

# Dissertation

submitted to the  
Combined Faculties for the Mathematics, Engineering and Natural  
Sciences  
of the Heidelberg University, Germany,  
for the degree of  
Doctor of Natural Sciences

Put forward by

**Michael Remmel, M.Sc.**

born in Karlsruhe, Germany

Date of the oral examination: 9. Dezember 2022



**Characterization of Fluorescent  
Molecular Switches  
for MINFLUX Nanoscopy**

Referees: Prof. Dr. Dr. h. c. mult. Stefan W. Hell  
Prof. Dr. Joachim Spatz



## Zusammenfassung

Nach der Überwindung der Beugungsgrenze mit supraauflösenden Techniken wie STED und PALM/STORM kombiniert die MINFLUX Nanoskopie die Vorzüge dieser Techniken und verschiebt die optische Auflösung hin zur Markergröße. Daher konzentriert sich die Fluoreszenzmikroskopie mehr denn je auf einzelne Fluorophore, wobei verschiedene fluoreszierende und nicht-fluoreszierende Zustände ausgenutzt werden. Das Photoschaltverhalten zwischen diesen Zuständen ist jedoch im Hinblick auf MINFLUX noch nicht analysiert worden. Diese fluorophorspezifischen Eigenschaften haben einen großen Einfluss auf die Bildqualität, insbesondere auf die Lokalisierungseffizienz in Bezug auf Erfolg und Geschwindigkeit. In dieser Arbeit wurden zwei Farbstoffklassen mit unterschiedlichen anregungsentkoppelten Schaltmechanismen (reversibel und irreversibel) auf ihr Potenzial für die MINFLUX Bildgebung untersucht. Zu diesem Zweck wurde ein vielseitiger Mikroskopieaufbau entworfen, der Charakterisierungen auf der Einzelmolekülebene im konfokalen und Weitfeld-Beleuchtungsmodus sowie PALM/STORM Mikroskopie ermöglicht, um die besten Farbstoffkandidaten für die MINFLUX Bildgebung zu identifizieren. Spontan blinkende Fluorophore (reversibles Schalten) erlaubten eine bis zu 30-fache Steigerung der Lokalisierungsgeschwindigkeit im Vergleich zu bereits publizierten blinkenden Farbstoffen. Mit photoaktivierbaren Farbstoffen (irreversibles Schalten) wurde der Lokalisierungserfolg der MINFLUX Nanoskopie zum ersten Mal quantitativ mit dem der PALM Mikroskopie verglichen. Darüber hinaus wurden Abstände innerhalb eines Markers bestimmt, was eine neue Perspektive auf die Markierungsstrategien für die Bildgebung biologischer Strukturen wirft.



## Abstract

After circumventing the diffraction limit with super-resolution techniques like STED and PALM/STORM, MINFLUX nanoscopy combines the advantages of these techniques, pushing the optical resolution down to the label size. Thus, more than ever, fluorescence microscopy focuses on single fluorophores, exploiting different fluorescent and non-fluorescent states. However, the behavior of the photoswitching between these states has not been investigated with respect to the MINFLUX performance. These fluorophore-specific properties heavily influence the image quality, particularly the localization efficiency in terms of success and speed. In this thesis, two dye classes with different excitation-decoupled switching mechanisms (reversible and irreversible) were evaluated for their potential for MINFLUX imaging. To this end, a versatile microscope setup was designed, enabling characterizations on single molecule level in confocal and wide-field illumination mode as well as PALM/STORM microscopy to identify the best dye candidates for MINFLUX imaging. Spontaneously blinking fluorophores (reversible switching) allowed for an up to 30-fold increase of localization speed as compared to previously reported blinking dyes. With photoactivatable dyes (irreversible switching), the localization success of MINFLUX nanoscopy was quantitatively benchmarked for the first time against PALM microscopy. Moreover, intra-marker distances were visualized, provoking a new perspective on labeling strategies for biostructural imaging.



# Contents

<b>List of Abbreviations</b>	<b>iii</b>
<b>Preface</b>	<b>1</b>
<b>1 Fluorescence Nanoscopy</b>	<b>4</b>
1.1 Fluorescence . . . . .	4
1.1.1 Molecular Fluorescence . . . . .	4
1.1.2 Reversible On/Off-Switching . . . . .	9
1.1.3 Irreversible On-Switching . . . . .	11
1.2 Fluorescence Nanoscopy . . . . .	12
1.2.1 Spatial Resolution . . . . .	13
1.2.2 General Concept of Super-Resolution Microscopy . . . . .	13
1.2.3 The MINFLUX Concept . . . . .	15
1.3 Why do Fluorophores Matter? . . . . .	17
<b>2 Material and Methods</b>	<b>21</b>
2.1 Instrumentation . . . . .	22
2.1.1 Confocal Setup . . . . .	22
2.1.2 Wide-field Setup . . . . .	24
2.1.3 Data Acquisition . . . . .	25
2.2 Data Analysis . . . . .	26
2.2.1 Single Molecule Experiments . . . . .	26
2.2.2 Image Processing . . . . .	29
2.3 Sample Preparation . . . . .	32
2.3.1 <i>In Vitro</i> Experiments . . . . .	32
2.3.2 <i>In Cellulo</i> Experiments . . . . .	33
<b>3 Spontaneously reversible On-Switching Dyes</b>	<b>35</b>
3.1 Introduction and Aim . . . . .	36
3.2 Results . . . . .	38
3.2.1 Photophysical Characterization . . . . .	38
3.2.2 STORM Imaging . . . . .	43
3.2.3 MINFLUX Imaging of nuclear pore complexes . . . . .	46
3.3 Discussion . . . . .	49

<b>4</b>	<b>Irreversible On-Switching Dyes</b>	<b>52</b>
4.1	Introduction and Aim . . . . .	53
4.2	Results . . . . .	55
4.2.1	Photophysical Characterization . . . . .	55
4.2.2	PALM Imaging . . . . .	58
4.2.3	MINFLUX Imaging . . . . .	62
4.2.4	Apparent density of labeling in MINFLUX and PALM Imaging . .	65
4.3	Discussion . . . . .	69
<b>5</b>	<b>Applications of irreversible switches</b>	<b>70</b>
5.1	Resolving the Fluorescent Label . . . . .	70
5.2	Dual Color MINFLUX Imaging . . . . .	73
5.3	Discussion . . . . .	77
<b>6</b>	<b>Conclusion and Outlook</b>	<b>78</b>
<b>7</b>	<b>Supplementary Information</b>	<b>82</b>
7.1	Commercial MINFLUX microscopic setup . . . . .	82
7.2	Custom-built MINFLUX microscopic setup . . . . .	83
7.3	Initial PALM data analysis for evaluating the apparent density of labeling . . . . .	84
7.4	Labeling Protocols . . . . .	85
7.5	Reagents and Proteins . . . . .	88
	<b>List of Tables</b>	<b>90</b>
	<b>List of Figures</b>	<b>92</b>
	<b>Publications</b>	<b>93</b>
	<b>Bibliography</b>	<b>100</b>
	<b>Acknowledgments</b>	<b>101</b>

# List of Abbreviations

<b>1D</b>	one dimension
<b>2D</b>	two dimension
<b>AB</b>	antibody
<b>ADOL</b>	apparent density of labeling
<b>AF647</b>	AlexaFluor 647
<b>AOTF</b>	acousto optical tunable filter
<b>APD</b>	avalanche photodiode
<b>BSA</b>	bovine serum albumin
<b>BS</b>	buffer solution
<b>bt</b>	biotin
<b>CFR</b>	center frequency ratio
<b>CRISPR</b>	clustered regularly interspaced short palindromic repeats
<b>CW</b>	continuous wave
<b>DBSCAN</b>	density-based spatial clustering of application with noise
<b>DCR</b>	dual color ratio
<b>DM</b>	dichroic mirror
<b>DMEM</b>	Dulbecco's modified Eagle medium
<b>DR</b>	detection ratio
<b>DOL</b>	density of labeling
<b>eCCDF</b>	experimental complementary cumulative distribution
<b>EMBL</b>	European laboratory for molecular biology
<b>EMCCD</b>	electron mutliplying charge-coupled device
<b>FBS</b>	fetal bovine serum
<b>FPGA</b>	field programable gate array
<b>FRET</b>	förster resonance energy transfer
<b>GFP</b>	green fluorescent protein
<b>FWHM</b>	full width at half maximum
<b>GSD</b>	ground state depletion
<b>HILO</b>	highly inclined and laminated optical sheet
<b>HMSiR</b>	hydroxymethyl silicon rhodamine
<b>HOMO</b>	highest occupied molecular orbital
<b>IC</b>	internal conversion
<b>ISC</b>	intersystem crossing
<b>LUMO</b>	lowest unoccupied molecular orbital
<b>MPH</b>	motorized pinhole
<b>NB</b>	nanobody
<b>NPC</b>	nuclear pore complex
<b>NTA</b>	nitrilotriacetic acid group

<b>Nup</b>	nucleoporin
<b>PAX</b>	photoactivatable xanthenes
<b>PALM</b>	Photoactivated Localization Microscopy
<b>PAINT</b>	points accumulation for imaging in nanoscale topography
<b>PBS</b>	phosphate buffer system
<b>PFA</b>	paraformaldehyde
<b>PLL-PEG</b>	poly(L-lysine)-poly(ethylene glycol)
<b>PMT</b>	photomultiplier tube
<b>RESOLFT</b>	Reversible Saturable Optical Fluorescence Transitions
<b>ROI</b>	region of interest
<b>ROXS</b>	reductive oxidative system
<b>S</b>	singlet state
<b>SBR</b>	signal-to-background ratio
<b>SMLM</b>	single molecule localization method
<b>STED</b>	Stimulated Emission Depletion
<b>STORM</b>	Stochastic Optical Reconstruction Microscopy
<b>STV</b>	streptavidin
<b>T</b>	triplet state
<b>TIRF</b>	total internal reflection fluorescence microscopy
<b>UV</b>	ultraviolet

# Preface

In experimental sciences, the core of knowledge lies in observation. For most developed living beings observation occurs primarily through visual exploration of their conspecifics and the environment, which is enabled by the electromagnetic interaction between photons and matter. However, human optical systems are very versatile, but inherently limited in terms of resolution. To address this shortcoming, technical optical systems have been developed that exploit the refraction of light, opening the scientific field of light microscopy. As visible light minimally affects most known biochemical structures, it is particularly desirable to use in experiments of biological relevance. However, conventional light microscopy suffers from poor contrast in biological samples, making fluorescence microscopy the technique of choice for life science research. Labeling the sample with a fluorophore complicates sample preparation but also ensures specificity with respect to the structure of interest.

Fluorescence microscopy greatly improves resolution compared to the human eye, but does not resolve beyond spatial distances of  $d \approx 200 \text{ nm}$ , which is about half the wavelength of visible light. This barrier is known as the Abbe limit [1] and was accepted to be the final frontier of light microscopy until the late twentieth century. The introduction of Stimulated Emission Depletion (STED, [2]) changed this paradigm by fundamentally undercutting the Abbe limit [3]. This coordinate-targeted approach to diffraction-unlimited fluorescence imaging utilizes a depletion beam as a reference coordinate to reduce the spatial dimension, from which spontaneous fluorescence can originate. As seeing is believing, a rush into the scientific field of super-resolution microscopy was set off ever since the experimental evidence, with more and more techniques circumventing the diffraction barrier being developed. Two other notable techniques, utilize a coordinate-stochastic approach: Stochastic Optical Reconstruction Microscopy (STORM, [4]) and Photoactivated Localization Microscopy (PALM [5, 6]), introduced about ten years after STED, impress by their relatively simple experimental setup. Admittedly, coordinate-targeted and coordinate-stochastic techniques differ strongly in their technical implementation. What both approaches have in common, however, is putting the individual fluorophores in the spotlight. By inducing different electronic states, the emission of the fluorophores is controlled in time

---

so that only the information of a subset of markers is detected at once. Theoretically, the resolution of approaches is unlimited, but the burden of the measurement lies on the fluorophores. Practically, the resolution of the methods depends on the number of emission cycles. Since fluorophores have a statistical probability of photo-bleaching, limiting the number of these cycles and thus the resolution that can be practically achieved to  $\sigma \approx 20$  nm.

Recently, a conceptually new realization called MINFLUX [7] has been developed, combining the strategies of the established approaches to diffraction unlimited resolution. Combining the injection of a reference coordinate (coordinate-oriented) with working at the single fluorophore level (coordinate-stochastic), provides a photon-gentle way to obtain precise localization information from individual emitters. Through multiple exposures with the intensity minimum of a structured excitation beam (e.g. donut pattern) in the vicinity of the emitter, its position can be calculated. In an iterative process, the excitation power is increased enabling a refinement of the calculated fluorophore position over several steps. By placing the excitation minimum on the calculated position after each step, most of the load off the fluorophore is taken away. This approach proved to break the diffraction limit ultimately by localizing with a precision down to  $\sigma \leq 1$  nm [8].

Fueled by this new nanoscopy method, dye research is taking a new direction. The paradigm that the maximum number of photons is the most important parameter to obtain the highest possible localization precision became secondary, as several hundred photons are sufficient for a precision in the single-digit nanometer range with MINFLUX [7]. This allows for the optimization of other dye parameters more important to MINFLUX nanoscopy. Now the single fluorophore discrimination criterium and therefore the control of the fluorescent on- and off-states of the molecule is of utmost importance, as it impacts the localization efficiency in terms of speed and success. Owing to the novelty of the technique, first localization and imaging experiments have been performed with the well-known AlexaFluor647 dye [7–9], a cyanine dye optimized for STORM microscopy. The dye is known to enter photo-induced long-lived dark states in distinct oxygen-depleted buffer systems containing thiols, and to emit a high number of photons before it photo-bleaches. Indeed, performing MINFLUX imaging is possible with this dye, but the unnecessary high number of photons is pricey and paid by prolonged localization times. Moreover, the dependence of the switching process on the excitation laser, which either switches the dye into the off-state or photo-bleaches it, additionally affects the localization efficiency.

In light of this setting, the aim of this thesis is the characterization of novel dyes and their switching mechanisms with respect to their suitability for MINFLUX nanoscopy. To this end, a versatile optical setup was designed and built, enabling dye characterization

---

in a single molecule environment in both confocal and wide-field illumination mode. First, statistical analysis was performed for the parameters most relevant to MINFLUX nanoscopy. In the second step, different biological structures were stained with various dye bioconjugates in fixed and living cells, to investigate their versatility as fluorescent markers and imaged with established techniques (confocal, PALM/STORM) using the custom-built setup. Finally, their usability in MINFLUX was proven by labeling nuclear pore complexes with different dye conjugates and imaging them with different MINFLUX systems. Utilized as standard sample system in super-resolution microscopy nuclear pore complexes enabled a wide range of measurements of different emitters and labeling strategies. Thus, among others, it was possible to increase the localization speed up to 30 times compared to previously published MINFLUX measurements, and to resolve one of the smallest fluorescent labels up today. The results obtained in this thesis toss a new view onto the implementation of MINFLUX measurement routines as well as emphasize the importance of labeling in nanoscopy.

The thesis comprises five chapters. While the first chapter covers an overview of the theoretical background of fluorescence and super-resolution microscopy (with emphasis on MINFLUX nanoscopy), also different photoswitching mechanisms with respect to MINFLUX are discussed. In chapter 2 the methodology of the conducted experiments is described, specifically sample preparation, photophysical characterization, imaging and evaluation of the data. Finally, in chapter 3 and 4, the investigation of two different dye families is presented. Fluorophores described in chapter 3 perform reversible on/off-switching stochastically within the ground state. In contrast, dyes presented in chapter 4 are irreversible fluorescent on-switches, being photoactivated via a transition in the excited state. For both photoswitching mechanisms, a comprehensive study is presented, including single molecule characterization, labeling with different bioconjugates, PALM, STORM and MINFLUX imaging of the respective biological structures and subsequent nanoscopy data evaluation. Exploiting the irreversible switching behavior of photoactivatable dyes presented in chapter 4 enabled different applications relevant for future considerations in MINFLUX nanoscopy (see chapter 5).

The results presented in this thesis were also subject of paper published and submitted as well as in preparation (see Publications).

# Chapter 1

## Fluorescence Nanoscopy

This chapter comprises a theoretical overview of the presented thesis. First the theoretical aspects of fluorescence are discussed in section 1.1. With regard to its application in fluorescent microscopy a more detailed view is put on the different fluorescent switching processes.

In section 1.2 MINFLUX nanoscopy is put into the context of established super-resolution techniques.

The chapter concludes with theoretical considerations of the on- and off-switching mechanisms utilized in MINFLUX nanoscopy in section 1.3.

### 1.1 Fluorescence

Fluorescence is the emission of light by a molecule after the absorption of light by the very same. The process is induced by transitions between different electronic singlet states within the molecule.

#### 1.1.1 Molecular Fluorescence

Covalent bonds are the predominant binding type in organic molecules. A covalent bond is created by two atoms sharing some of their valence electrons. The probability of finding the electrons around the atom's nucleus is represented by atomic orbitals. When an atomic orbital partly overlaps with an atomic orbital from the neighboring atom, a

molecule orbital is formed (for organic fluorophores, mainly s- and p- orbitals contribute). The spatial overlap defines the shape of the molecule as well as the energy levels of its electronic states. Figure 1.1A displays formaldehyde and the energy levels of the molecular orbitals, which are formed by the electrons occupying the carbon-oxygen bond and the non-binding electrons. For molecules containing heteroatoms, the promotion of an electron from the HOMO (highest occupied molecular orbital) to the LUMO (lowest unoccupied molecular orbital) represents the main route of transitions into an energetically higher state of the molecule. These transitions can be understood as the excitation of an electron from a lower to a higher energy level and are shown in figure 1.1B. The electronic ground state of most stable organic molecules possesses a multiplicity equal one. Consequently, all transitions that leave the electron spin unaffected create singlet excited states. A spin flip during the transition results in a triplet state. According to the spin selection rule, the transition between singlet state  $S_x$  and triplet states  $T_x$  are forbidden. However, the triplet states can be populated from excited singlet states by intersystem crossing, mainly via spin-orbit interactions.

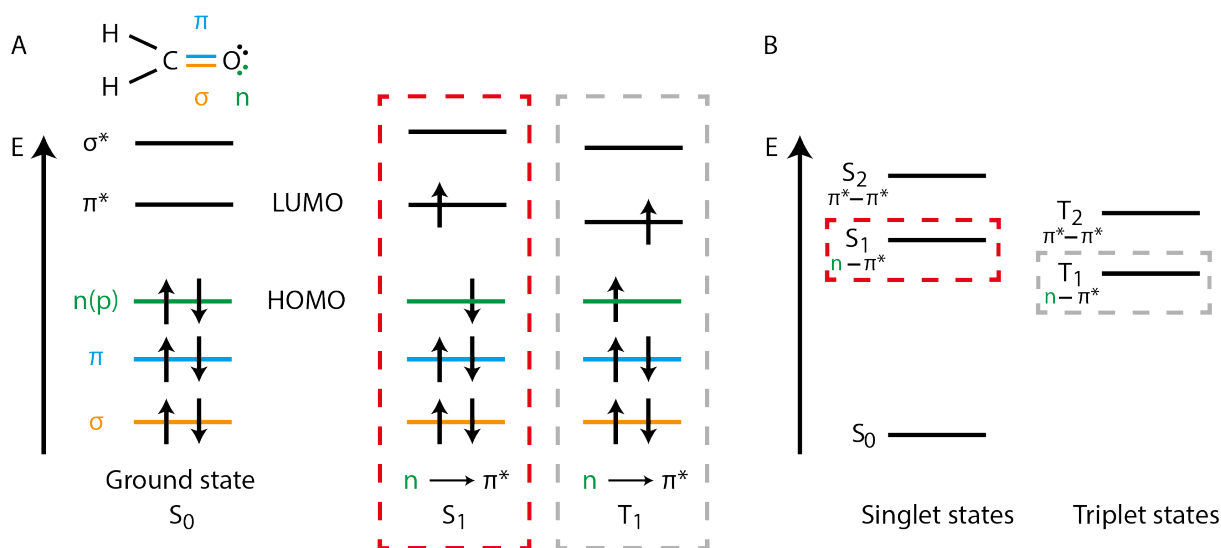


Figure 1.1: **Molecular orbitals and electronic energy states of formaldehyde.** A) The molecular orbitals of the ground state  $S_0$  and the lowest excited singlet (spin conserving,  $S_1$ ) and triplet state (spin changing,  $T_1$ ). In both excited cases, one electron of the HOMO is excited into the LUMO. B) The different electronic states of formaldehyde caused by excited electrons. Higher states than  $S_1$  and  $T_1$  can be achieved by excitation of an electron from a lower orbital than the HOMO (Figure adapted from [10]).

Molecular states and transitions can be visualized in a Perrin-Jablonski diagram as shown in figure 1.2. Starting at the electronic ground state  $S_0$ , the absorption of a photon (light) results in an excited molecule ( $S_{x>0}$ ). From an excited singlet state, a molecule can deexcite via different processes: internal conversion ( $S_{x+1}$  to  $S_x$ ), fluorescence ( $S_1$  to  $S_0$ ) or intersystem crossing ( $S_{x>0}$  into  $T_x$ ). While the first and the last one are

non-radiative processes, in which energy is transferred via vibrational relaxation (thin black lines) to the surrounding, the second one is a radiative process. From the triplet state, the molecule can return to the corresponding singlet state by reverse intersystem crossing ( $T_x$  to  $S_x$ ) or deexcite by phosphorescence ( $T_x$  to  $S_0$ ). Furthermore, while occupying an electronic state, a molecule can adopt different vibrational states. This affects photon energies in the absorption and emission process, yielding broad spectra for both (see figure 1.2 bottom), with their shapes being determined by the probability of the individual transitions (Franck-Condon-Principle). Moreover, the vibrational relaxation of the molecule itself as well as solvent reorganization during the lifetime of the first excited singlet state  $S_1$  (Kasha's Rule) leads to a shift of the emission spectrum to lower energies compared to the absorption spectrum (Stokes Shift).

Transition processes, originating from the same excited state (e.g.  $S_1$ ) are competing, each with a probability defined by its individual decay rate  $k_x$ . Thus, the sum of these processes determines the lifetime of the respective excited state and the lifetime of  $S_1$ , i.e. the fluorescence lifetime, reads

$$\tau_{S1} = \frac{1}{k_{em} + k_{ic} + k_{isc}} \quad . \quad (1.1)$$

Moreover, the probability for the deexcitation via fluorescence is defined as the quantum yield

$$\Phi_{fl} = \frac{k_{em}}{k_{em} + k_{ic} + k_{isc}} \quad . \quad (1.2)$$

For highly fluorescent molecules, the internal conversion rate and intersystem crossing rate are low compared to the fluorescence emission rate, which results in a high probability of the molecule deexciting via fluorescence. Also, compared to the singlet lifetime (typical nanoseconds), the triplet lifetime (typical microseconds) is orders of magnitude higher, as the spin multiplicity differs from the one of the ground state  $S_0$ .

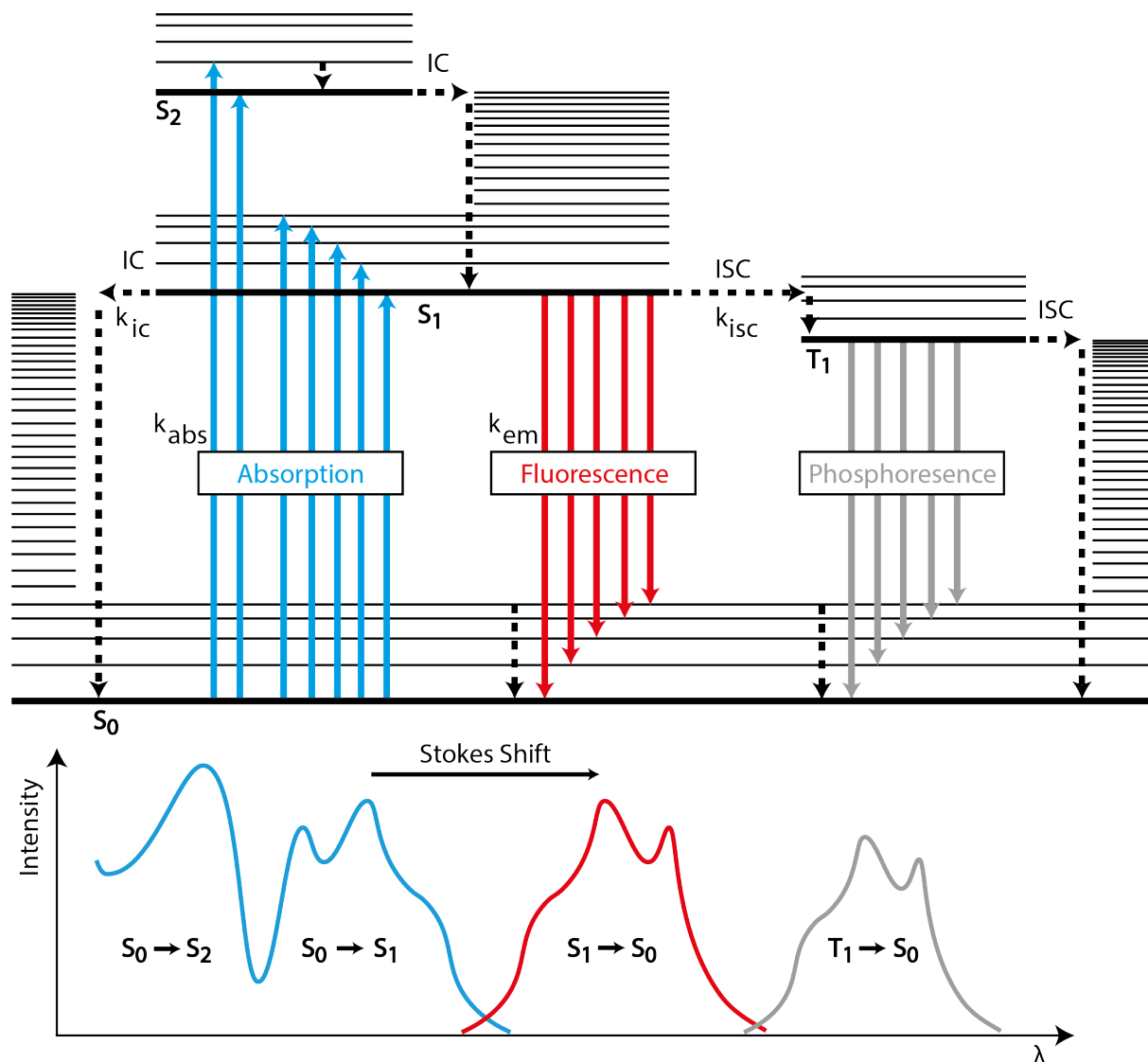


Figure 1.2: **Perrin-Jablonski diagram of the energy states and transitions of a molecule.** Absorption of a photon excites the molecules into a higher singlet state ( $S_1$  or  $S_2$ ). After rapid vibrational relaxation, it can either deexcite via internal conversion (IC) or fluorescence into the ground state  $S_0$ , or reach the triplet state  $T_1$  via intersystem crossing (ISC). From triplet state, it can deexcite via phosphorescence or intersystem crossing. Moreover, the vibrational states of the molecule lead to a spread in energy for the individual transitions resulting in broadened spectra for absorption and emission (bottom). The probability of the individual transitions defines the shape of the spectra (Franck-Condon-Principle), and together vibrational relaxation and solvent reorganization during the fluorescence lifetime yield an energy difference between the absorption and emission spectra (Stokes Shift). Electronic states are shown as thick black lines, vibrational states as thin black lines (Figure adapted from [11]).

In real-life, the process of absorption and fluorescence emission cannot be repeated indefinitely. Instead, when illuminating an ensemble of dyes, a decrease of fluorescence light can be observed over time. This is due to the fact that the fluorophores have a probability of photo-bleaching, i.e. irreversibly changing their chemical structure in a way such that they cannot absorb and emit photons anymore. These degradation processes have been known and investigated for a long time [12], but are still not fully understood today. However, by now it is known that one type of photodegradation processes has its origin in the triplet state. In  $T_x$ , the molecule is highly reactive and can be oxidized either by molecular oxygen (triplet in the ground state) or by reactive oxygen species produced by triplet-triplet annihilation between another triplet state molecule and molecular oxygen or it can be photon-ionized by another photon [13]. Figure 1.3 shows a simplified Jablonski diagram including photo-bleaching.

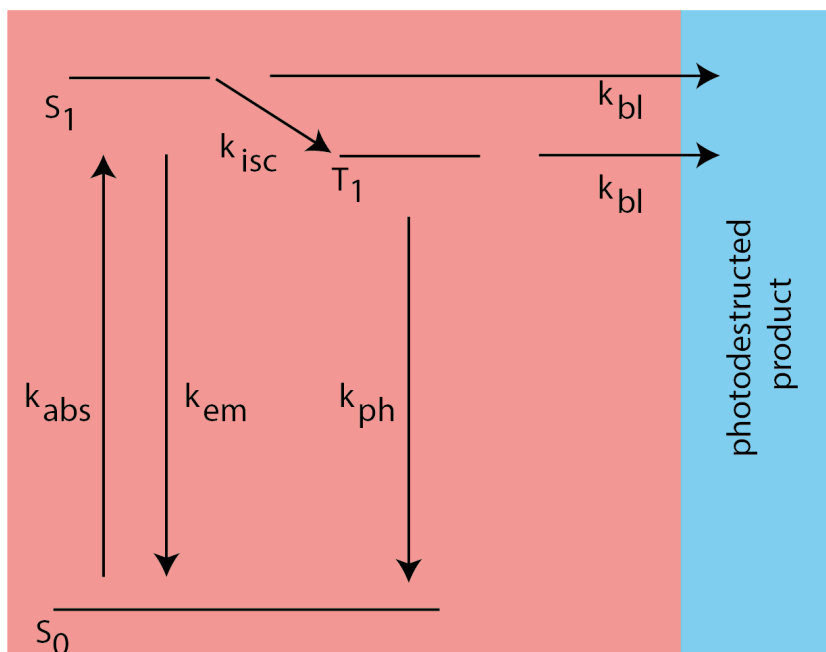


Figure 1.3: **Simplified Jablonski diagram of the triplet state transitions.** Via intersystem crossing (e.g. by spin-orbit interactions) a molecule can switch from  $S_1$  into the triplet state  $T_1$  with the rate  $k_{isc}$ . The molecule becomes highly reactive and can be oxidized by molecular oxygen or reactive oxygen species (e.g. singlet oxygen generated through triplet-triplet annihilation between molecular oxygen and another triplet state molecule) or deexcites via phosphorescence with the rate  $k_{ph}$ .

Nevertheless, significant photo-bleaching of molecules with a quantum yield close to one (i.e. minimized probability of intersystem crossing to the triplet state), indicates that other photo-bleaching mechanisms independent of triplet states are the cause for loss in fluorescence [14]. Metastable states [14] and photo-bleaching through the  $S_1$  state [15, 16] are suggested. The vast amount of published studies not only emphasize the complexity of photo-bleaching [17], but also how much it is still up for debate today. However, these

processes can all be reversed by reductive and/or oxidative additives. Donating to or accepting electrons from the fluorophore, these reductive/oxidative systems (ROXS) are reported to enhance the lifetime significantly [18, 19].

While photo-bleaching is a light-induced, irreversible structural change leading to a non-fluorescent product, there are also photochemical processes resulting in the opposite phenomenon, i.e. photo-induced switching from a non-fluorescent state into a fluorescent state. This irreversible on-switching process, termed photoactivation or uncaging, as well as reversible on- and off-switching processes (photo-induced or thermal) are exploited in all fluorescence nanoscopy techniques comprising coordinate-targeted techniques following the RESOLFT approach [20], single molecule localization methods like PALM and STORM [5, 6], and MINFLUX [7] (see section 1.2.2). Especially for the latter technique, the photoswitching mechanisms are from high relevance and therefore one of the main subjects of this thesis.

### 1.1.2 Reversible On/Off-Switching

The term 'switching' refers to the transition between different states with distinct photo-physical properties a fluorescent molecule can possess. More precisely, it ascribes transitions between states, in which the fluorophore emits light (on-state) and in which its emission is heavily suppressed (off-state). This transitions can be reversible or irreversible (see section 1.1.3). The mechanisms yielding a reversible switching behavior can be either photochemically or thermally induced. The main difference lies in the state the molecules possesses while switching back and forth. In a photochemically induced mechanism, the molecule switches from the excited state  $S_1$  into long-lived dark states, while the thermal mechanisms lead to switching between two different ground states  $S_0$  [21].

Reversible photochemical switching is the most utilized switching concept in STORM microscopy. However, a general switching mechanism cannot be pointed out, as multiple ones are proposed, depending on the type of dye and its chemical structure. As photochemical switching is induced while the molecule is in  $S_{x>0}$ , the power of the excitation laser plays a significant role for the transition into long-lived dark states, determining the population density of these off-states. The best-studied photochemical switching mechanisms are all based on intersystem crossing into the triplet state  $T_1$  with a typical lifetime of several tens to several hundreds of microseconds. The comparatively long lifetime to  $S_1$  (typical showing nanosecond lifetimes) results in a higher probability for inducing a transfer into longer-lived dark states. The photochemical processes behind this transfer are similar to the irreversible photo-bleaching (usually undesired transfer

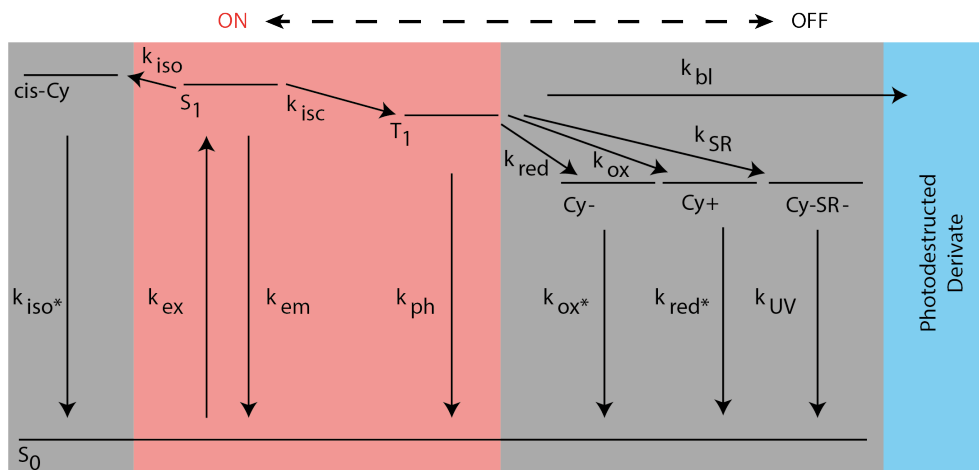


Figure 1.4: **Main photochemical/photophysical processes of Cy5.** The scheme displays the main photochemical/photophysical processes of Cy5 comprising its in on-state (red), off-state (grey) and the irreversibly photo-bleached state (blue). All switching processes are initiated from the excited singlet state ( $S_1$ ) and compete, with their rates determining their individual probabilities and the lifetimes of the individual states. The thiolated state  $\text{Cy-SR}^-$  represents the long-lived dark state exploited in STORM and MINIFLUX microscopy.

into a permanent dark state), namely photoionization, photooxidation or photoreduction. Also, cis-trans isomerization can induce a off-state by disturbing the planarity of the chromophore. The lifetimes of all these dark states depend on the chemical structure of the molecule. For fluorescent proteins for example, protonation and cis-trans isomerization can result in long off-states [22]. The cyanine dye Cy5, a well-known dye in the field of STORM microscopy, is reported to show different dark states based on all the mechanisms mentioned above with an average lifetime of several hundred microseconds, similar to the triplet state lifetime [23]. These dark states are too short-lived to keep a significant amount of dyes in the off-state to guarantee single molecule conditions (i.e. only one dye in on-state per diffraction limited area). Another photochemical switching mechanism, also applicable for Cy5, is induced by thiols, which covalently bind in the region of the chromophore and break the conjugated system, forming a non-fluorescent molecule. This conjugate is reported to be stable up to several hours [24]. The fluorescent molecule can be recovered with UV illumination. A scheme illustrating the photoswitching mechanism of Cy5 is depicted in figure 1.4. Also several rhodamines [25] as well as the enhanced yellow fluorescent protein eYFP [26] are reported to undergo thiol-based photoswitching. Furthermore, uncoupling the photo-induced switching from the excitation source was realized with fluorescent proteins [27].

Structural fluorogenicity in contrast, does not depend on light for switching between a fluorescent and a dark state, but instead relies on thermal switching in ground state  $S_0$  (see figure 1.5). This is accomplished by structural changes between a non-fluorescent and

a fluorescent form of the molecule (e.g. protonated form, isomers). Mechanisms allowing for ground state switching are manifold, such as reversible nucleophilic attack by a thiol [28], conformational locking [29] or internal spirocyclization [21, 30]. The latter is based on the proton equilibrium between the fluorophore and its aqueous environment. For rhodamines and silicon-rhodamines, which are popular due to their high quantum yields, spirocyclization causes a reversible disturbance of the conjugated system of the rhodamine core. As the application of spontaneously blinking silicon rhodamines for MINFLUX imaging is part of this thesis, a detailed comparison of their switching behavior with the established thiol-based switching can be found in chapter 3.

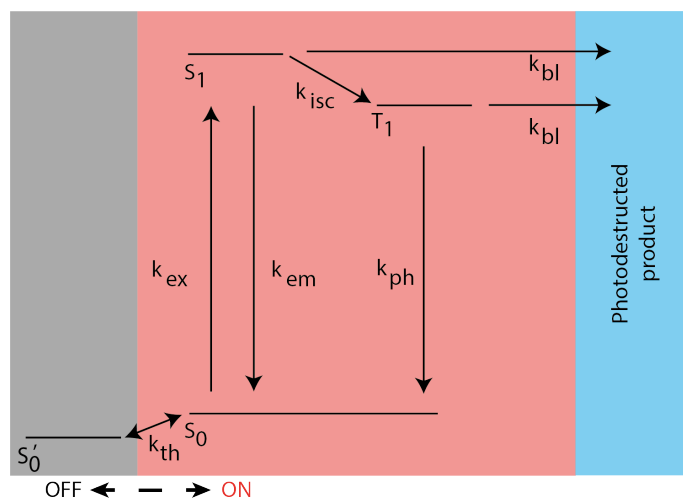


Figure 1.5: **Spontaneous reversible on/off-switching of fluorophores.** The Jablonski diagram depicts the basic principle of spontaneously (thermally) switching fluorophores. The molecule stochastically switches between two ground states ( $S'_0$  and  $S_0$ ), of which  $S'_0$  is not absorbing or emitting light.

### 1.1.3 Irreversible On-Switching

In contrast to reversible on/off-switching, irreversible on-switching results in only one burst of photons by which the organic fluorophore or fluorescent protein can be detected before photo-bleaching. Consequently, not only the transition into the on-state is irreversible, also the off-state is permanent, as it is represented by photo-bleaching.

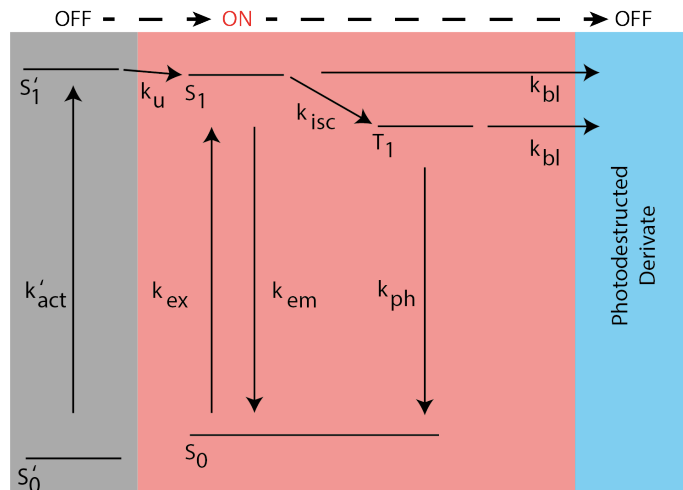


Figure 1.6: **Irreversible on-switching of fluorophores.** The Jablonski diagram depicts basics of photo-induced uncaging. An activation source (usually UV or 2-photon absorption) excites the molecule from a ground state  $S'_0$  into a non-fluorescent excited state  $S'_1$ . From there, it uncages (photoactivates) into  $S_1$  and can fluoresce. The molecule is permanently turned off by photo-bleaching.

The irreversible switching behavior can be installed in organic fluorophores by different means of photochemistry. The currently explored mechanisms comprise photo-cleavage of quenching groups (uncaging) [31–33], cage-free uncaging [34] and photo-conversion into a molecule with different spectral properties [35, 36]. Figure 1.6 illustrates the uncaging strategy as an example. By absorption of activation light the molecule gets excited from a ground state  $S'_0$  to an excited non-fluorescent state  $S'_1$ . The transition from  $S'_1$  to  $S_1$  yields a fluorescent molecule.

## 1.2 Fluorescence Nanoscopy

Fluorescence microscopy is a sub domain of light microscopy. The laws of optics are exploited and light refraction on lenses is used to enlarge the view of structures. Typical structures are of biological relevance and can be imaged without harm as visible light is used. While light microscopy often suffers from poor contrast in such samples, fluorescence microscopy circumvents this issue by dyeing the structures of interest, collecting the fluorescence light emitted by the molecule. Certainly, labeling a sample complicates its preparation, but also ensures specificity with respect to the structure of interest. More important to this thesis than the initial motivation of contrast enhancement, fluorescence microscopy sets the foundation for techniques that fundamentally beat the Abbe diffraction limit.

### 1.2.1 Spatial Resolution

Investigating the light propagation through optical gratings, Ernst Abbe discovered a maximum number of lines per region above which the grating structure could not be displayed anymore in the image. This was due to the fact that the maximum angle between the zero and first order diffraction maximum, carrying the grating information in the Fourier space, is  $180^\circ$  [1]. He deduced a formula describing the minimal distance  $d$  between two identical objects at which both can be recognized as different

$$d = \frac{\lambda}{2n \sin \alpha} = \frac{\lambda}{2\text{NA}} \quad , \quad (1.3)$$

with the numerical aperture (NA) being the product of the immersion medium refractive index and the half-opening angle of the microscope objective lens. For modern objective lenses with a  $\text{NA} \approx 1.4$ , the diffraction limit amounts to roughly half of the employed wavelength  $\lambda$ , limiting the resolution to  $d \approx 200$  nm for green light.

### 1.2.2 General Concept of Super-Resolution Microscopy

The Abbe diffraction limit was found to be the resolution limit of optical microscopy more than a century ago and still holds true today. However, in the late 20th and the early 21st century, techniques were developed to circumvent the diffraction limit [2]. All these approaches are specialized variants of fluorescence microscopy and make use of distinguishable fluorophore states to specifically address sub-ensembles of fluorophores, with the aim to detect only one fluorophore per diffraction-limited spot at best. Two general procedures can be distinguished, namely coordinate-targeted approaches and coordinate-stochastic approaches [37].

**Coordinate-Targeted Approaches** utilize a focused structured depletion beam with one (or more) intensity zero(s) creating one (or more) sub-diffraction reference coordinate(s) in the sample. By overlapping a gaussian-shaped excitation beam with the commonly used donut-shaped depletion beam during scanning, only a sub-ensemble of excited molecules close to the reference coordinate (central intensity zero) is allowed to spontaneously emit photons, enabling the continuous readout of information from a sub-diffraction-limited area. The suppression of spontaneous fluorescence in the periphery of the reference coordinate can be achieved either by Stimulated Emission Depletion (STED [2]) or by populating long-lived dark states (Ground State Depletion, GSD [38]), both generalized as Reversible Saturable Optically Linear Fluorescence Transitions (RESOLFT [20]) microscopy. The spatial resolution is determined by the sub-population size staying in an emissive

state, which in turn is influenced by the intensity distribution of the depletion beam around its zero intensity. Therefore, the obtained resolution mainly depends on the intensity of the depletion beam and is approximated by

$$\sigma = \frac{\lambda}{2n \sin \alpha \sqrt{1 + I/I_s}} = \frac{d}{\sqrt{1 + I/I_s}} \quad , \quad (1.4)$$

with  $I$  being the intensity of the depletion beam and  $I_s$  the intensity, at which the probability to evoke the depletion process (e.g. stimulated emission) equals 0.5 [37, 39]. In contrast to equation 1.4, the resolution can be adapted by changing the illumination intensity of the depletion laser. As the laser power does not represent a limiting factor, the resolution can be pushed to the size of a single fluorescent molecule in theory. In reality however, the large number of excitation-and-depletion cycles bears the risk of photo-bleaching before the fluorophores were allowed to spontaneously emit, thus limiting the resolution to about 30 nm for organic dyes in biological samples [40].

**Coordinate-Stochastic Approaches** in contrast, comprise methods that calculate the centroid position of the diffraction-limited emission pattern of single emitters by focusing a 2D pixel detector onto the sample plane without any *a priori* knowledge about the emitter's position. As coordinate-targeted approaches, stochastic approaches make use of different molecule states to ensure that only one emitter is in the fluorescent on-state per diffraction-limited spot at a time. This can be achieved with the photoswitching mechanisms described in section 1.1. The most established techniques make use of either photoactivation with subsequent excitation, detection and photo-bleaching (Photoactivated Localization Microscopy, PALM [5, 6]), reversible conditional or stochastic transitions between emissive and non-emissive states (Stochastic Optical Reconstruction Microscopy, STORM [4]), or by transient binding of emissive fluorophores (Points Accumulation for Imaging in Nanoscale Topography, (DNA-)PAINT [41, 42]). As the precision of the centroid position calculation strongly relies on the number of detected photons, the resolution of these techniques can be described in the absence of background by

$$\sigma = \frac{d}{\sqrt{N}} \quad , \quad (1.5)$$

with  $N$  being the number of detected photons. The square root dependence of the equation results in a moderate increase of resolution (compared to the Abbe limit) for low photon numbers, but also heads into a progressive decrease of additional information with every detected photon. Moreover, as the coordinate-targeted approaches described above, photo-bleaching limits the number of detectable photons and therefore the localization precision typically to 10 – 20 nm. This experimental resolution limit can be pushed by

optimization of the experimental parameters, i.e. by applying ROXS to reduce photo-bleaching [18] and by identifying novel fluorescent molecules [43, 44], but cannot be ultimately overcome.

With the development of MINFLUX nanoscopy [7], the problem of an experimentally limited localization precision as caused by the fading nature of fluorophores was overcome for the first time. The fundamentally new concept of using an excitation intensity minimum for localizing single fluorophores truly enables a localization precision of the size of the emitter itself.

### 1.2.3 The MINFLUX Concept

'Nanometer Resolution Imaging and Tracking of Fluorescent Molecules with Minimal Photon Fluxes' (MINFLUX nanoscopy, [7]) represents the combination of both established super-resolution approaches named above. It utilizes an excitation intensity distribution (coordinate-targeted), e.g. donut-shaped, for the excitation of single fluorophores with photoswitching ability between distinguishable states such that there is only one excitable molecule per diffraction-limited spot at a time (coordinate-stochastic). The molecule position is estimated via several exposures close to the excitation intensity zero (e.g. donut center), serving as reference coordinate. Using the information extracted from the detected photons, the excitation intensity zero is recentered with respect to the estimated molecule position in an iterative manner and thus the molecule is only exposed to minimal intensity. Due to this illumination strategy, the less photons are detected, the smaller the displacement between the intensity zero and the actual molecule position is.

In the original paper published by Balzarotti et al. [7] an excitation intensity distribution in the shape of a donut was employed and three exposures in a triangular pattern around the estimated molecule position  $x_0$  were performed, followed by a fourth exposure at the center of this pattern. For the ease of visualization, the one-dimensional case is illustrated in figure 1.7. The excitation pattern with its intensity minimum in the center illuminates the molecule of interest at three different positions  $+L/2$ ,  $-L/2$  and  $x_0$  to correlate the parameters 'excitation intensity' and 'excitation position' unambiguously. The photon flux emitted by the fluorophore depends on both the molecule's photophysical characteristics such as fluorescence quantum yield and absorption cross section, and on the local excitation intensity, which is determined by the distance of the molecule to the excitation intensity minimum. The fluorophore properties are constant as they are independent from the illumination intensity and the linear dependence between the number of detected photons and the local excitation intensity is valid as long as the

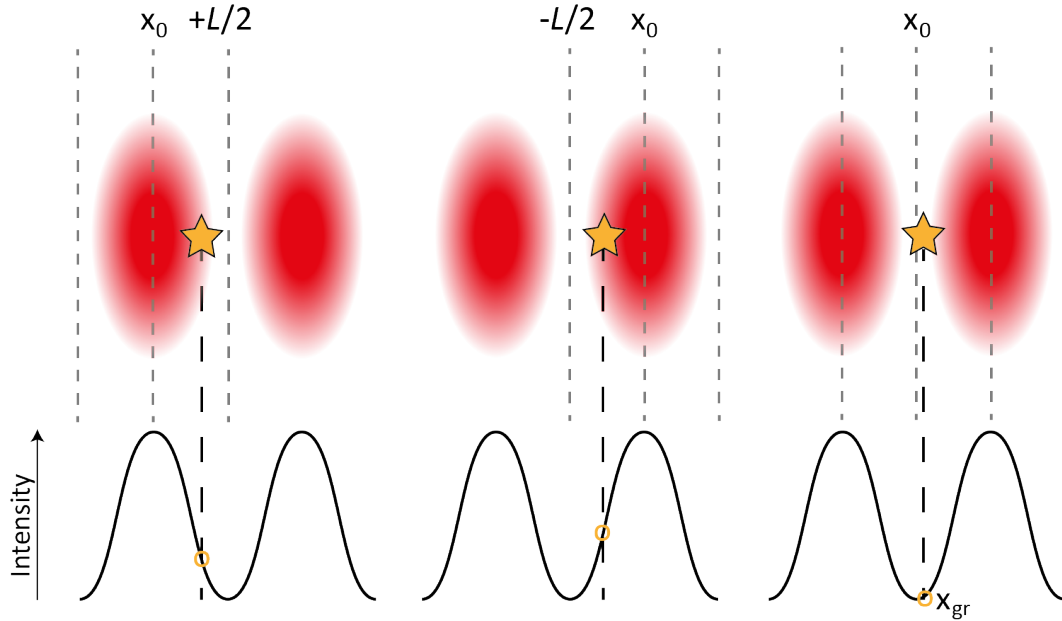


Figure 1.7: **MINFLUX excitation scheme visualized in 1D.** Illumination with the excitation intensity distribution at three positions ( $+L/2$ ,  $-L/2$ ,  $x_0$ ; grey dashed lines) exposes the emitter to different local excitation intensities (bottom), which in turn evokes the emission of different amounts of photons. A maximum likelihood estimation allows for the estimation of the most probable molecule position to which the excitation intensity minimum is readjusted.

molecule is not excited in a saturated regime. Thus, knowing the intensity pattern, a maximum likelihood approach can be used to estimate the molecule position with respect to the individual exposures and their corresponding photon counts. The center of the pattern can be readjusted with respect to the estimated molecule position.

By recentering the excitation intensity distribution, the displacement between the intensity zero and the molecule of interest decreases, reducing the effective intensity the molecule experiences. By increasing the excitation power, the intensity gradient experienced by the molecule increases, allowing for a smaller scanning range  $L$ . The concept of localizing single molecules via their excitation and not emission introduces the parameter  $L$  as a second quantity determining the localization precision

$$\sigma = c \cdot \frac{L}{\sqrt{N}} \quad , \quad (1.6)$$

with the constant  $c$ , determined by the exact shape of the diffraction-limited illumination pattern. The consequence of equation 1.6 becomes clear, when considering the fact that  $L$  is set by the experimenter. The impact of changing  $L$  can be seen in figure 1.8, showing the 1D localization precision  $\sigma$  of a quadratic excitation intensity distribution in dependence on the number of detected photons  $N$  for different sizes of  $L$ . Lowering  $L$  increases

the precision at a constant number of detected photons. The small scanning ranges are achieved via an iterative process, refining the position estimate with each step (figure 1.9). Compared to stochastic-coordinate approaches, this reduces the number of required photons by orders of magnitude (figure 1.8).

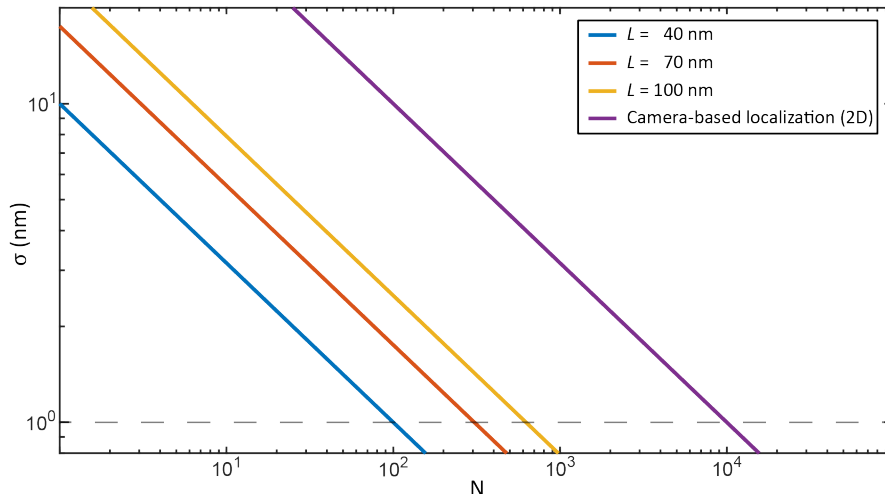


Figure 1.8: **MINFLUX localization precision in dependence on number of detected photons.** The 1D localization precision of MINFLUX with an excitation intensity minimum approximated by a parabola is shown in dependence on the number of detected photons. Differently sized  $L$  (blue, red, yellow) are compared to a 2D localization precision of an idealized camera (purple), showing the advantage of MINFLUX nanoscopy compared to conventional single molecule localization methods with respect to the efficiency in the use of photon.

### 1.3 Why do Fluorophores Matter?

In conclusion, the established approaches to super-resolution microscopy explained above share two specific requirements regarding the fluorescent molecules, namely photostability and discernable photophysical states. The introduction of the MINFLUX concept softened the demand for the former by the concept's inherent photon efficiency. However, typical imaging or tracking experiments do not deal with a single fluorophore in the region of interest, but many. In this regard, MINFLUX shares the requirement of having only one emitter in the on-state per diffraction-limited spot with the coordinate-stochastic approaches and puts discriminable molecular states even more into the center of current fluorophore design and development, including the presented thesis.

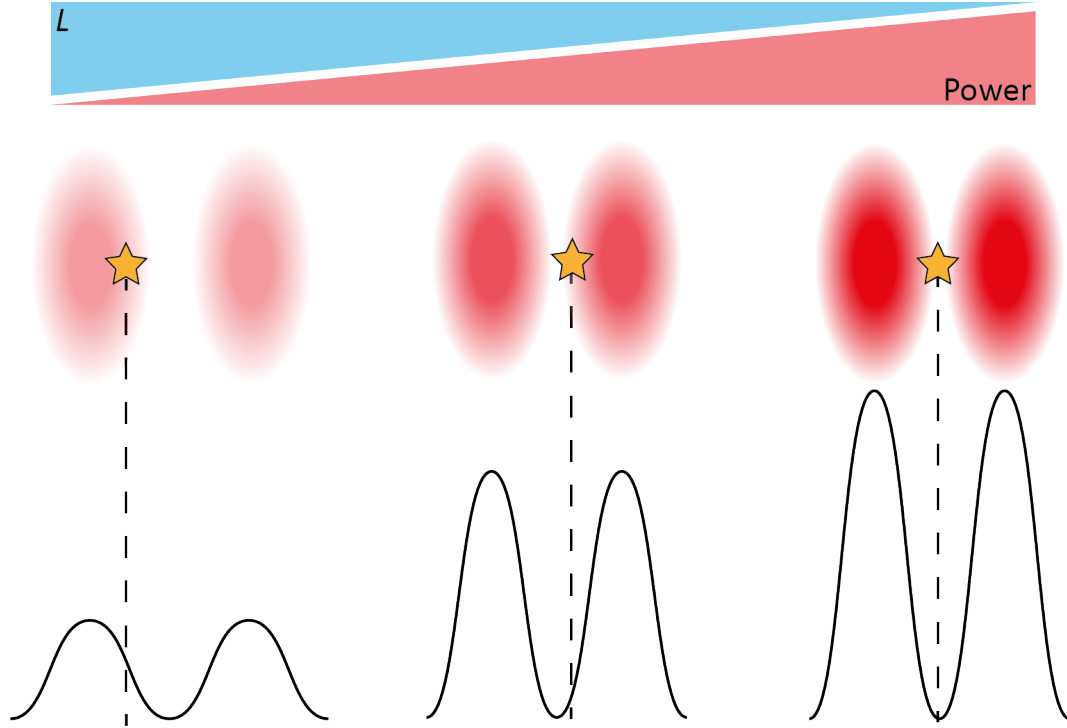


Figure 1.9: **Iterative MINFLUX approach.** Decreasing the  $L$  while increasing the excitation intensity yields an increased localization precision, upon which the subsequent localization step builds. Due to the position refining of the excitation intensity distribution with respect to the fluorophore of interest at each step, the experienced intensity of the molecule stays low.

In section 1.1, fluorescent molecules fulfilling this requirement are described. In case of reversible switching dyes, the compliance with criterium of only one fluorescent molecule active per diffraction-limited area can be assessed via the duty cycle ( $DC$ ), which depends on the durations of the on- and off-state:

$$DC = \frac{T_{On}}{T_{On} + T_{Off}} \quad . \quad (1.7)$$

The probability that a maximum of only one molecule is in the on-state can be estimated by binomial coefficients

$$P(0, N) = \binom{N}{0} \cdot DC^0 \cdot (1 - DC)^N \quad (1.8)$$

$$P(1, N) = \binom{N}{1} \cdot DC^1 \cdot (1 - DC)^N \quad , \quad (1.9)$$

for 0 or 1 event (photon burst) in an ensemble of  $N$  molecules in a diffracted-limited area with a  $DC$  given by equation 1.7. Figure 1.10 shows a simulation of equation 1.8 and displays the probability for a maximum of one single molecule event in a diffracted-limited spot for a reversible blinking fluorophore. While a two-emitter system can have a duty

cycle up to 0.2 still ensuring a single event in 95% of the cases, typical systems between 50 and 1000 molecules demand duty cycles between 1:100 and 1:2000. Indeed, typical duty cycles of photoswitches used in super-resolution imaging of biological samples lie in that order of magnitude [45].

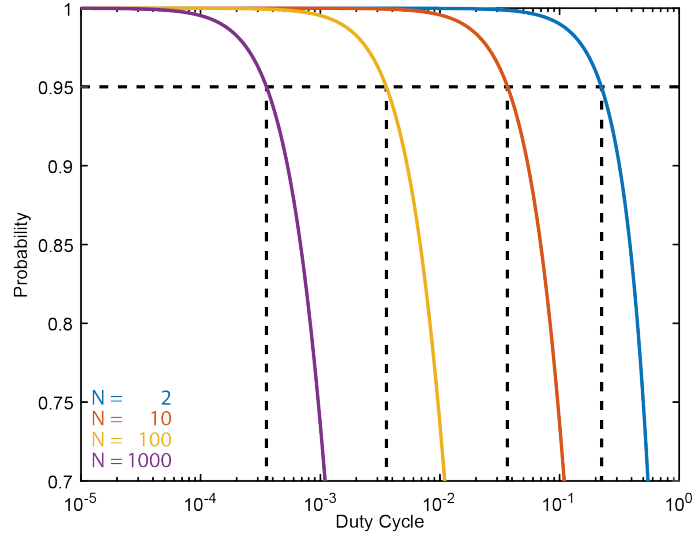


Figure 1.10: **Single fluorophore event probability in dependence on the duty cycle.** The probability for an event (photon burst) originating from a single fluorophore is simulated for different numbers of molecules per diffraction-limited spot. The duty cycle and the discrimination criteria are strongly correlated.

As the reversible switching process of single molecules obeys a stochastic distribution, the probability of observing a specific molecule in an ensemble of  $N$  molecules is determined by  $P_{k1+} = 1/N$ . Thus, the probability of not observing the molecule is described by

$$P_{k1-} = P_F^k = \left(\frac{N-1}{N}\right)^k \quad (1.10)$$

with  $k$  being the number of observed events. This equation allows for the estimation of the minimally required number of events to observe each molecule in the ensemble at least once. For a nuclear pore complex ( $N=8$  with one fluorophore at each of the eight corners),  $k \geq 22$  observations on average are necessary to observe each dye at least once with a probability of 95%.

In contrast, photoactivatable dyes only go through one on/off-switching cycle, making the specification of a duty cycle obsolete. The criterium of only one dye per diffraction-limited spot can be fulfilled by tuning the activation energy of the source (e.g. UV light). The loss of complexity is paid with the probability of the detection of a specific fluorophore, as can be seen in figure 1.11. The probability distributions are depicted in dependence on the number of detected corners of an idealized nuclear pore complex (eight

corners) for different detection ratios (DR) and number of fluorophores per corner ( $n$ ). Still, with a detection ratio of 75% for only 10% of the nuclear pore complexes, all eight corners are detected, while a detection ratio of 95% increases the probability by a factor of 6.6. Increasing the number of fluorophores per corner (see figure 1.11B) increases the probability of detecting all corners 6-fold, highlighting the importance of a additional try for lower detection efficiency.

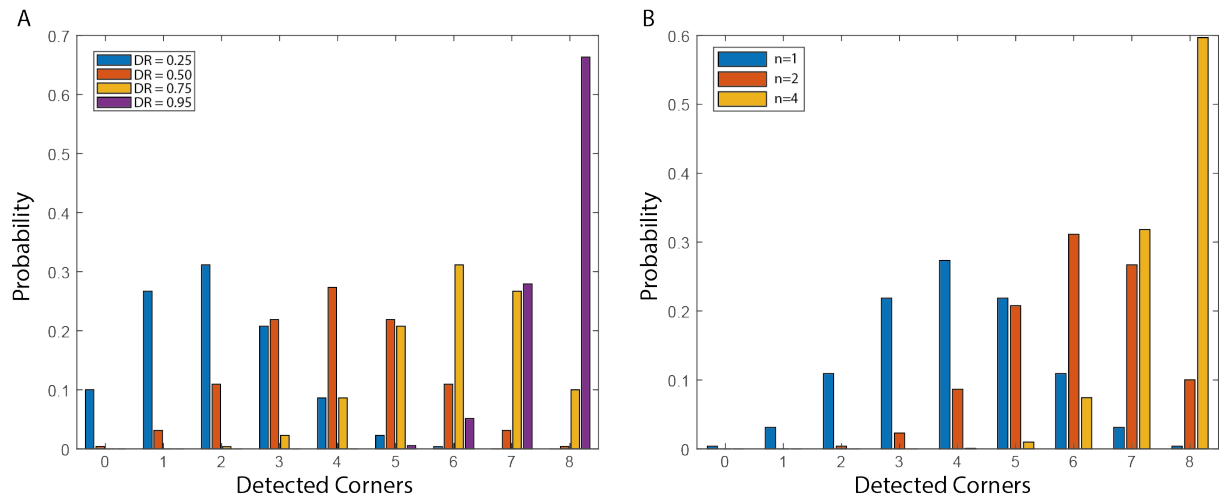


Figure 1.11: **Probability distribution of detected events for an idealized nuclear pore complex.** A) The probability distribution of detected corners in an idealized nuclear pore complex for different detection ratios (DR) for  $n = 1$  fluorophore per corner. B) The probability distribution of detected corners in an idealized nuclear pore complex for different numbers of fluorophores per corner ( $n = 1 - 4$ ) for a detection ratio of 50%.

# Chapter 2

## Material and Methods

The main scientific work of the present thesis deals with the characterization of novel fluorescent emitters for optical nanoscopy. Therefore, a versatile optical setup was built, enabling data acquisition in a confocal and a wide-field configuration. The detailed description of the setup can be found in section 2.1.

To investigate novel dyes, two complementary approaches were used. In one of them, data of the fluorophores, was acquired in a single molecule environment with the aid of confocal and wide-field microscopy. The detailed sample preparation can be found in section 2.3.1. The second approach characterizes the dye in a biological relevant system, i.e. imaging them with STORM and MINFLUX nanoscopy, in both fixed and live cell samples. The preparation of these samples can be found in section 2.3.2.

Data acquired from these measurements was evaluated with the aid of dedicated software written in Matlab. The methodology of the data analysis is described in section 2.2.

In a last step, the obtained results were used for the iterative optimization of the MINFLUX measurement routines of a commercial MINFLUX system (Abberior Instruments, Göttingen, Germany) to find the best imaging conditions for the novel probes. The quantitative image analysis is described in section 2.2.

## 2.1 Instrumentation

A scheme of the optical setup can be found in figure 2.1. For excitation, four different CW STM Lasers are used. They emit laser light at a wavelength of 642 nm (MPB Communications,  $P_{max} = 1000$  mW), 560 nm (MPB Communications,  $P_{max} = 1000$  mW), 532 nm (Laser Quantum,  $P_{max} = 1000$  mW) and 473 nm (Laser Quantum,  $P_{max} = 500$  mW). For photoactivation of fluorophores, two different CW UV lasers are implemented, providing laser light with a wavelength of 355 nm (Genesis Coherent,  $P_{max} = 100$  mW) and 405 nm (06-MLD Cobolt,  $P_{max} = 300$  mW). Light emitted by the laser is overlapped with the aid of different dichroic mirrors reflecting the respective wavelengths. Fast intensity control is done either via acousto-optical filters (AOTF1: PCAOM VIS, Crystal Technology Inc., AOTF2: AA.AOTF nC/A3-UV-Col351-363/TN) for STM lasers or via analog modulation of the diode laser (06-MLD Cobolt). An electronically controllable flipper allows to choose between two illumination beampaths, which enable either confocal or wide-field imaging. Before entering the fiber (Thorlabs P1-405BPM-FC-5, Thorlabs Inc. Newton, USA) of either beam path, the polarization of the excitation light is tuned by a half wave plate ( $\lambda/2$ , achromatic half-wave plate, B.Halle). Matching the polarization of the incoming light with the fiber polarization axis results in a clean output of the mode and a parallel character of the different wavelengths. The further explanation of the two beampaths can be found in their respective sections 2.1.1 and 2.1.2.

### 2.1.1 Confocal Setup

Polarization of light exiting the fiber is cleaned up by a Glan-Thompson polarizer (GTH5M, Thorlabs) and passes a non-polarizing beamsplitter (BS034, Thorlabs). The latter is guiding a small portion of back-reflected excitation light from the sample to a photon multiplier tube (PMT, Perkin Elmer MD-963, Excelitas Technologies Corp. former Perkin Elmer, Inc. Waltham USA), which detects refractive index changes and simplifies both searching for the imaging plane and the adjustment of the correction ring. Afterwards, the laser light is guided through another AOTF (see section 2.1, AOTF3, AA Opto Electronic, Orsay, France), filtering with respect to the corresponding wavelength. The light is then coupled into an analog galvanometer scanner consisting of four scanning units (mirrors: 6210H, servo driver: MicroMax<sup>TM</sup>671, Cambridge Technology) enabling bi-directional scanning. Light enters the microscope body of a Leica DMI8 via its infinity back-port providing a wide chromatic correction range. For all measurements in the context of this thesis, a Leica HCX PL APO NA 1.46 Oil corrected objective lens (Leica Microsystems, Wetzlar, Germany) was used.

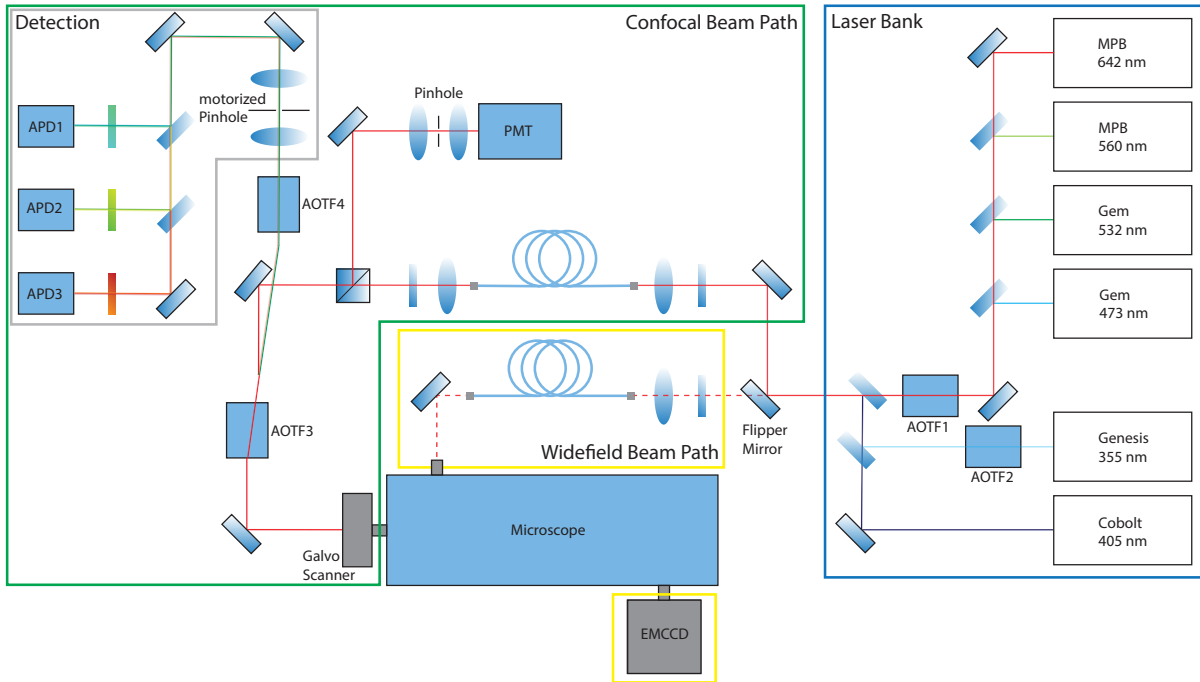


Figure 2.1: **Scheme of the custom-built experimental setup.** Multiple excitation lasers in the depicted wavelengths are tuned by an AOTF or by analog input (blue). With an electronic controllable flipper mirror the confocal (green) or the wide-field (yellow) beam path can be chosen. For the confocal beam path, an analog galvanometer quadscanner guides light into a Leica DMI8 microscope body, enabling confocal scanning of the sample. For wide-field measurements, light enters the microscope body via a tube lens. The fluorescence light is either detected in the detection module via avalanche photo diodes (confocal, grey) or via an EMCCD camera (wide-field, yellow). The hardware is controlled by a computer running a dedicated software written in LabView for data recording and parameter control, while a field programmable gate array board takes over the real-time measurement control.

Table 2.1: **Overview of bandpass filters that are used at low angle of incidence to act as dichroics in the filter cascade.** All filters were manufactured by IDEX Corp., Lake Forest, USA

Channel 1 (green)	DM 1	500 – 550 nm	Semrock 525/50 Brightline HC
Channel 2 (yellow)	DM 2	574 – 626 nm	Semrock 600/52 Brightline HC
Channel 3 (red)	DM 3	662 – 800 nm	Semrock 731/137 Brightline HC

The sample is placed on a custom-built sample stage allowing for precise measurements with samples mounted on regular objective slides and in live-cell imaging chambers. It is powered by piezo linear-actuators (SLC1740, Smaract GmbH, Oldenburg, Germany) and has a positioning precision below 1 nm with a maximum travel distance of 21 mm.

Fluorescence light emitted by the fluorophores inside the sample is collected by the objective lens, descanned passes AOTF3 suppressing the excitation light. The crystal of a second, passive AOTF (AOTF4, AA Opto Electronic, Orsay, France) guides all emission light on the same axis independent of its wavelength. To facilitate a high confocal confinement of the emission, the light is focused into a motorized pinhole (MPH, Thorlabs MPH16-A, Thorlabs Inc. Newton, USA). The pinhole size can be adjusted from 25  $\mu\text{m}$  to 2 mm corresponding to 75 nm to 6  $\mu\text{m}$  in the object space with the used objective lens. After collimating the beam, it is split into three different detection channels by dichroic mirrors, listed in table 2.1. To efficiently suppress excitation light or light of any unwanted wavelengths, two filters per channel are implemented in each corresponding detection path. Detection of the fluorescence light is carried out by avalanche photo diodes in each of the windows (PerkinElmer SPCM-AQR-14, Excelitas Technologies Corp. former PerkinElmer, Inc. Waltham USA, Excelitas SPCM-AQRH-13, Excelitas Technologies Corp. Waltham, USA).

### 2.1.2 Wide-field Setup

Light exiting the fiber enters the side-port through the tubus lens of the microscope body. A tiltable optical mirror between the fiber and the tubus lens allows for positioning the focus of the beam in the back focal plane of the objective lens. This results in a tilted collimated beam exiting the objective lens, enabling so-called HILO microscopy (Highly Inclined and Laminated Optical sheet), where only a thin sheet of the laser beam illuminates the sample, increasing signal-background ratio [46].

Fluorescence light emitted by probes in the sample is collected by the objective lens and passes the respective dichroic mirror of the filter wheel separating excitation and emission light. A second bandpass filter ensures further suppression of the excitation light and light of any other unwanted sources. The combination of dichroic mirrors and filters can be found in table 2.2. Passing a telescope the fluorescence signal exits the microscope body on a side-port through a tubus lens and illuminates the CCD chip of an EMCCD camera with a pixel size of  $16\ \mu\text{m}$  (iXon DVU897, Andor Oxford Instruments, Abingdon UK). The telescope has a magnification factor of 1.6, which leads to a pixel size of  $100\ \text{nm}$  in the object space.

Table 2.2: **Overview of bandpass filters and dichroics used in the respective filter cubes enabling detection channels of different colors.**

Channel 1 (blue)	400 nm (T 400 LP)	435 – 485 nm (Chroma ET460/50 M)
Channel 2 (green)	505 nm (T 505 lpxr)	508 – 598 nm (SR 550/88 BL HC)
Channel 2 (yellow)	560 nm (SR HC 560)	565 – 605 nm (Chroma ET585/40 M)
Channel 4 (orange)	580 nm (SR HC R561)	589 – 739 nm (SR 665/150 BL HC)
Channel 5 (red)	660 nm (SR HC 660)	665 – 732 nm (Chroma ET700/75)

### 2.1.3 Data Acquisition

The fast measurement procedures are controlled by a field programmable gate array board (FPGA, PCIe-R7852r, National Instruments, Austin, USA). It operates at a base clock of  $100\ \text{MHz}$  enabling real-time control of the data acquisition. It has eight analog outputs (AO) with a precision of 16 bit updating at a speed of  $1\ \text{MHz}$ , as well as eight analog inputs (AI) with the same precision operating at  $750\ \text{kHz}$ . The outputs are used to control the galvanometric units, the AOTFs, the APDs and the  $405\ \text{nm}$  UV laser. Other components (e.g. EMCCD detector) of the optical setup can also be controlled via one of the 96 digital in/outputs (DIO).

Via a dedicated software written in LabView communicating with the FPGA, the measurement configuration is controlled. The software was primarily written by Johann Engelhardt (Ph.D., Optical Nanoscopy, MPIMR, Heidelberg). Minor changes were implemented by the author.

For operating the EMCCD camera, the manufacturer’s software (Andor Solis) was used. While acquiring data, the camera (primary) sends a signal to the AI of the FPGA (secondary), which allows to change the measurement’s configuration (i.e. activation or excitation sequences and power) within the software in real-time.

## 2.2 Data Analysis

For the data analysis in the context of this thesis, mostly dedicated scripts written in Matlab were used. The scripts were primarily written by Mariano Bossi (Ph.D., MPIImR, Heidelberg). Minor changes were implemented by the author.

### 2.2.1 Single Molecule Experiments

MINFLUX is a single emitter localization technique, which makes dye characterization at the single molecule level for novel MINFLUX probes essential. As stated in chapter 1 the localization precision for a single localization in MINFLUX also depends on the parameter  $L$  of the intensity distribution pattern displacement in the vicinity of the fluorophore of interest and therefore softens the demand for the number of detected photons ( $N_{Ph}$ ) compared to coordinate-stochastic methods. The speed of the localization process itself is limited by the rate with which the dye can emit the required number of photons. For imaging on the other hand, only one molecule in a diffracted-limited spot must be in an on-state while localizing [7]. This can be accomplished by different, distinguishable states, which can be induced (e.g. photo-switching, or photoactivation) or be of stochastic nature.

Acquired single molecule data from either wide-field or confocal microscopy measurements were transformed into single molecule time traces via dedicated routines written in Matlab or LabView. The time traces were then further evaluated via dedicated scripts in written in Matlab.

In the first step, the signal of the single events was separated from noise by setting a photon threshold. For this, an approximated threshold well above the noise was taken and the signal underneath the threshold was plotted into a histogram. For wide-field measurements a Gaussian distribution was fitted to the distribution. By calculating  $4 \cdot \sigma$  with respect to the mean, 99.999% of the noise could be separated from the signal. This calculated threshold was used for further analysis of the data. For confocal measurements, a Poissonian distribution was used. A threshold excluding 99.994% of the noise was calculated. Figure 2.2 shows signal separated from noise by this method, and also, the binarized traces obtained after applying the threshold.

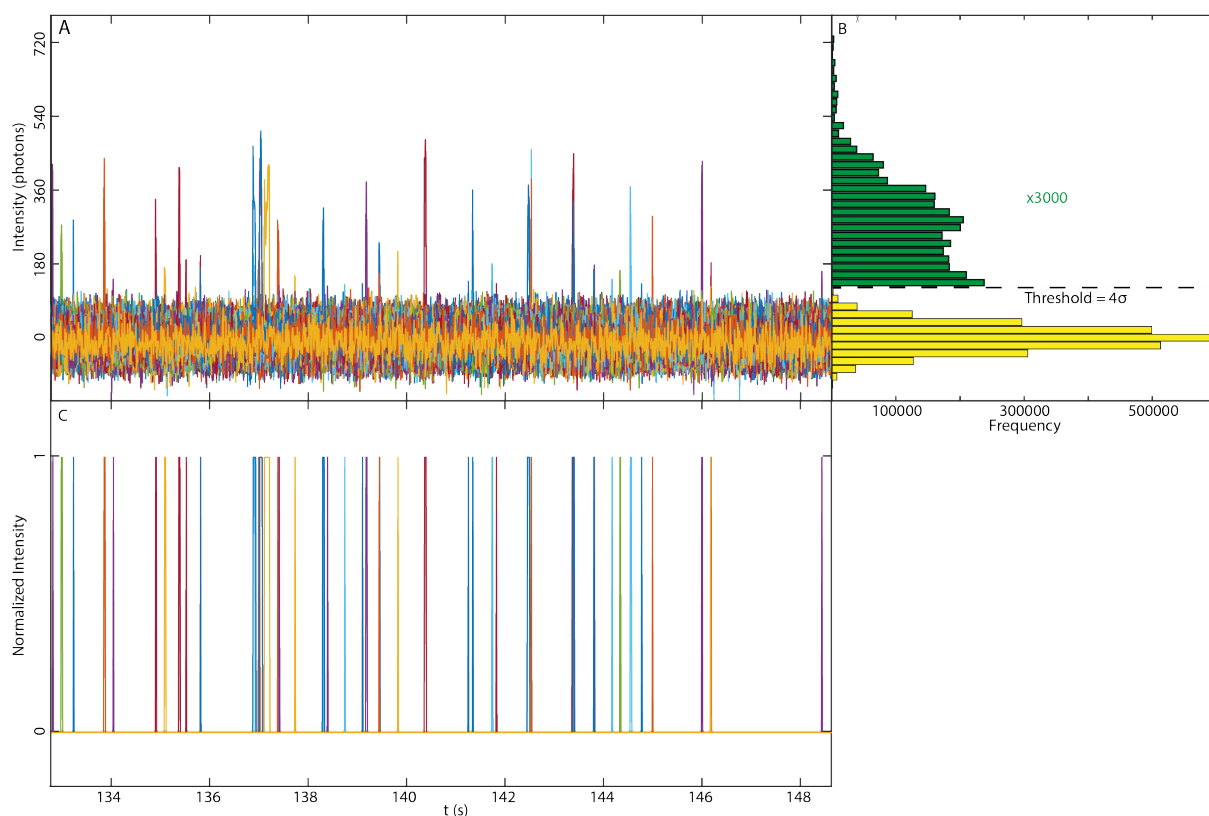


Figure 2.2: **Data separation of the single molecule time traces.** A) The particular traces are stacked showing individual spikes caused by photon bursts of single fluorophores in the sample. B) The signal is separated by fitting a Gaussian distribution to the background and setting a threshold of  $4\sigma$  with respect to the mean of the distribution. C) The binarized events used to evaluate on- and off-times are plotted.

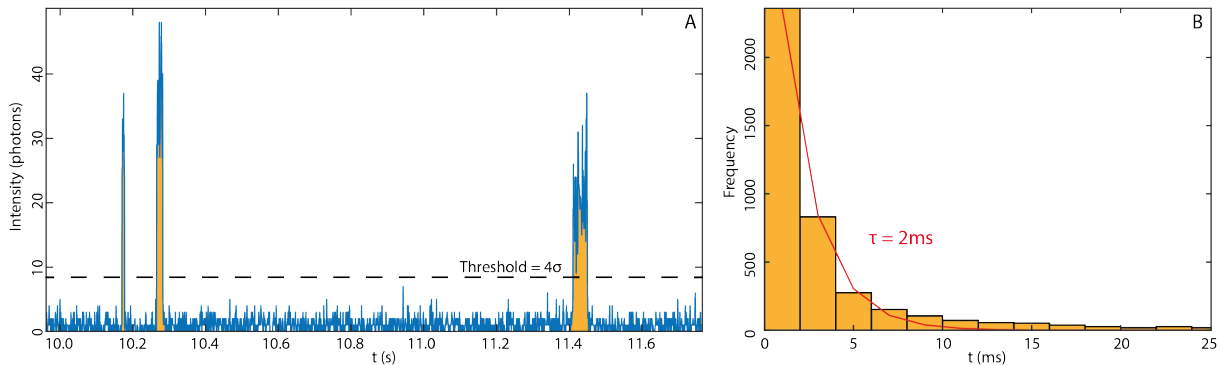


Figure 2.3: **Evaluation of the single molecule data.** A) An excerpt of a single molecule time trace. Areas contributing to the number of photons and the rate are shown in orange. B) A histogram of all on-events. The exponent of the exponential decay is the expected value of the duration of the on-event.

As the characteristics of the respective fluorescent switches strongly influence the speed and efficiency of the MINFLUX imaging process, studies on on- and off-switching properties are necessary. Therefore, the focus of the dye characterization within this thesis lies on the number of photons per on-event  $\text{Ph}_{Cy}$ , the photon rate, on-time of the fluorescent state  $T_{On}$  as well as in specific cases, also on the duty cycle ( $DC$ ), number of on-state cycles  $N_c$ , or activation time  $T_{act}$ .

The number of cycles ( $N_{Cy}$ ) was obtained by calculating the mean event number of all binarized traces (figure 2.3A) and subtracting the mean noise from the part of the trace in which the dye was in off-state, to factor in the background. The photons per cycle ( $\text{Ph}_{Cy}$ ) were determined by forming the quotient of  $\text{Ph}_{Cy} = N_{Ph}/N_{Cy}$ . Since starting and ending points of the events could be obtained from the binarized traces,  $T_{On}$  and  $T_{Off}$  were calculated for each event. Plotting the events in a histogram displays a (bi)-exponential distribution with the exponent giving the expected value of  $T_{on}/T_{off}$  (figure 2.3B). The duty cycle was calculated following equation 1.7.  $T_{act}$  is the average time until the activation light induces the uncaging mechanism and can be obtained by a exponential fit from the histogram of the first off-time  $T_{off,1}$ . The average photon rate of the dye was calculated by dividing  $\text{Ph}_{cy}$  by  $T_{on}$ .

**Spontaneously Blinking Dyes** are fluorophores which switch reversibly between an on- and off-state, absorbing and emitting light only in the former. This results in a couple of cycles  $N_c$  with limited photon number  $\text{Ph}_{Cy}$  for localizing the fluorophore. The duration of the on-state  $T_{On}$  sets the time frame of the localization, while  $T_{Off}$  dominates the duty cycle ( $DC$ , see equation 1.7) and therefore impacts the density of labeling ( $DOL$ ) of the sample.

**Photoactivatable Dyes** are initially in an off-state in which they do not emit photons under excitation. Irradiation with a shorter wavelength, typically UV light, leads to uncaging of the emissive molecule. The activation time  $T_{act}$  is crucial as one has to ensure excitation of only a single molecule per diffraction limited spot. The probe has a single on-state in which it emits photons  $Ph_{Cy} = N_{Ph}/N_{Cy} = N_{Ph}$  after excitation. The emission proceeds with a rate in a time window  $T_{On}$ , determining the speed of a localization. Possessing only one cycle the duty cycle becomes obsolete.

### 2.2.2 Image Processing

In context of the presented thesis, primarily single molecule localization methods (SMLM) and MINFLUX imaging was performed. Both single emitter imaging techniques result in a list of localizations with parameters (e.g. intensity, duration) for each event. Analyzing this data, enables the reconstruction and the rendering of the imaged region of interest (ROI). Furthermore, dye or structure specific parameters can be extracted subsequently.

**SMLM** raw data is initially represented by a certain number of camera frames (typical several thousand) possessing pixel-bound intensity value. After stating the camera specifications a super-resolution image could be reconstructed with the aid of the ImageJ plugin ThunderSTORM [47]. The plugin detects single events in a stack of frames by the detection of pixels exceeding a specific intensity threshold and by subsequent Gaussian fitting. Moreover, it allows correction for drift of the data by correlation and emitter merging of events stretched over several frames. More specific description of the algorithms can be found in Ovensný et al. [47].

With the aid of a dedicated script written in Matlab both the initial data and the super-resolution images were further filtered. For rendering, Gaussians with a pixel size corresponding to the mean of the localization uncertainty were plotted.

**MINFLUX** raw data is initially represented by a list of localizations with specific parameters. The data were processed by using dedicated scripts written in Matlab. In the first step, localizations with identical event IDs (meaning the microscope counts the localizations as same emission event) were analyzed by Matlab's density-based spatial clustering of application with noise (DBSCAN, see figure 2.4, [48]) algorithm. On the one

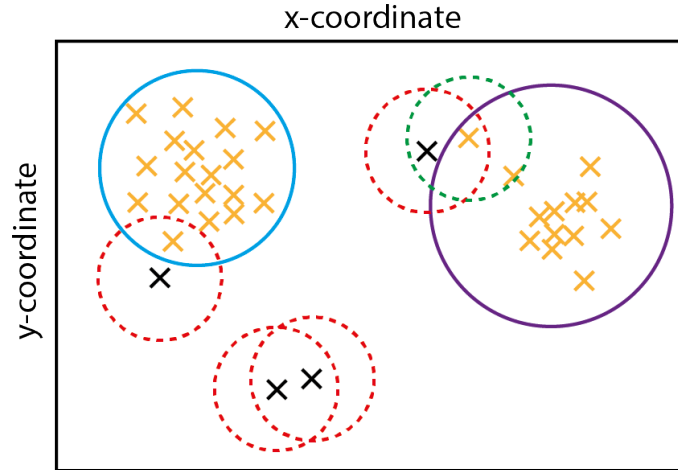


Figure 2.4: **Visualization of DBSCAN.** The figure shows a scheme of a possible MINFLUX event consisting out of multiple localizations. DBSCAN calculates distance between single localizations and filters for clusters with sufficient localizations (in this case two) in a set radius. In this scheme localizations with two neighbors inside the radius (stashed lines) are marked as valid (yellow) resulting in two clusters (blue, purple cycle), which are tagged as different events

hand it allows separation of two and more localization clusters inside one event ID and on the other hand it provides filtering of noise. In the next step, the data were filtered for outliers, by plotting x- and y-values for all localizations with respect to their mean in a 2D histogram and by fitting a 2D Gaussian (see figure 2.5A). All data above  $1.65\sigma$  with respect to the mean of the normal distribution were filtered out, representing the 10% of all localizations with the largest uncertainty [34](figure 2.5B red panel). Additional filtering with respect to the dye or sample characteristics was used by applying filters to measurement time, photon rate or detected photons.

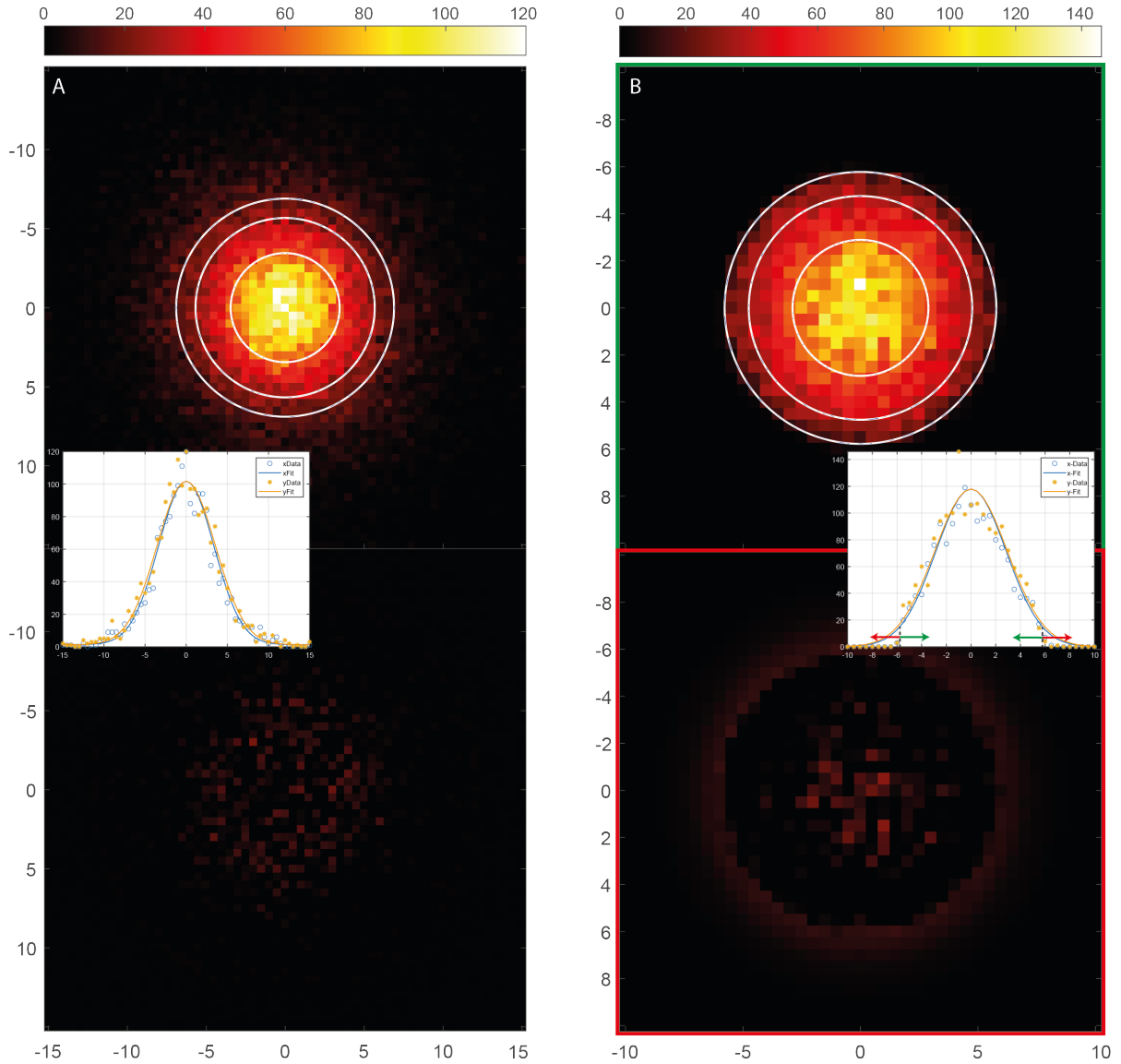


Figure 2.5: **Outlier filtering method.** A) Localizations plotted with respect to the mean of the event after DBSCAN. Residuals below shows filtering after a 2D Gaussian (1D fits in x- (blue line) and y-direction (orange line) shown in the inset). B) Localizations plotted with respect to the mean of the event after filtering the 10% outliers ( $>1.65\sigma$ ) obtained from A) (green panel). Residuals are shown in the red panel. A 1D fit in x- and y-direction shows the Gaussian distribution of the localizations.

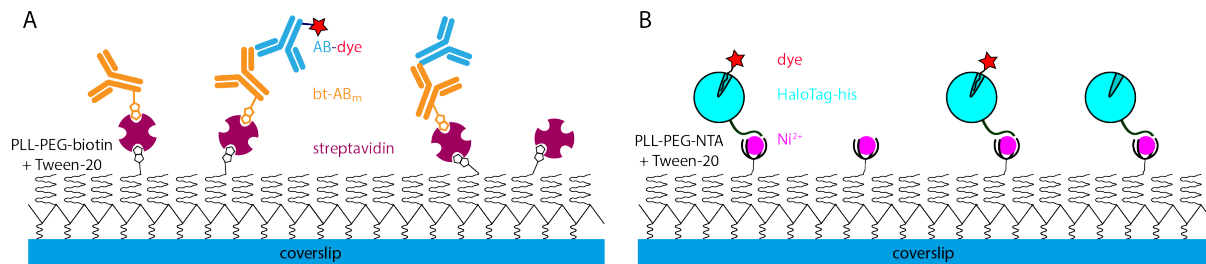


Figure 2.6: **Single Molecule Sample Setup.** A) Immobilization of the dye of interest by antibodies. The primary antibody is conjugated with biotin, which is linked via a streptavidin bridge to a biotinylated polymer (PLL-PEG). B) The HaloTag compound of the dye specifically labels HaloTag, which is immobilized via its HisTag and a  $\text{Ni}^{2+}$  to a PLL-PEG-NTA layer forming a chelate complex.

## 2.3 Sample Preparation

In the following section, the preparation of all samples used in this thesis is described. The detailed protocols are listed in the supplements 7.4.

### 2.3.1 *In Vitro* Experiments

**Samples for Photophysical Characterization of Single Molecules** allowed the photophysical evaluation of the examined dye in a nanoscope relevant system. For the sake of reproducibility, the focus of the sample setup based on reported protocols [49, 50], optimized by Lukas Scheiderer, Optical Nanoscopy, MPIImR, Heidelberg, laid on simplicity. A concentration screening, ensured sparse distribution. A sketch can be found in figure 2.6.

To label with biotinylated antibodies a plasma cleaned coverslip was incubated with a biotinylated poly-L-lysine layer (0.2 mg/ml in PBS) supplemented with 1% (v/v) Tween-20 (Susco AG Inc.). A streptavidin (10  $\mu\text{g}/\text{ml}$ ) bridge between the biotinylated antibody (1:100) allowed specific binding with a secondary antibody (1:100) labeled with the dye of interest (DOL= 0.3) and ensured maximum degree of freedom [49]. For the immobilization of dyes with HaloTag or anti-GFP nanobodies, a PLL-PEG layer with a nitrilotriacetic acid group (NTA) (0.2 mg/ml in PBS), supplemented with 1% (v/v) Tween-20, was used (Susco AG Inc.). After incubation with  $\text{Ni}^{2+}$  (2  $\mu\text{g}/\text{ml}$  in  $\text{dH}_2\text{O}$ ), the HaloTag ( $\approx 20 \mu\text{M}$ ) was added and its HisTag formed a chelate complex with the NTA and the  $\text{Ni}^{2+}$  [50]. In case of anti-GFP nanobodies, incubation with GFP-HisTag was done to ensure specific binding of the anti-GFP nanobody with the fluorophore of interest. All reagents are listed in section 7.4.

**Nanobodies for Resolving the Fluorescent Label** were labeled with PAX<sub>560</sub> maleimides (DOL=2) [34]. For the experiment FluoTag®-X2 anti-Rabbit IgG nanobodies (NanoTag, Göttingen, Germany) were chosen possessing two cystein linkers at the C- and N-terminal of the nanobody corpus. The nanobodies were applied to the coverslip by spin coating and mounted in Mowiol.

### 2.3.2 *In Cellulo* Experiments

All cell lines were cultured in a CO<sub>2</sub> an incubator (37°C, 5% CO<sub>2</sub>, 95 % r.h.). For COS-7 (Cell Lines Service), HK-2xZFN-mEGFP-Nup107 (Cell Lines Service) and U2OS-Vim-Halo (AG Stefan Jakobs, Göttingen) cells, Dulbecco's modified Eagle medium (DMEM) was used as culture medium, supplemented with 10% (v/v) fetal bovine serum (FBS, ThermoFisher 10500064) and 1% penicillin-streptomycin (Gibco 15140122). For U2OS-Nup96-Halo (Cell Lines Service) McCoy's 5A medium (Gibco 26600023) was used as culture medium, supplemented with 10% (v/v) fetal bovine serum (FBS, ThermoFisher 10500064), 1% penicillin-streptomycin (Gibco 15140122), 2 mM GlutaMAX, 10% MEM (11140035, ThermoFischer) and 1mM sodium pyruvate (31966, ThermoFisher). The cells were plated on glass coverslips (18 mm diameter) for 24-48 h prior to fixing or labeling.

For labeling tubulin, vimentin or nuclear pore complexes with antibodies, green monkey kidney fibroblast COS-7 cells were used. For tubulin or vimentin staining, cells were washed with PBS and then fixed with MeOH (cooled to -20°C) for 5 min. After blocking with 2% bovine serum albumin (BSA) blocking buffer (BB) for 45-60 min, cell were incubated with the primary antibody against the structure of interest for 60 min at r.t. (or overnight at 4°C) in BS and subsequently washed twice with BB. Then, they were incubated with a secondary antibody carrying the dye of interest for 60 min at r.t. In case of nuclear pore complexes labeled with antibodies, the protocol of the manufacturer (NanoTag Biotechnologies) was adapted (see section 7.4). A detailed protocol can be found in 7.4. Briefly, the cells were washed with PBS and then fixed with Paraformaldehyde (PFA 4%). Following a quenching step, the cells were blocked and permeabilized for 30 min (0.2% Triton in BB). Afterwards sequential labeling with the primary antibody and secondary antibody or nanobody with the dye of interest was done as described above.

For HeLa HK-2xZFN-mEGFP-Nup107 cells, the detailed protocol can be found in [51, 52] and is attached in the supplementary section 7.4. Briefly, HeLa HK-2xZFN-mEGFP-Nup107 were washed with PBS and prefixed in PFA for 30 s. After a permeabilization step

with Digitonin (25µg/ml in transport buffer), cells were blocked and labeled with the dye of interest linked to an anti-GFP nanobody. A second fixation and permeabilization step with 0.4% Triton was performed, before the cells were again labeled with the nanobody.

U2OS-Vim-Halo and U2OS-NUP96-Halo were used for both live-cell imaging and fixed cell imaging. In both cases, the cells were labeled live with the Halo derivative of the dye of interest in DMEM++ described above, for 24-48h. In case of U2OS-NUP96-Halo, the cells were washed with PBS and fixed with 4% PFA. After quenching, permeabilization and blocking counter labeling was performed with a primary antibody against NUP153 and a secondary nanobody. The detailed protocols can be found in section 7.4.

A detailed protocol for U2OS-CRISPR-NUP96-mMaple clone #16, which were treated according to [8] can be found in section 7.4. Briefly, the cells were prefixed in PFA. After a permeabilization step (Triton 0.2%) a second additional fixation step was performed followed by quenching of the sample. All used reagents can be found in the tables of section 7.4.

For live-cell imaging samples were washed twice with FluoBrite (Invitrogen) supplemented with 10% FBS and 2% GlutaMAX and mounted in the very same.

All used cell lines reagents, proteins with their concentrations with detailed protocols are listed in 7.4

# Chapter 3

## Spontaneously reversible On-Switching Dyes

This chapter contains the studies of spontaneously blinking, red silicon-rhodamine dyes. The chapter begins with a brief introduction setting the approach of stochastic blinking in general into the context of super-resolution microscopy, especially MINFLUX nanoscopy (section 3.1).

A comprehensive study in a single molecule environment was designed and realized (section 3.2.1), evaluating characteristics of the fluorophores important for MINFLUX nanoscopy.

The suitability for biological samples is shown in section 3.2.2, by labeling several different structures both in fixed and live-cells and imaging them in STORM microscopy.

Finally, the suitability as fluorescent probes for MINFLUX nanoscopy was demonstrated by imaging nuclear pore complexes (NPC) stained via different labeling strategies (see section 3.2.3). NPCs suit as a standardized sample in nanoscopy [52]. Thus, the system allowed a further optimization of the MINFLUX imaging process, as well as an analysis of the data with the focus on localization speed.

A conclusive discussion comparing the results of this thesis with previous work is done in section 3.3.

The study presented in this chapter resulted in a publication by Rimmel et al. (submitted, [53]). The dyes were synthesized by Alexey Butkevich (Ph.D, Optical Nanoscopy, MPIImR, Heidelberg). Analysis of the data was performed in exchange with Mariano Bossi (Ph.D, Optical Nanoscopy, MPIImR, Heidelberg).

### 3.1 Introduction and Aim

Thermally self-blinking dyes are a specific group of reversible on-off switching fluorophores without photoinduced reactions, mainly used in STORM imaging [21, 30, 54–58], while a first experiment showing proof of principle measurements in MINFLUX nanoscopy has been done in 2021 [59]. As opposed to photoinduced blinking dyes (e.g. Cyanines), also utilized in stochastic super-resolution microscopy [60] and MINFLUX nanoscopy [7–9], the blinking mechanism does not rely on photochemical reactions, but on thermal ones. Their two or more state systems only absorb excitation light in the on-state with subsequent emission of fluorescent light.

The overall rising interest in utilizing thermally self-blinking dyes for fluorescence microscopy can be explained by several advantages that they possess compared to photoinduced blinkers. The first one lies in the mechanism itself, as photoinduced blinkers like cyanines (e.g. AlexaFluor647) make use of a external stimulations to achieve blinking. For the one mentioned, a non-fluorescent dark state is induced by the excitation light ( $\lambda = 640$  nm) and fluorescent recovery by UV illumination ( $\lambda = 405$  nm) [60, 61]. First of all, UV light damages cells making it undesirable for imaging in biological samples. Secondly, as excitation (and therefore imaging) and transfer into the dark state are coupled, one has limited control on localization speed. This results from the fact, that higher excitation power (for increasing the probability to transfer a fluorophore into dark state and therefore speed up the imaging process), results in an increased bleaching rate, uncontrollable triplet state blinking and a higher background level. The latter is crucial for MINFLUX imaging, since the zero of the excitation intensity distribution determines the localization quality. Furthermore, photo-induced blinkers often make use of complex redox blinking buffers, consisting of enzymatic systems and multiple chemicals like thiols or reducing agents, complicating sample preparation, as well as precluding live-cell measurements. Moreover, recent studies on the interaction of fluorophores with sub 10 nm distances show energy transfers between molecules with absorbance in their dark states (such as photoinduced blinkers), suggesting fluorophores with a non-absorbing dark state, as it is the case for stochastic blinking dyes [62]. Additionally, a non-absorbing dark state has no impact on the background level. Spontaneous self-blinkers work in every aqueous environment (by exchanging hydrogen-ions with the solvent) including live-cell media. As an example, HMSiR [21] can be named. Its equilibrium state at pH= 7.4 is shifted to the fluorescent state, yielding to rather long on-times of about 100 ms, compared to the dyes evaluated in this work. However, the blinking behavior with respect to the on- ( $T_{On}$ ) and off-times ( $T_{Off}$ ) can be chemically tuned by changing side groups of the molecule and thus adapted to the speed of the localization process. Last but not least, by the nature of all fluorescent imaging methods there is a non-zero chance of failing the detection or the valid

localization of the molecule. Especially for samples with only a few labels, reversibility can be advantageous, to ensure a sufficient apparent density of labeling.

Most spontaneously blinking dyes, especially molecules with a rhodamine or silicon rhodamine core, make the use of spirocyclization for switching between a fluorescent and a non-fluorescent state. In figure 3.1 the general structure of the evaluated silicon rhodamines, used for their far red emission light, and their mechanism is depicted. Functioning as a proton donator/acceptor in aqueous environment, the molecule switches between a closed form (colorless spirolactam) and an open form (red emitting xantilium). The equilibrium of these two states depends on the electrophilicity of the closed form, which can be influenced by the side groups  $Ar_1$  and  $Ar_2$  (detailed in figure 3.2). The two classes of dyes (each consisting out of three molecules), diverge in their spirolactam core ( $Ar_1$ ), which consists either of a thiophene or of a benzothiophene.

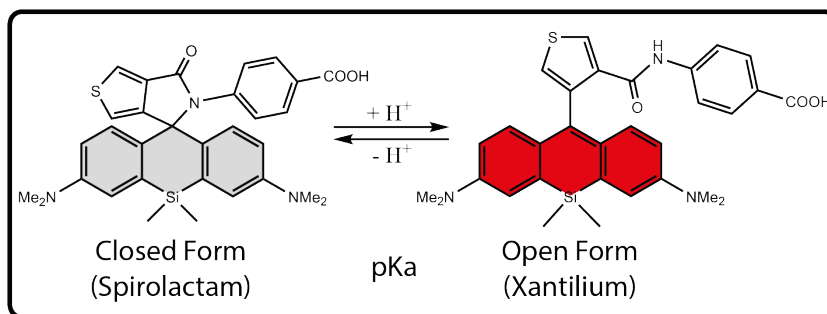


Figure 3.1: **General structure of the evaluated stochastic blinkers.** Shown are two different states the evaluated dyes can occupy. The dye switches predominantly between an open fluorescent form (Xantilium) by accepting a proton and a closed non-fluorescent form by proton-donation (Spirolactam).

Compared to previous studies on stochastic blinkers, like HMSiR [21] or others [58], the focus on the fluorophores evaluated in this thesis, was on their utilization for MINFLUX nanoscopy. MINFLUX achieves a localization precision of a few nanometers with orders of magnitude less than other super-resolution techniques utilizing blinking approaches (see figure 1.8), and thus localization times at similar detection rates are dramatically reduced. Typical on-times of spontaneous blinkers (like HMSiR:  $T_{On} \approx 100$  ms) or transition times into dark state for e.g. AF647, which appear to be a few hundreds of milliseconds in MINFLUX measurements (see section 3.3), do not exploit the full potential of MINFLUX nanoscopy.

## 3.2 Results

### 3.2.1 Photophysical Characterization

The photophysical properties of the fluorophores were measured with focus on the on-times ( $T_{On}$ ) and off-times ( $T_{Off}$ ), as well as the emission rate of the dye, as these parameters are from high importance to MINFLUX localization speed. While the first one, as described in section 1.3, is crucial to ensure emission of only one fluorescent probe in a diffracted limited spot, the third one determines the localization speed of single events. First bulk experiments show the minor absorbance of the fluorophores at  $\text{pH} = 7.4$ , implicating the predominance of the closed non-fluorescent form (see figure 3.2). This results hint to long off-times and short on-times on physiological conditions. Therefore, as explained in chapter 2, wide-field and confocal measurements with the same illumination intensity (at the fluorophore) were taken for each candidate, complementing each other in statistics on the one hand (off-times) and time resolution on the other hand (on-times).

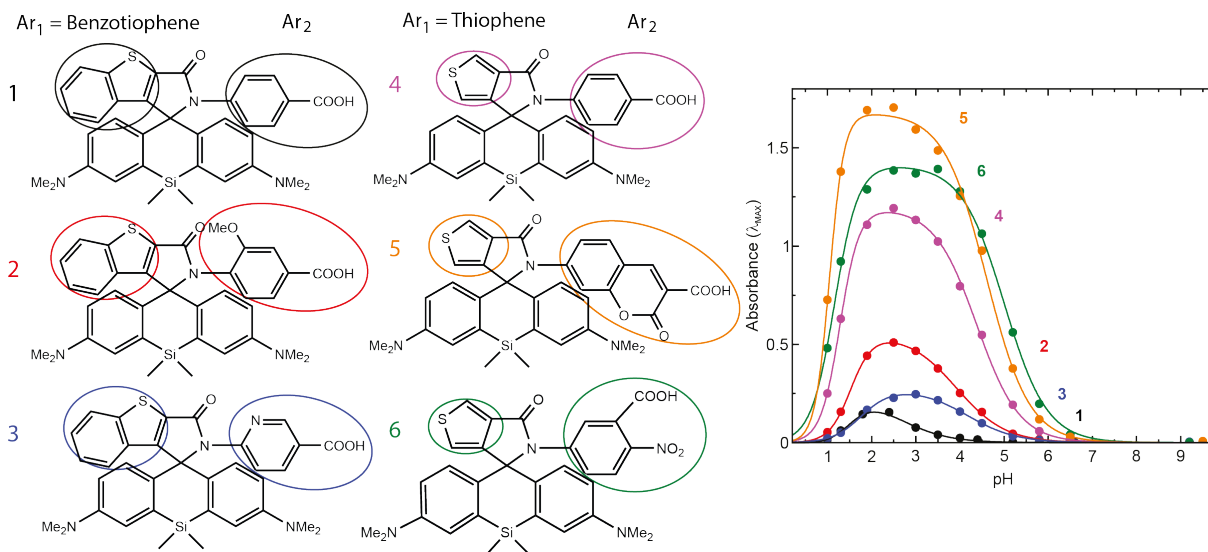


Figure 3.2: **Absorbance of the fluorescent probes in dependence on the pH-values.** The different shape of the absorption curves is caused by the different side groups  $\text{Ar}_1$  and  $\text{Ar}_2$  impacting the electrophilicity of the molecule. The absorbance at  $\text{pH} = 7.4$  is rather low, implicating a predominant non-fluorescent form at physiological pH.

Figure 3.3 depicts the histograms of the on-times for the six compounds bound to antibodies evaluated in this work. The measurements were obtained by confocal single molecule microscopy, as wide-field experiments showed an insufficient time resolution for measuring this parameter reliably (frame time  $> 5$  ms). The histograms are fitted with bi-exponential functions to take the multi-exponential behavior of the observed data better into account.

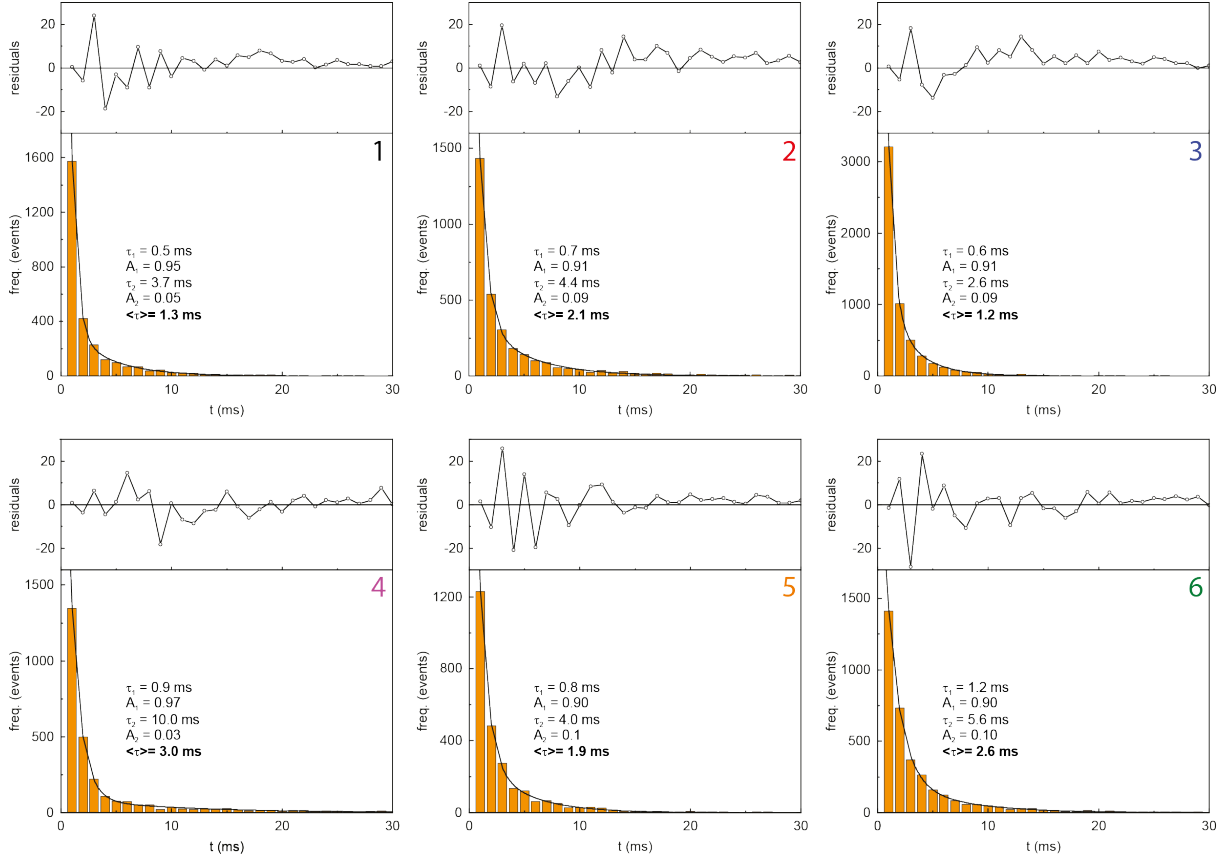


Figure 3.3: **Duration distribution of the on-events for the six compounds.** The histograms depict the distribution of the on-times for each compound measured in confocal single molecule microscopy. The distribution is fitted by a bi-exponential function (residuals on top) accounting for the multi-species behavior of the fluorophores.

Although one would suspect a mono-exponential behavior of a single stochastic species, like a population of same dyes, there is a possible explanation for the occurring phenomenon: As the probes do not only consist of the dye itself, but also are immobilized by a protein system (e.g. antibodies), they experience individual micro-environments. For instance, fluorophores labeled on different positions of the antibody might experience different local electric potentials influencing the switching mechanism. Nonetheless, the sample described in chapter 2 provides a good trade-off between the degree of freedom and sufficient immobilization in an aqueous environment. The exponents possess a fraction of  $T_{On} < 1$  ms and  $T_{On} < 10$  ms, from which one can obtain an average on-time. This is achieved, by calculating the intensity average lifetime, allowing analysis of multi-exponential behavior in a collection of different excited-state populations [63]

$$\langle \tau \rangle = \frac{\sum_i A_i \cdot \tau_i^2}{\sum_i A_i \cdot \tau_i}, \quad (3.1)$$

where  $A$  are the amplitudes and  $\tau$  the exponents of the bi-exponential fit. Being in the order of a few milliseconds the on-times are significantly shorter than on-times of

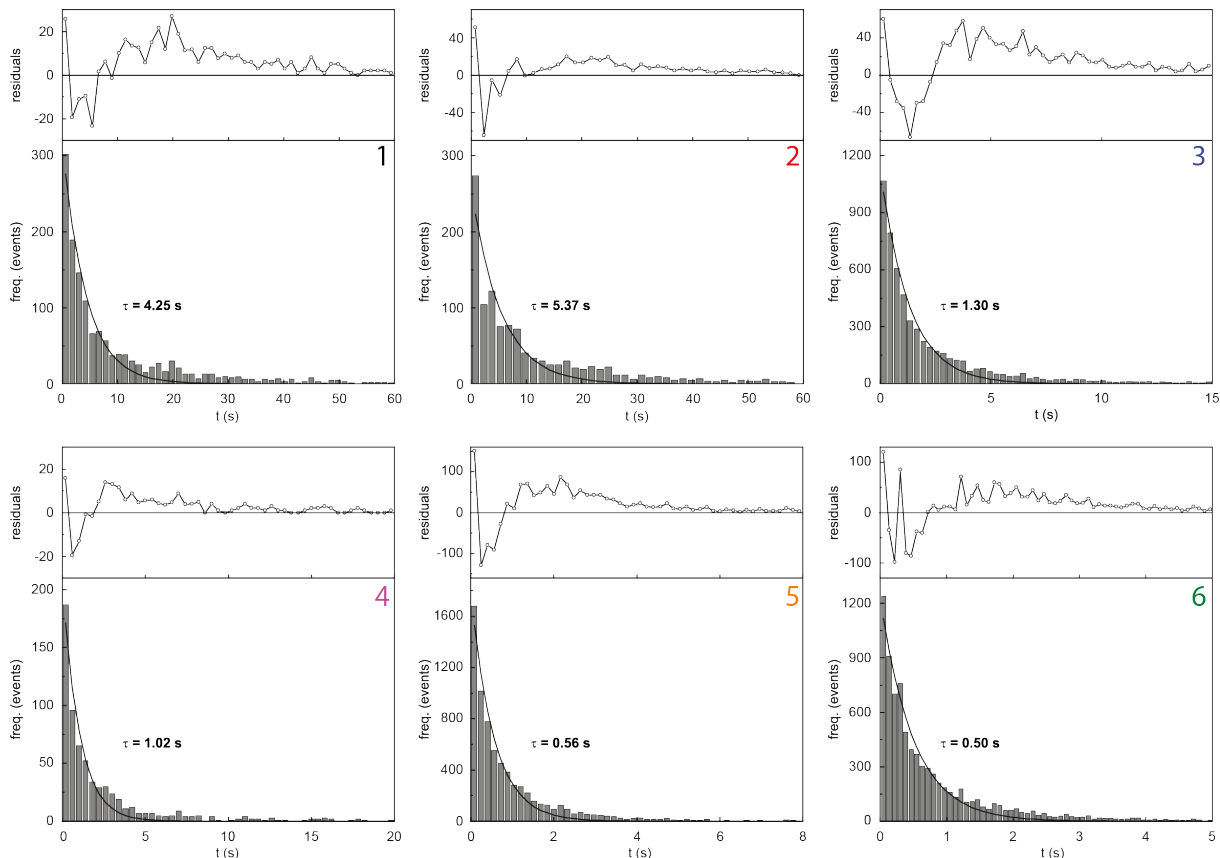


Figure 3.4: **Duration distribution of the off-events for the six compounds.** The histograms show the distribution of the off-times for each compound measured in wide-field single molecule microscopy. By fitting the distribution with a mono-exponential function (residuals on top) one can obtain  $T_{off}$  of the particular compound.

fluorophores used in STORM microscopy, reported in previous work [21]. Furthermore, they are also shorter than typical localization times used in MINFLUX nanoscopy nowadays [8, 9]. However, as MINFLUX needs substantially less photons compared to purely stochastic methods, it has been possible to image with these dyes, as will be shown in section 3.2.3. As the off-times are expected to be substantially longer, it was decided to obtain this parameter by wide-field measurements in similar conditions ensuring statistical significance of the data. The histogram of each evaluated fluorescent probe is shown in figure 3.4. The distributions are fitted with a mono-exponential function, as small fluctuations of the off-duration, addressed to the micro-environment, don't carry much weight. The off-times are in the order off several hundreds of microseconds up to a few seconds, surpassing the on-times by 2-3 orders of magnitude. As shown by the approximation in section 1.1.2, this is desirable, as it ensures a high probability of only one event in a diffracted limited spot (in dependence on the density of labeling).

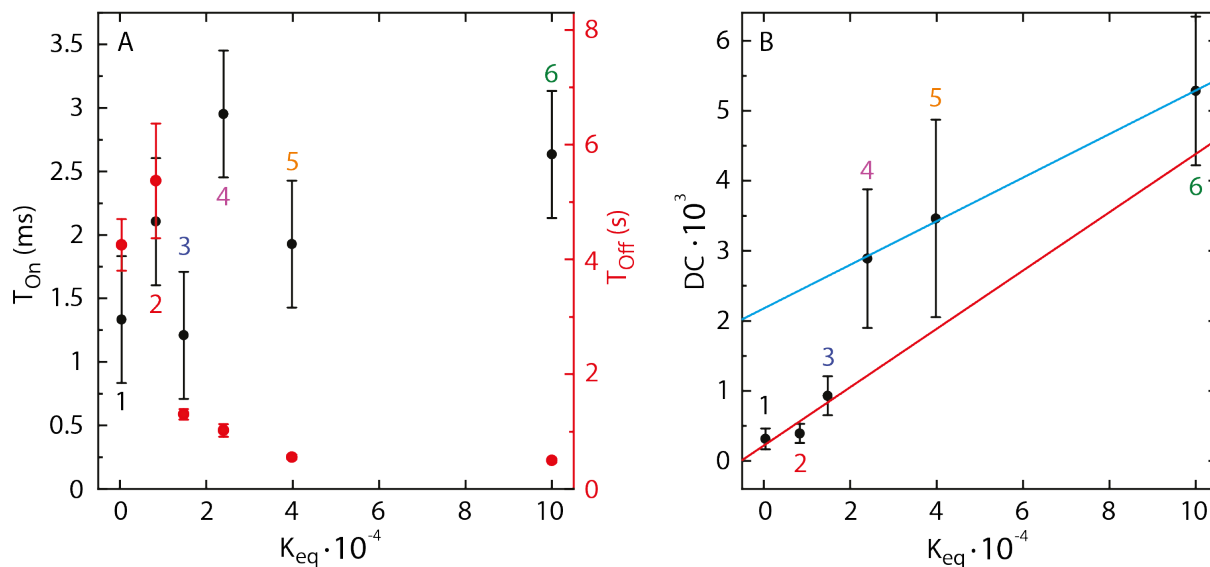


Figure 3.5: **On- and off-times of the six compounds and the corresponding duty cycle in dependence on the equilibrium constant.** A) The on-times (black) and off-times (red) in dependence on the equilibrium constant. While for the on-times no clear tendency can be demonstrated, the off-times show a strong decrease with an increasing constant, indicating a higher rate of on-events with rising pKa-value. Duty cycles for the two evaluated classes, varying in their substituents, display a linear behavior (B).

With the aid of equation 1.7 one can obtain the duty cycle of the evaluated compounds. Both the on-/off-times and duty cycle are plotted in dependence on the equilibrium constant of the two states in figure 3.5. While one cannot conclude there is a correlation of the equilibrium constant on the on-times (3.5A, black dots), a decrease of the off-times with rising pKa-value of the corresponding compound is clearly visible (3.5A, red dots). This leads to higher duty cycles of the respective compound (3.5B). For the two groups of stochastic blinking dyes, studied in this thesis, linear correlation fits the behavior of the duty cycle. Table 3.1 shows the photophysical properties of the six spontaneous blinkers studied in detail in this thesis. The percentage of bleaching is an estimation comparing the observed number of cycles  $N_{Cy}$  with the number of blinking events a dye with the respective off-time is expected to do in the measurement time (100 s). With increasing  $T_{Off}$  the photo-bleaching decreases, indicating a efficient shelving without absorption of excitation light in the off-state and no additional background consequently. The rate was calculated by the quotient of the Photon per event ( $Ph_{Cy}$ ) and the evaluated on-time ( $T_{On}$ ). The observed events show a similar rate for all compounds being in the regime of 100 KHz. This was expected, as these dyes all contain the same silicon-rhodamine (SiR) core and thus the chromophores are the same.

Table 3.1: Photophysical properties of the fluorescent probes

Comp.	$\Phi_{Fluo}$	pKa <sub>2</sub>	K <sub>eq</sub>	DC · 1000	T <sub>On</sub> (ms)	T <sub>Off</sub> (s)	N <sub>Cy</sub>	%Bl	Ph <sub>Cy</sub>	Rate (kHz)
<b>1</b>	0.1	2.62	417	0.31	1.3	4.25	13	45	143	111
<b>2</b>	0.17	3.92	8318	0.39	2.1	5.37	7	62	251	120
<b>3</b>	0.24	4.17	14791	0.93	1.2	1.3	36	53	115	96
<b>4</b>	0.16	4.38	23988	2.89	3.0	1.02	14	86	354	118
<b>5</b>	0.17	4.6	39811	3.46	1.9	0.56	39	78	207	109
<b>6</b>	0.16	5	100000	5.28	2.6	0.5	58	71	278	107

K<sub>eq</sub> = (K<sub>a2</sub>)<sup>-1</sup>; T<sub>On</sub> (average time, from bi-exponential fits); T<sub>Off</sub> (from mono-exponential fits);  
 DC = T<sub>On</sub> · (T<sub>On</sub> + T<sub>Off</sub>)<sup>-1</sup>, N<sub>Cy</sub>: cycles measured in 100 s (WF), % Bl = 100 · (N<sub>Cy</sub>/N<sub>Cy</sub><sup>Th</sup>);  
 Ph<sub>Cy</sub> (Confocal); rate = Ph<sub>Cy</sub> / T<sub>On</sub> (Confocal).

While MINFLUX, as a single molecule localization method, allows fast localizations of single fluorescent probes, in published work the localization process took up to a few hundred milliseconds [8, 9]. Therefore, further photophysical characterization of compound 4 was performed, as it possesses the largest T<sub>On</sub> = 3.0 ms and the highest Ph<sub>Cy</sub>. All of the investigated compounds change their structure in the spirocyclation process, which makes environmental sensitivity likely [64]. Hence, a characterization of compound 4 with different labeling strategies was required. Table 3.2 shows the photophysical properties of compound 4 labeled with three different bioconjugates (antibodies, nanobodies and HaloTag self-labeling enzyme), used for imaging in this work. To reduce precipitation, the compound was functionalized with a standard hydrophilizer (dipeptide linker) for labeling the nanobodies. The dependence on the tags appears to be clear, as the HaloTag bound compound shows a duty cycle an order of magnitude lower (mainly caused by the off-time), compared to the other candidates. This confirms the prediction of the micro-environment dependency. The average on-times are obtained as described above

Table 3.2: Photophysical properties of compound 4 bound to different ligands

Compound	DC · 1000	T <sub>On</sub> (ms)	T <sub>Off</sub> (s)	N <sub>Cy</sub>	%Bl	Ph <sub>Cy</sub>	Rate (kHz)
<b>Antibody</b>	2.89	3.0	1.02	14	86	354	118
<b>Halotag</b>	0.18	1.6	8.95	6.1	45	175	109
<b>Nanobody</b>	2.15	2.5	1.16	6.1	86	184	73

by bi-exponential fitting. While this is a good method to calculate a characterizing parameter, allowing a comparison between different compounds and linker, reducing the whole distribution to one number does not fully visualize the heterogeneity of the phenomenon. Thus, a model-independent analysis by plotting the experimental complementary cumulative distribution function (eCCDF) on T<sub>On</sub> was performed (see figure 3.6). The cumulative distributions show a significant portion of the fluorophore in a long on-state state above 6 ms (a typical time frame for a full MINFLUX iteration), while around 90% of the events are shorter than roughly 10 ms. Small differences in the distributions confirm the values, obtained by bi-exponential fitting.

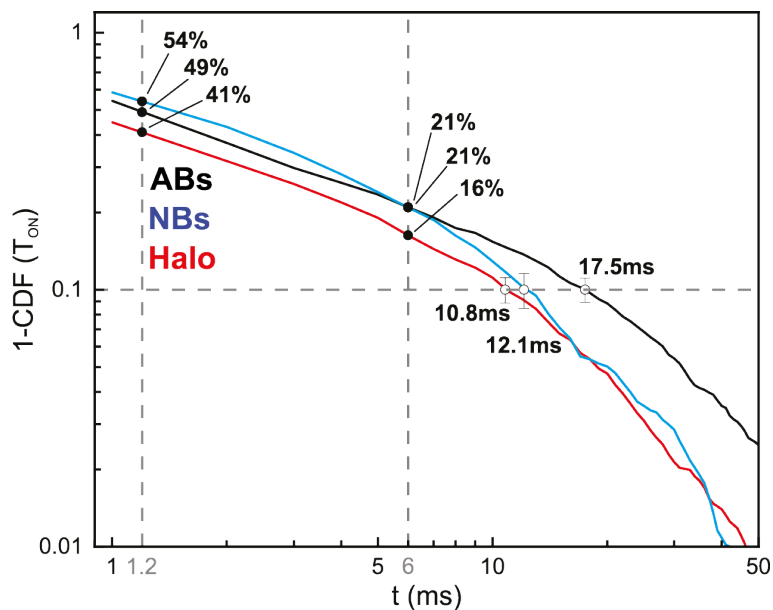


Figure 3.6: **Experimental complementary cumulative distribution function of compound 4 with different bioconjugates.** The distributions depict a moderate decrease in dependence on  $T_{On}$ , leaving a significant portion of events in a long on-time regime. A typical MINFLUX iteration takes between 4 – 6 ms. A gain of  $\approx 250\%$  on localized event (i.e.  $T_{On} > T_{Loc}$ ) is expected if the localization routine is decreased from 6 ms to 1.2 ms.

### 3.2.2 STORM Imaging

Since STORM is a rather simple super-resolution technique, allowing a high throughput of different samples and parameters (e.g. excitation power, labeling concentrations etc.), it is well-suited for preliminary screening of the compounds in biological relevant samples and for optimization of labeling conditions. Despite this, STORM and MINFLUX share a key requirement for fluorescent probes, by the utilization of distinguishable states of the fluorophores.

For the ease of labeling, in first samples antibodies with a high DOL of the respective compound were utilized to specifically tag the structures of interest. In figure 3.7 reconstructed STORM images of the bioconjugates are depicted, in which tubulin was labeled via a primary and a secondary antibody (the last one carrying the dye of interest). Secondary antibodies labeled with all six compounds are specifically binding, as only few background events can be seen and the tubulin structure is clearly displayed. Furthermore, despite their short on-times in the low millisecond regime (compared to typical frame times of 10 – 30 ms), the dyes emit enough photons for STORM measurements.

In section 3.2.1 the strong dominance of the non-fluorescent, closed form (duty cycle) was discussed. The expected opportunity of live-cell labeling with a HaloTag linker, caused

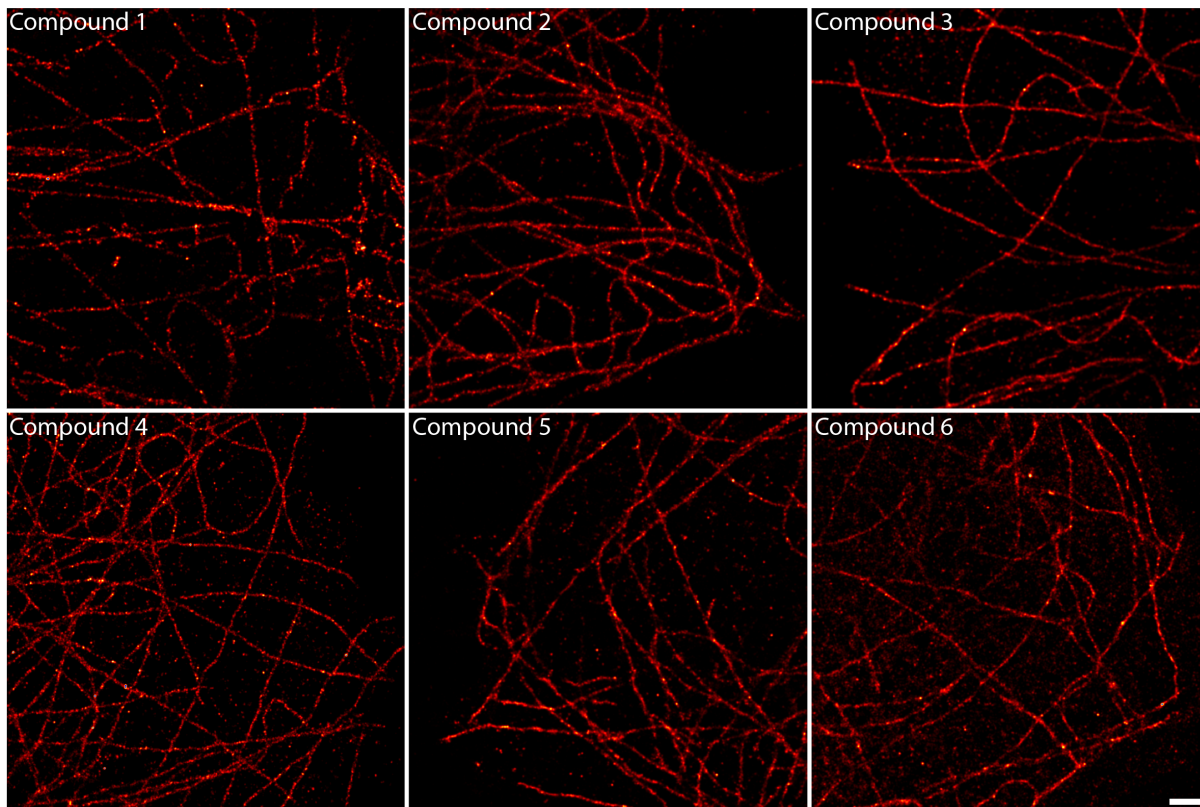


Figure 3.7: **Reconstructed STORM images of fixed tubulin.** The fixed cells (COS-7) are stained with a primary antibody (anti-tubulin) and a secondary antibody labeled with compound 1-6. The images prove a high specific binding. The localization precision of the single events is 20 – 25 nm. Scale bar: 1  $\mu$ m.

by the predominance of the neutral form, is confirmed by live-cell imaging of vimentin depicted in figure 3.8 for compound 3-6. Live-cell imaging with compound 1-2 failed, probably due to the extreme low duty cycle (see table 3.1). Compared with compound 4, the duty cycle appears to be lower by a factor of 10 resulting in a tenfold increase of the measurement time. As live-cells show movement in the micrometer regime in a timespan of a few minutes, super-resolution by SMLM was prohibited.

Both tubulin and vimentin are structures with a high density of binding sites allowing a high DOL and thus are widely spread as a sample to check staining of new dyes in general. However, the structures are labeled with an uncountable number of fluorophores, which makes quantitative analysis more difficult. As a biological relevant standardized system one can pick nuclear pore complexes (NPC), because they have a assignable number of binding sides [52]. As a consequence, MINFLUX images in section 3.2.3 were acquired on NPCs after testing them with a conventional SMLM first. Figure 3.9 exhibits the labeling integrity of the characteristic ring-like structure, labeled with nanobodies and HaloTag respectively in fixed and live-cell conditions.

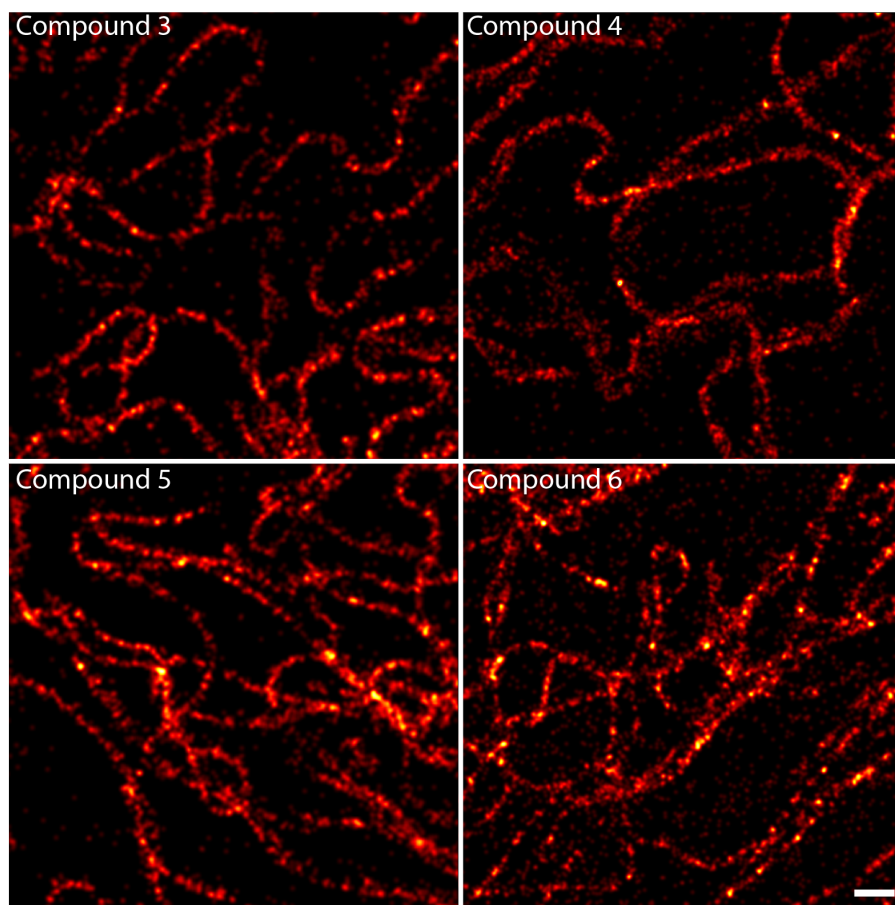


Figure 3.8: **Reconstructed STORM images of live-cell vimentin.** The cells (U2OS vimentin-halo) are labeled with chloralkane ligands (vimentin) of compounds 3-6. The specific binding of the vimentin filaments via HaloTag show the cell permeability of the dyes. The images were obtained under live-cell conditions with a localization precision of 20 – 25 nm. Scale bar: 500 nm.

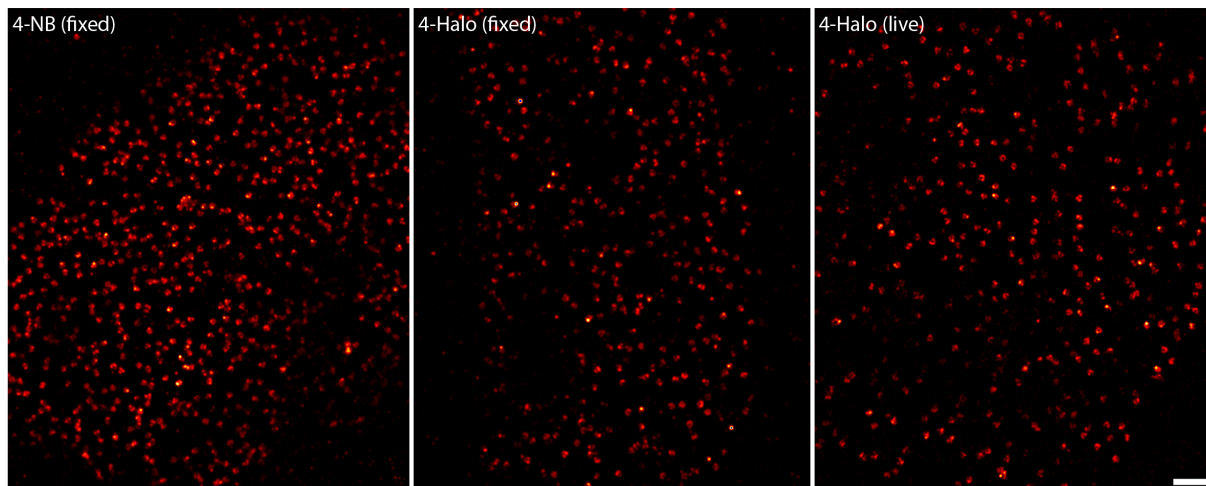


Figure 3.9: **Reconstructed STORM images of nuclear pore complexes.** The cells (mEGFP-Nup107, U2OS-Nup96-Halo) are labeled with either anti-GFP nanobody (fixed), or HaloTag (fixed before imaging, and live-cells imaging) of compound 4. Fixed samples were mounted in PBS, while live-cell samples were mounted in FluoBrite cell medium. The reconstructed images have a localization precision of 20 nm. Scale bar: 1  $\mu$ m.

### 3.2.3 MINFLUX Imaging of nuclear pore complexes

After showing the suitability of the spontaneously blinking dyes for biological samples in general with different linker in fixed and live-cell conditions, the consecutive step is to show their applicability in MINFLUX nanoscopy. As stated in the last section, NPCs suit well as a standardized biological system, wherefore mEGFP-Nup107 cells stained with nanobodies with compound 4 and U2OS-Nup96-Halo cells stained with compound 4 Halo ligand have been imaged. Both samples allow tagging with a smaller label compared to antibodies. Moreover, as the latter represents genetically engineered (CRISPR) cells, expressing the Halo protein at endogenous level, a single fluorescent probe per binding site is ensured.

First images were acquired with a standard imaging sequence by the manufacturer on a commercial MINFLUX setup. A detailed description of setup and sequences can be found in section 7.1. In brief, the localization process starts after the detected fluorescence signal surpasses an internal threshold. The following sequence can be split into two parts: The first one serves as a pre-localization containing 4 steps with decreasing  $L$  (1 ms each) and requires a minimum of 120 photons (above the background). The localization part of the sequence contains 2 steps (1 ms each,  $L_1 = 76$  nm and  $L_2 = 40$  nm, 30 photons

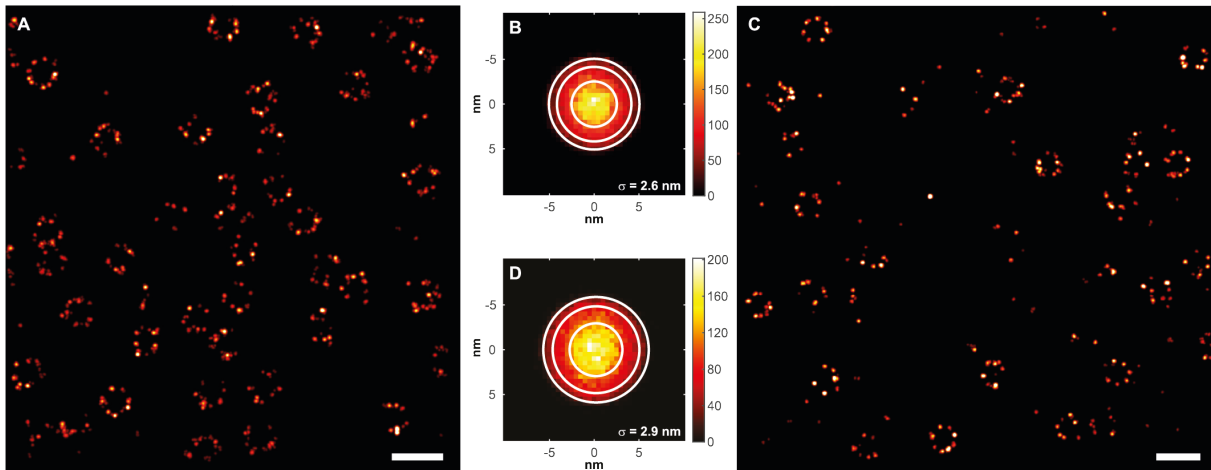


Figure 3.10: **MINFLUX images of nuclear pore complexes.** A) mEGFP-NUP107 cells labeled with an anti-GFP nanobody (compound 4, DOL=2). The corresponding 2D dispersion plot (B) shows a localization precision of  $\sigma = 2.6$  nm. C) U2OS-Nup96-Halo fixed cells labeled with compound 4 linked to HaloTag imaged with a localization precision of  $\sigma = 2.9$  nm (D). The events are plotted as Gaussians with the size of the average localization precision after filtering (see section 2.2.2). Scale bar: 200 nm.

per step), which are performed alternating until the fluorescence signal drops below the internal threshold. Thus, the recorded single emitter events consist of  $N$  localizations ( $N_{Loc}$ ), where  $N$  is the number of successful repeats of the last two steps. The localization precision of each event can be obtained from the distribution of the single localizations in respect to their mean position. Moreover, every single localization of the event has a time ID, as well as a distinct number of photons, adding up to a total localization time ( $T_{Loc}$ ) and a total number of photons ( $N_{Ph}$ ).

Figure 3.10 depicts MINFLUX images of NPCs labeled with the respective bioconjugates. The data was treated as described in section 2.2.2, filtering below a frequency (effective frequency offset,  $efo$ ) of 35 kHz to minimize background and filtering events with an inside-outside ratio (cfr) of collected photons excelling the range of  $-0.5 - 0.8$ . Further analysis showed a localization precision of  $\sigma = 2.6$  nm and  $\sigma = 2.9$  nm achieved with 185 and 163 photons/localization allocated mainly in the pre-localization process. This resulted in a localization time  $T_{Loc} = 52 - 70$  ms and  $T_{Loc} = 91 - 98$  ms respectively, depending on the statistical approach. An overview of the image parameters, obtained from further analysis, can be found in table 3.3.

However, as the dye has to be in the on-state for the duration of the localization process, a comparison of  $T_{Loc}$  with  $T_{On}$  (see table 3.2) shows that imaging was done in an extreme regime of  $T_{On}$ . Moreover, figure 3.6 underpins this, as only 1% of dyes measured in a single molecule environment showed on-times above 40 ms. As a result, the MINFLUX sequence was optimized, relating to the localization speed.

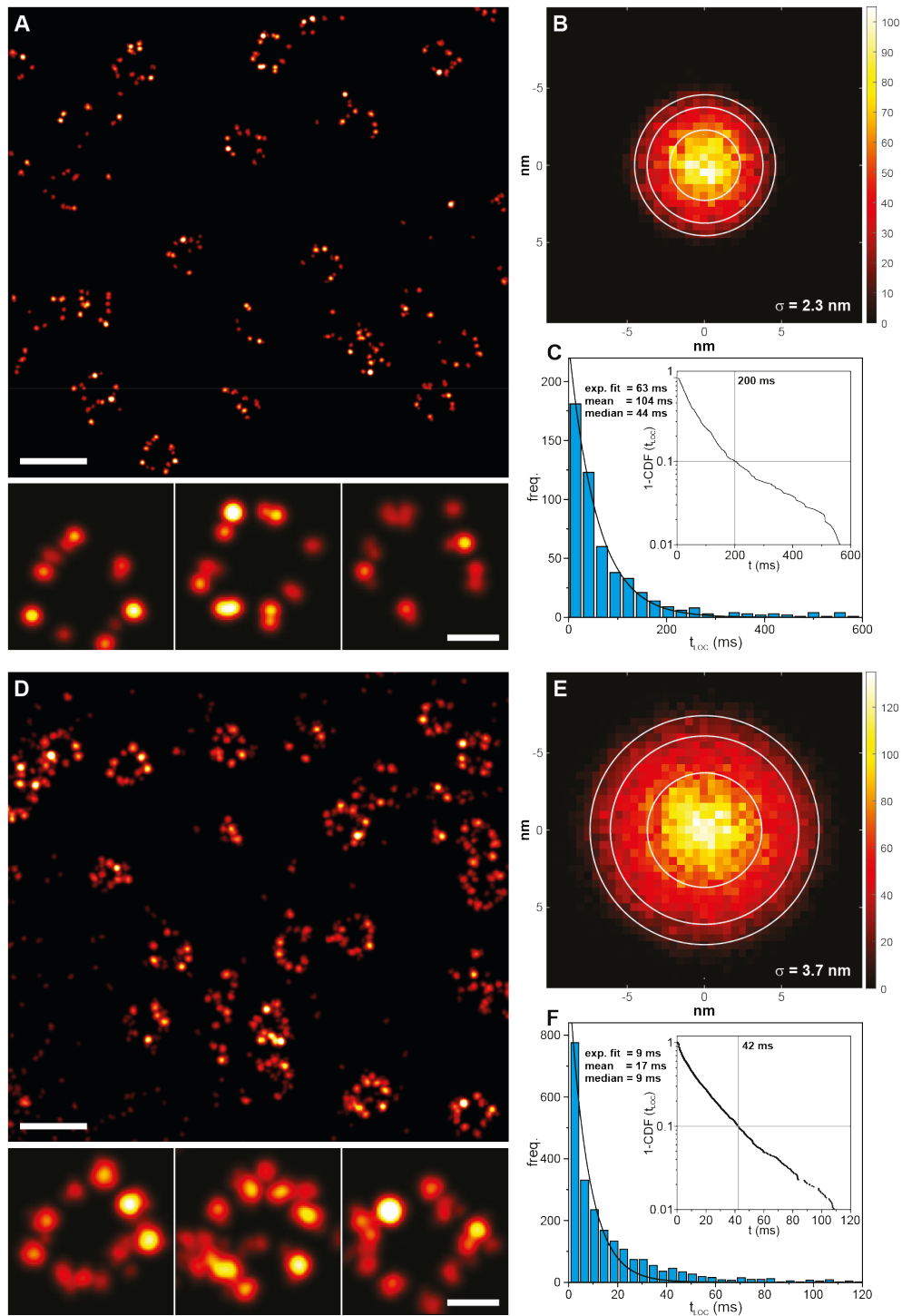


Figure 3.11: **mEGFP-Nup107 cells imaged with different MINFLUX sequences.** The cells were labeled with an anti-GFP nanobody (compound 4, DOL= 2). A) An image obtained with the conventional sequence taking 6 ms/iteration is compared with one taking 1.2 ms per localization (D). A panel with selected individual NPCs is showcased below. In B) and E) dispersion plots display distances between localizations and their respective cluster mean. Circles indicate  $\sigma$ ,  $1.64\sigma$  and  $2\sigma$ . The histograms C) and F) depict the distribution of  $T_{Loc} = t_{last} - t_{first}$ . The highlighted values correspond to 90% of the measured events. Scale bar: A)D): 200 nm; B)E): 50 nm.

Since in previous measurements (see table 3.3) the lion’s share of photons was utilized in the pre-localization, the number of steps and the dwell time of each step was reduced to 2 steps with 0.7 ms in total, in which  $L$  was halved subsequently. The localization part was reduced to one final step at  $L = 76$  nm with a shortened dwell time of 0.5 ms. Excitation power was doubled ( $P = 540 \mu\text{W}$  at microscope entry) compared to previous measurements, addressing the reduced dwell times. The sequence can be found in detail in the supplements 7.1. As the conventional sequence uses a localization step with  $L = 40$  nm a trade off between localization time and localization precision is expected. Figure 3.11 displays images of mEGFP-NUP107 cells, labeled with nanobodies of compound 4, comparing the conventional sequence (A) and the adapted sequence (D). While the localization precision declined from  $\sigma = 2.3$  nm to  $\sigma = 3.7$  nm (B,E), localization speed increases. Median and exponentially fitted  $T_{Loc}$  decrease from 44 – 63 ms to 9 ms. Table 3.3 lists all parameters evaluated in figure 3.11. Whereas the number of localizations does not vary significantly, the number of photons exploited decreases by a factor of 5 resulting in the localization time reduced by a factor of 5-7, mainly due to the pre-localization steps.

### 3.3 Discussion

Since stochastic imaging approaches are bound to a high number of photons (and hence a large  $T_{On}$  to localize emitters) previous studies of blinking fluorescent probes were mainly focused on photon output and duty circle [45]. The latter, as explained above, determines the density of labeling, which also plays a role in MINFLUX nanoscopy. However, as the photon demand by MINFLUX is significantly lower, resulting in a faster localization process, a more detailed study of the parameters (e.g.  $T_{On}$ ) is necessary. Such a study has been made for one other spontaneous blinker (HMSiR, [21]), calculating an average on-time of  $T_{On} = 96$  ms. A first proof of principle MINFLUX measurement with HMSiR was done in 2021, making use of the spontaneous blinking as distinguishable states and achieving a comparable localization precision of 2.3 nm [59]. However, a dye with such a long on-time does not make use of the high localization speed possible with MINFLUX nanoscopy [65]. Dyes, evaluated in this work, are optimized for such fast localizations in a single digit millisecond regime, showing on-times shorter by a factor of 30 compared to previous work.

No further analysis on the localization duration regarding spontaneously blinking dyes has been performed yet. Moreover, even for AlexaFluor647, a dye more established in MINFLUX nanoscopy, localization times were not evaluated, but thresholds were stated

[8, 9]. The cited studies focused on localization precision, making use of 2100/2000 (excluding pre-localization) in 4/5 localizations with at least 260/200 ms per event, detecting at a average rate of 30/50 kHz. Due to accessibility of the data and the similarity of the used commercial MINFLUX setups, evaluation with routines used in this work and a subsequent comparison of data from [9] with the data of this thesis was possible. As photon numbers diverge significantly for the different measurements, data binning of figure 3.10A was executed to compare localization precision (figure 3.12). Evaluating both data set at chunks of 350 photons, shows a localization precision of  $\sigma = 1.9$  nm and  $\sigma = 2.2$  nm [9] respectively, while data presented in this work was roughly 25% faster acquired, due to the higher photon rate (see table 3.3). Binning up to 700 photons and filtering results in a precision below 1 nm on the one hand, but is accompanied by a large loss of usable events on the other hand. Comparing the localization time  $T_{Loc}$  gained in these two experiments, exposes an acceleration of the localization process by a factor of 17/32 per fluorescent event. This yields a trade of in localization precision by a factor 1.7/4 depending on the data binning used in [9].

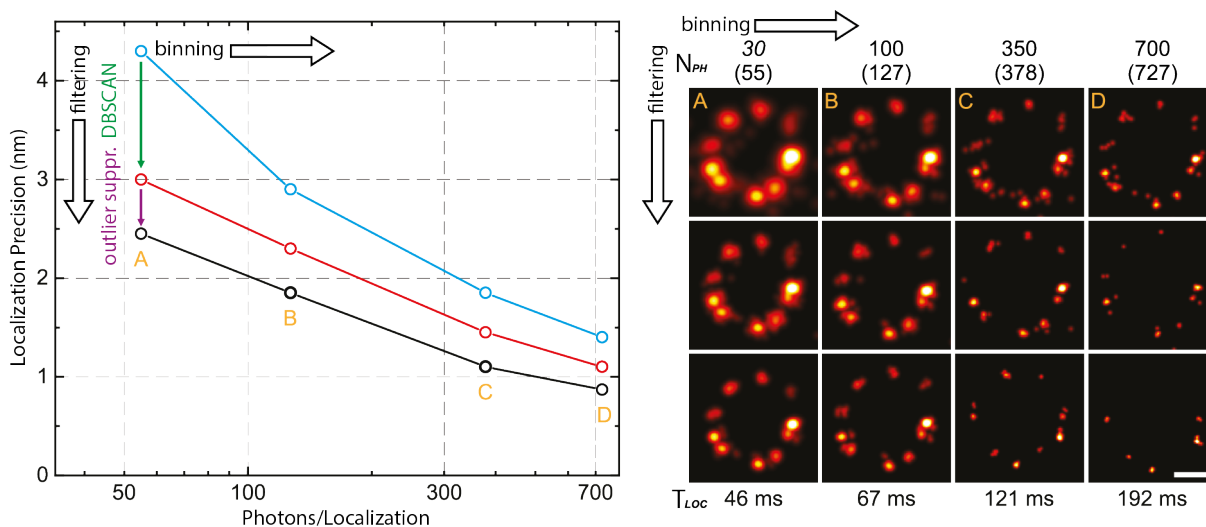


Figure 3.12: **Localization precision in dependence on binning and filtering.** Data from figure 3.10A is reevaluated for different bins of photons and with/without the filtering methods used in this thesis. A localization precision below 2 nm can be achieved by moderate binning and minor loss of events. For visualization purposes an individual NPC is shown on the right panel with the respective parameters. Scale bar: 50 nm.

The results presented in this chapter underline the importance of stochastic blinking dyes for MINFLUX. Whereas first MINFLUX measurements were mostly done with AlexaFluor647, inducing blinking by UV activation and excitation under the influence of special blinking buffers, the spontaneous blinking approach uncouples the blinking behavior from any excitation or activation and blinking buffer environment. Specifically,

Table 3.3: Image parameters obtained from the MINFLUX measurements compared with Schmidt et al. ([9])

	$\sigma$ (nm)	$N_{Loc}$ median/exp	$N_{Ph}$ median	$T_{Loc}$ (ms) median/exp	$Ph_{Preloc}$ median	$Ph_{Loc}$ median	Rate (kHz)
<b>NB A</b>	2.6	7/10	1300	52/70	1000	51	57
<b>HT B</b>	2.9	8/7	1300	91/98	920	48	45
<b>Fast Seq A</b>	2.3	7/9.4	2200	44/63.4	1800	71	76
<b>Slow Seq D</b>	3.7	6/7.5	450	9/8.6	100	55	118
<b>Schmidt et al.</b>	2.2 <sup>1</sup> /1.35	5/3.9	2230	155 <sup>3</sup>	1000	415	30
<b>(Figure 3d, [9])</b>	0.9 <sup>1</sup> /0.8	3 <sup>2</sup>	6600	323 <sup>3</sup>	920	2173	30

<sup>1</sup> precision reported in [9]; <sup>2</sup> no exponential fit; <sup>3</sup> exponential fitting failed due to the distribution of the events

the fluorophores, proposed and characterized in the underlying work, are optimized for fast localizations, enabled and utilized by MINFLUX nanoscopy. Due to multi-exponential behavior of the on-times, it was possible to image in a, until now, conventional MINFLUX localization regime, as well as speeding up localizations by a factor of 5-7 for the very same sample and up to 30 times, compared with previous publications [8, 9], enabling a broad spectrum of different experiments and applications.

# Chapter 4

## Irreversible On-Switching Dyes

This chapter contains the studies of photoactivatable xanthone dyes (PAX [34]). This group of fluorophores perform irreversible photo-induced switching into the fluorescent on-state, in a cage-group free manner.

The chapter begins with a brief introduction setting the approach of irreversible switching fluorophores into the context of super-resolution microscopy, (section 4.1).

A comprehensive study in a single molecule environment was designed and realized (section 4.2.1), evaluating characteristics of the fluorophores important for MINFLUX nanoscopy.

The suitability for biologically relevant samples is shown in section 4.2.2, by staining several different structures in both fixed and live-cells. Moreover, by combining different labeling strategies (nanobodies and HaloTag), multicolor PALM imaging with different PAX derivatives was performed.

Finally, the suitability as fluorescent probes for MINFLUX nanoscopy was demonstrated by imaging U2OS Nup96-halo and HeLa HK-2xZFN-mEGFP-Nup107 cells achieving a similar localization performance to established red-emitting fluorophores (see section 4.2.3).

Furthermore, functioning as a standardized sample in nanoscopy in terms of size and number of fluorophore binding sites (see Thevathasan et al. [52]), the NPC system allowed analytic comparison for PALM and MINFLUX data in terms of apparent density of labeling for both imaging techniques. Moreover, imaging with genetically modified U2OS-CRISPR-Nup96-mMaple was performed allowing a comparison of the fluorescent probes with fluorescent protein labeling on an endogenous level (see section 4.2.4).

The chapter concludes in a discussion of the results obtained in the underlying thesis (section 4.3).

The study presented in this chapter resulted in publications by Lincoln et al. [34] and Rimmel et al. (in preparation). This dye group was discovered and synthesized by Richard Lincoln (Ph.D, Optical Nanoscopy, MPIImR, Heidelberg). Analysis of the data was performed in exchange with Mariano Bossi (Ph.D, Optical Nanoscopy, MPIImR, Heidelberg).

## 4.1 Introduction and Aim

Photoactivatable dyes are a specific group of irreversible on-switching dyes absorbing light to uncage from an initial fluorescent off-state. This is accomplished via the transition in the excited state yielding a fluorescent molecule (see section 1.1.3), which can be excited and detected subsequently. In contrast to stochastic reversible switching dyes, discussed and evaluated in chapter 3, photoactivatable probes possess a single cycle, allowing a number of localizations before they switch off permanently by photo-bleaching.

As MINFLUX nanoscopy represents one of the latest advances in optical nanoscopy [7], only few reports of mechanisms other than photo-induced blinking (e.g. cyanines such as AlexaFluor647) have been presented [7, 9, 66]. However, recent studies either propose photoactivatable fluorescent probes [67], or show the applicability for MINFLUX nanoscopy utilizing different caging approaches [8, 34, 68, 69].

In coordinate stochastic super-resolution microscopy, like PALM, the number of detectable photons is of utmost importance, which made brightness and photo-stability the parameters of choice for dye selection. In MINFLUX nanoscopy, however, maximizing photon numbers isn't the main concern, as significant fewer photons are sufficient for the same localization precision (see figure 1.8). This leaves space for other dye parameters more important to MINFLUX, namely the photoactivation mechanism itself: Initially, PALM and MINFLUX require uncaging of only one fluorophore in a diffracted limited spot. However, the focused excitation beam functioning as reference coordinate in MINFLUX evokes high intensities in proximity of the to be localized molecule. Thus, uncoupling the excitation from the activation process is strongly preferred to ensure the discrimination. This interest appears clearly, as photoactivatable dyes possess a single fluorescent on-cycle only. Hence, maximizing the number of successful localizations (the detection ratio) is one center point

in the research of irreversible on-switching dyes, as failed localizations affect the apparent density of labeling dramatically and can only be equated by increasing the number of labels (see section 1.3). Nevertheless, a single cycle bears the advantage of prohibiting multiple redundant localizations of the same label. Moreover, it significantly eases the quantitative analysis of the data.

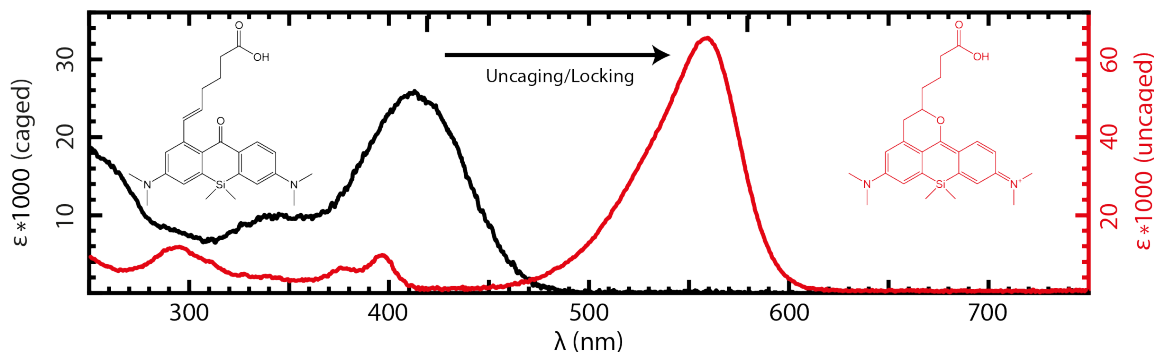


Figure 4.1: **Absorption spectra of the open (non-fluorescent) and closed (fluorescent) form.** Irradiation of PAX<sub>560</sub> with UV light (black spectrum) results in uncaging/locking of the molecule absorbing at  $\lambda = 560$  nm (red spectrum).

In context of this thesis a series of photoactivatable dyes were investigated. In contrast to previous published fluorescent probes, their activation mechanism relies on photo-induced locking of the fluorophore structure (cage-group free uncaging), instead of unlocking by degradation of photolabile groups via UV illumination [34]. Figure 4.1 depicts an exemplary fluorophore structure (PAX<sub>560</sub>) visualizing the fluorescent and non-fluorescent forms with their respective absorption spectra. On the one hand, this approach is expected to provide reliable uncaging, as their mechanism is well defined with only a minor amount of side products possible. On the other hand, it keeps the size of fluorescent molecules small. The latter is important to keep the dye soluble and to facilitate cell permeability. In addition to demonstrating the applicability as dyes suitable for MINFLUX nanoscopy, including a characterization of the required parameters, the aim of these studies was to investigate the detection efficiency in MINFLUX nanoscopy as expressed in the apparent density of labeling, as well as resolving the fluorescent label itself.

## 4.2 Results

### 4.2.1 Photophysical Characterization

From the first color palette of PAX dyes five compounds (PAX<sub>480</sub>, PAX<sub>525</sub>, PAX<sub>560</sub>, PAX<sub>+560</sub>, PAX<sub>570</sub>) were investigated. The structures are depicted in the fluorescent (closed) form in figure 4.2, with their respective emission spectra. The commercially available MINFLUX microscope setup possesses a green ( $\lambda_{ex} = 560$  nm) and a red detection channel ( $\lambda_{ex} = 640$  nm) only, photophysical characterization was focused on PAX<sub>560</sub> and PAX<sub>+560</sub>, with respect to their applicability in MINFLUX nanoscopy.

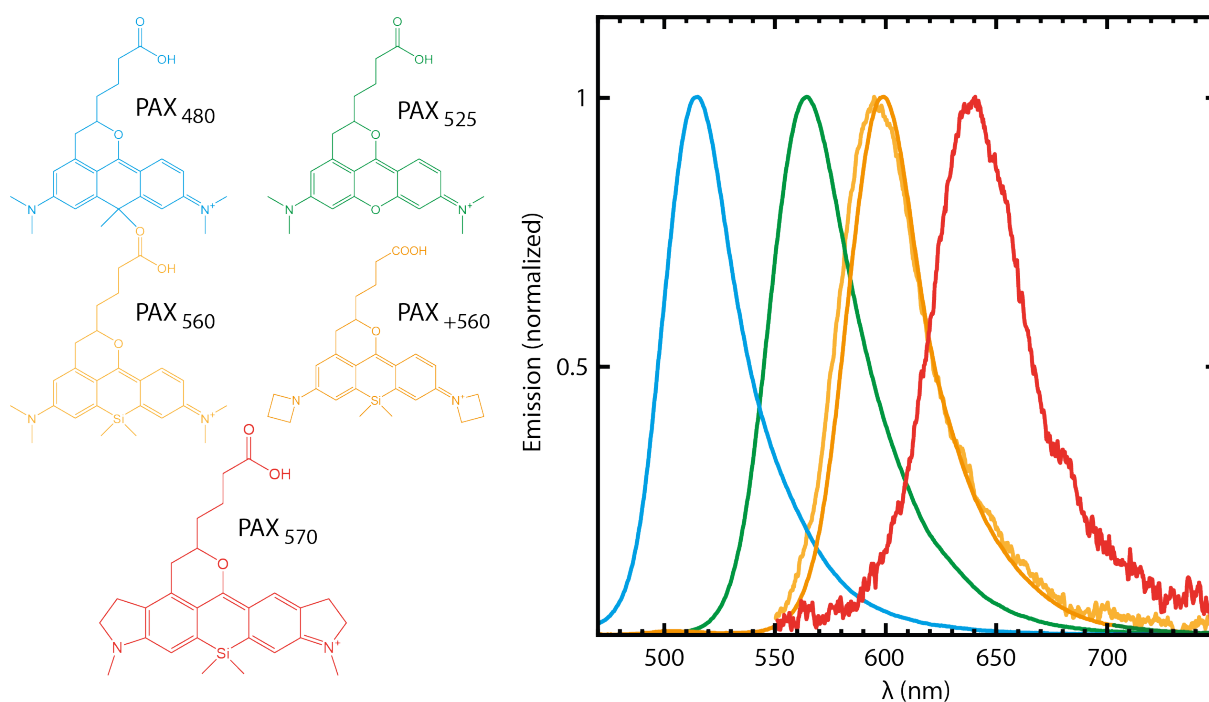


Figure 4.2: **PAX compounds utilized in this work.** The structures of the PAX compounds are shown on the left side with their respective normalized emission spectrum on the right.

As explained in section 1.1.3, photoactivatable fluorophores possess a single on-state after uncaging. Thus, for localizing the single probes successfully, three criteria must be given: Reliable uncaging provides a single fluorescent probe in a diffracted limited spot; a sufficient event duration is needed to localize with the microscope technique of choice; a sufficient number of photons determines the success of the localization and influences its precision. Thus, the photophysical characterization focused on those aspects.

For photophysical characterization, chloralkane ligands of PAX<sub>560</sub> and PAX<sub>+560</sub> (specific for HaloTag), which were used predominantly in imaging experiments, were sparsely distributed enabling a single molecule environment and mounted in a phosphate buffer

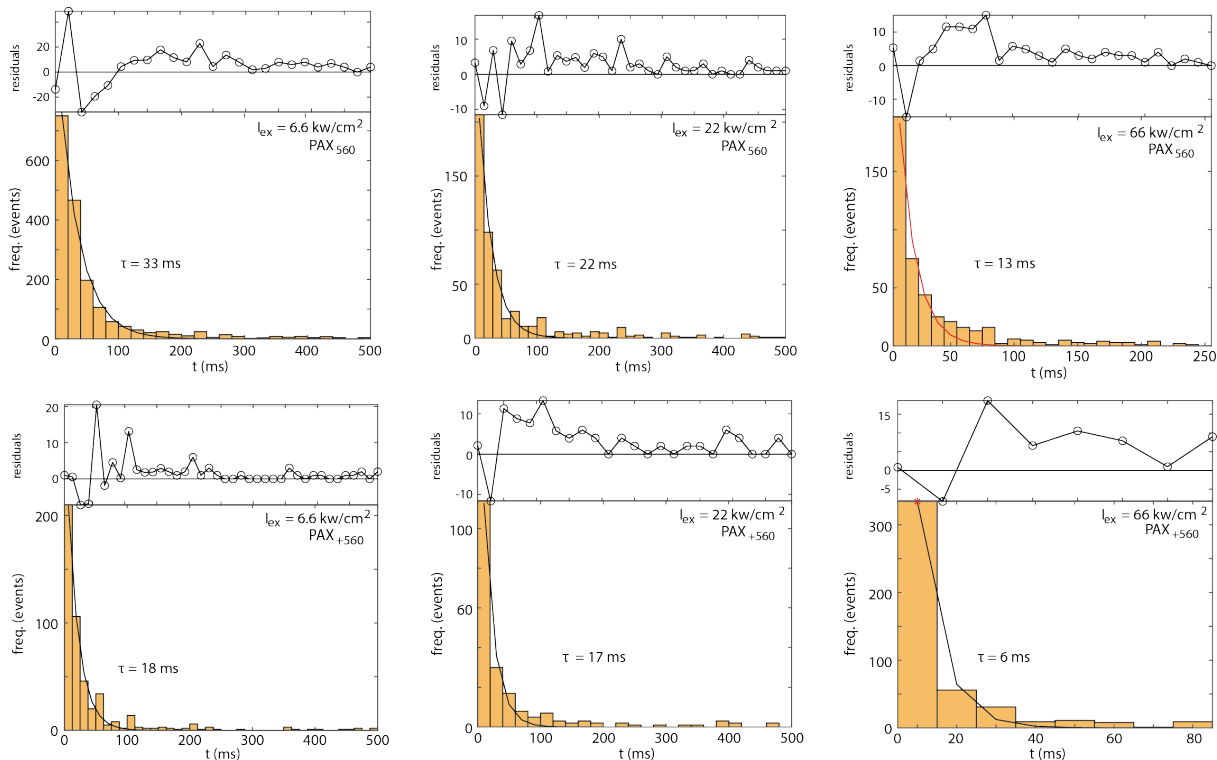


Figure 4.3: **Histograms of the event duration ( $T_{On}$ ) for  $PAX_{560}$  and  $PAX_{+560}$  at three different excitation intensities.** The histograms depict the distribution of the on-times for both compounds measured in wide-field microscopy at single molecule level. While screening the excitation intensity the UV activation light was set to  $P_{405nm} = 2.5 \text{ nW}$  measured at the back focal plane of the objective lens to ensure a reasonable number of events,. The distribution is fitted by a mono-exponential function (residuals on top). The on-time  $\tau_{+560,66kW/cm^2} = 8 \text{ ms}$  lies below the time resolution of the experiment. The samples were mounted in a phosphate buffer system (PBS, pH=7.4).

system (PBS, pH=7.4) (see section 2.3.1). Data were acquired in a wide-field microscope exciting single molecules and detect the fluorescent light with an EMCCD camera taking a frame every 10 ms, as described more detailed in section 2.2.1. Moreover, the sample was activated with different doses of UV light simultaneously. Figure 4.3 depicts the time of the emission events measured with a resolution of 10 ms as histograms fitted with a mono-exponential function. The fits show on-times ( $T_{On} = k_{bl}^{-1}$ ) ranking between 10 – 33 ms. Increasing the excitation intensity results in a clear decrease of the event duration, ultimately below the time resolution of the experiment in case of  $PAX_{+560}$  at the highest excitation intensity. However, as localization times in MINFLUX nanoscopy can be in the low single digit millisecond regime and even shorter, the measured on-times for both compounds are sufficient at moderate excitation powers for more than  $N_{loc} = 10$  localizations [65].

Table 4.1: **Photophysical properties of the fluorescent probes**

	$\Phi_{fluo}$	Intensity (kW/cm <sup>2</sup> )	T <sub>On</sub> (ms)	Ph	Rate (kHz)
PAX <sub>560</sub>	0.48	6.6	33	3920	7.8
		22	22	2300	16.6
		66	13	2850	41.3
PAX <sub>+560</sub>	0.92	6.6	18	2410	7.2
		22	17	3590	19.4
		66	<10	1860	30.6

In table 4.1 the on-times are put in context of the other properties measured for both compounds in wide-field conditions (excitation power in the same order of magnitude as for MINFLUX) with a time resolution of  $t = 100$  ms. While an increase of the detection rate can be witnessed with increasing excitation power, no clear trend for the number of photons was observed. Remarkably, although the fluorescent quantum yield is strongly enhanced for the azetidine form (PAX<sub>+560</sub>), no increase of photons was observed. This could hint to diverging intersystem crossing rates into the triplet state of the respective fluorophores. However, in contrast to PAX<sub>560</sub>, PAX<sub>+560</sub> shows a strong decrease of photon number going hand in hand with the low event duration (figure 4.3), indicating significant photo-bleaching at higher excitation intensities. Such a trend is not observable for PAX<sub>560</sub>. Overall, the single dyes emit on average several thousand photons in a PBS buffer environment under single molecules conditions. Simulations of the localization precision in dependence of the number of photons (see figure 1.8), suggest the possibility of localizing with a single nanometer precision using MINFLUX nanoscopy at a moderate  $L = 100$  nm.

Figure 4.4 shows the activation rate in dependence on the activation power of the UV light ( $\lambda = 405$  nm) for the investigated compounds illuminated in single molecule conditions. The data were evaluated by fitting the time duration till uncaging occurred ( $t_{Act}$ ) by a mono-exponential (figure 4.4B). As experiments without UV activation yielded a significantly lower amount of events and no exponential behavior, these data sets were evaluated by calculating the median of  $t_{Act}$  (figure 4.4C). No significant activation could be witnessed without UV illumination and furthermore no tendency in dependence on excitation power ( $P_{ex}$ ) was observed. However, the fluorophores uncage in a highly efficient manner in the low nanowatts regime (figure 4.4A). Significant activation could be observed down to  $p_{405nm} = 2.5$  nW, measured at the backfocal plane of the microscope. Linear fitting of the two data sets yield a rate of  $k_{=Act,560} = 1/\tau = 0.13$ /nWs and  $k_{Act,+560} = 0.017$ /nWs respectively. In contrast to the 7-fold increase of activation for PAX<sub>560</sub> chloralkane ligand in single molecule conditions, a 3-fold increase could be observed in bulk experiments [34]. However, as the mechanism of photoactivation is expected to be dependent on the micro-

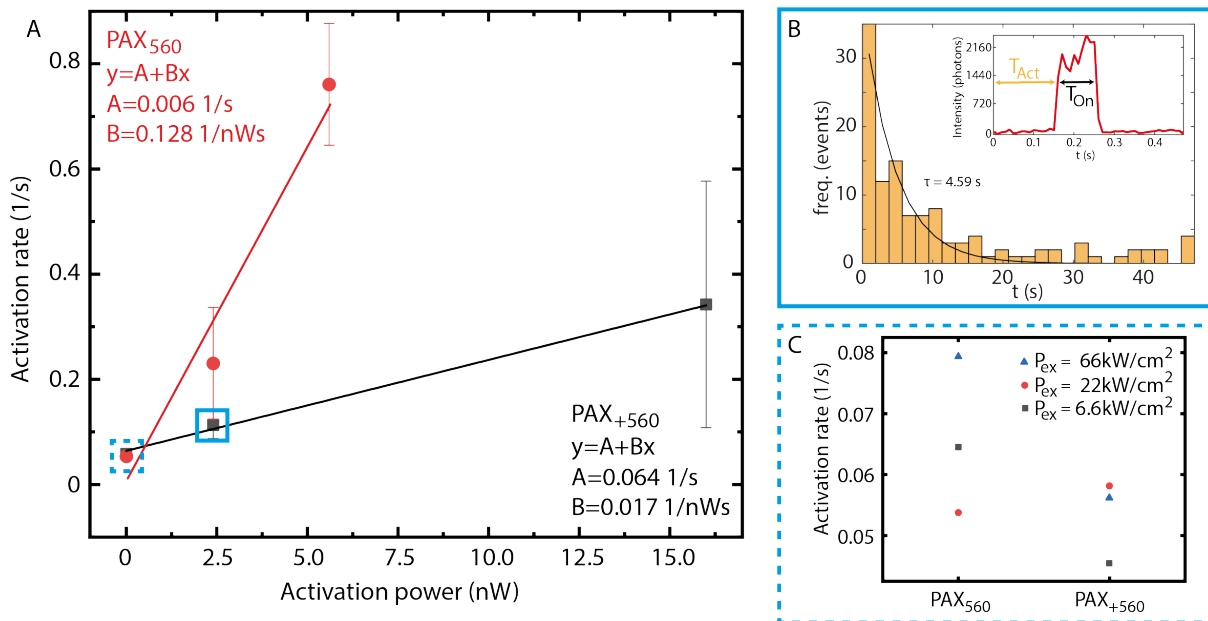


Figure 4.4: **Activation rate in dependence on activation power.** The plot depicts the activation rate of PAX<sub>560</sub> and PAX<sub>+560</sub> in dependence on the UV activation power ( $\lambda = 405$  nm) measured in sparsely labeled single molecule samples mounted in PBS (HaloTag ligand, see section 2.3.1 for more details). The fluorophores were excited at an intensity of 22 kW/cm<sup>2</sup> and show a linear dependence on the activation power ( $k_{Act,560} = 0.13$ /nWs,  $k_{Act,+560} = 0.017$ /nWs). Data were evaluated by fitting a mono-exponential function to  $t_{Act}$  (B), or by calculating its median (for  $P_{405nm} = 0$  nW). The inset shows a single photon trace visualizing  $T_{Act}$  and  $T_{On}$ . No significant uncaging and no trend related to the excitation power could be witnessed (C).

environment and especially faster in the case of the chloralkane ligand [34], deviations compared to the free compound are expected. In conclusion, the dye switches into the fluorescent on-state highly efficient by UV light-induced uncaging at minimal light doses, minimizing light induced damages in live-cells.

## 4.2.2 PALM Imaging

Since PALM is a rather simple super-resolution technique, allowing a high throughput of different samples and parameters (e.g. excitation power, labeling concentrations etc.), it is well-suited for first tests of the compounds in biological relevant environments enabling optimization of labeling conditions. Despite this, PALM and MINFLUX share a key requirement for fluorescent probes, by the utilization of distinguishable states of the fluorescent probes.

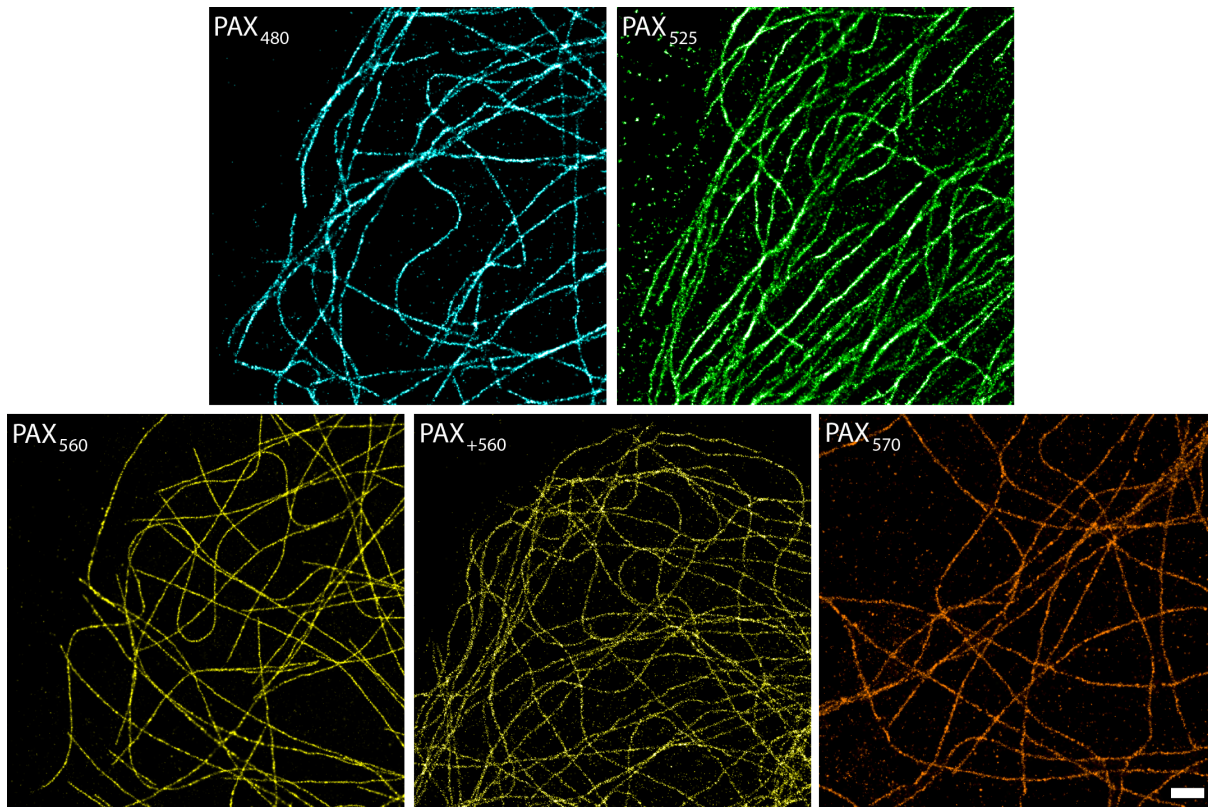


Figure 4.5: **Reconstructed PALM images of fixed tubulin.** The fixed cells (COS-7) were stained with a primary antibody (anti-tubulin) and a secondary antibody labeled with the respective compounds. The images show a high specificity of all prepared antibodies binding. The localization precision of the single events is 10 – 16 nm. Scale bar: 1  $\mu\text{m}$ .

Due to the ease of labeling, for the first samples, antibodies with a moderate DOL (2-4) of the respective compound were chosen to specifically tag the structures of interest. In figure 4.5 reconstructed PALM images of the bioconjugates are depicted, in which tubulin was labeled via primary and secondary antibodies (with the dye of interest labeled to the secondary antibody). All five compounds are specifically binding, as only few background events can be seen and the tubulin structure is clearly displayed. As the fluorescent probes are uncharged and of small structural size, live-cell labeling could be performed via chloralkane ligands of the respective compounds. Figure 4.6 depicts reconstructed PALM images acquired under live-cell conditions and proves the cell permeability of the fluorescent probes. The parameters of these data sets are listed in table 4.2. The localization precision of the obtained images is about  $\sigma \approx 10 - 15$  nm which was expected as several thousand photons were emitted in single molecule experiments as well as in PALM microscopy. Bulk studies on the respective compounds revealed a large difference of the activation quantum yield ( $\Phi_{act}$ ) by about a factor of 50 between PAX<sub>480</sub> and PAX<sub>560</sub> [34]. This also could be witnessed in PALM microscopy. Furthermore, PAX<sub>480</sub> showed essential uncaging at  $\lambda = 470$  nm excitation while imaging, prohibiting MINFLUX imaging with an uncoupled excitation-activation scheme. However, the difference in

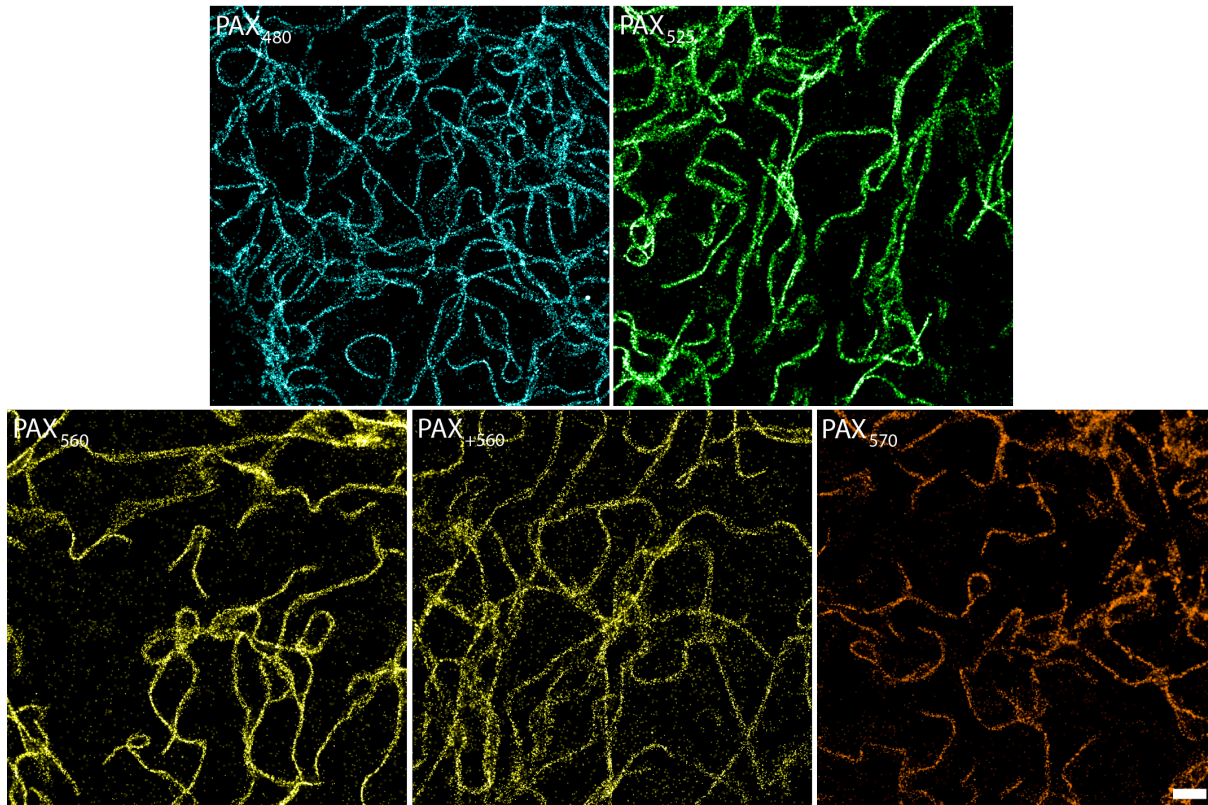


Figure 4.6: **Reconstructed PALM images of vimentin in live-cells.** The cells (U2OS vimentin-halo) were labeled with chloralkane ligands of the compounds. The specific binding of the vimentin filaments via HaloTag show the cell permeability of the dyes. The images were obtained under live-cell conditions with a localization precision of  $\sigma \approx 15$  nm. Scale bar: 1  $\mu$ m.

Table 4.2: **Image parameters obtained from the respective PALM measurements**

Compound	Tubulin (fix)		Vimentin (live)	
	Photons	$\sigma$ (nm)	Photons	$\sigma$ (nm)
Pax <sub>470</sub>	2315	16.0	4926	13.4
Pax <sub>525</sub>	3827	16.6	1950	15.8
Pax <sub>560</sub>	2822	13.8	4430	15.1
Pax <sub>+560</sub>	4540	8.2	3678	10.1
Pax <sub>570</sub>	1719	15.0	2053	16.2

activation quantum yield enabled sequential two-color imaging of the compounds, which is depicted for tubulin (PAX<sub>560</sub>) and clathrin-coated pits (PAX<sub>480</sub>) in figure 4.7. The structures were imaged sequentially. The first data set comprises the signal of PAX<sub>480</sub> exploiting its activation at  $\lambda = 470$  nm. Afterwards tubulin stained with PAX<sub>560</sub>-antibodies was imaged while activating the sample with weak pulses of UV light ( $\lambda = 405$  nm).

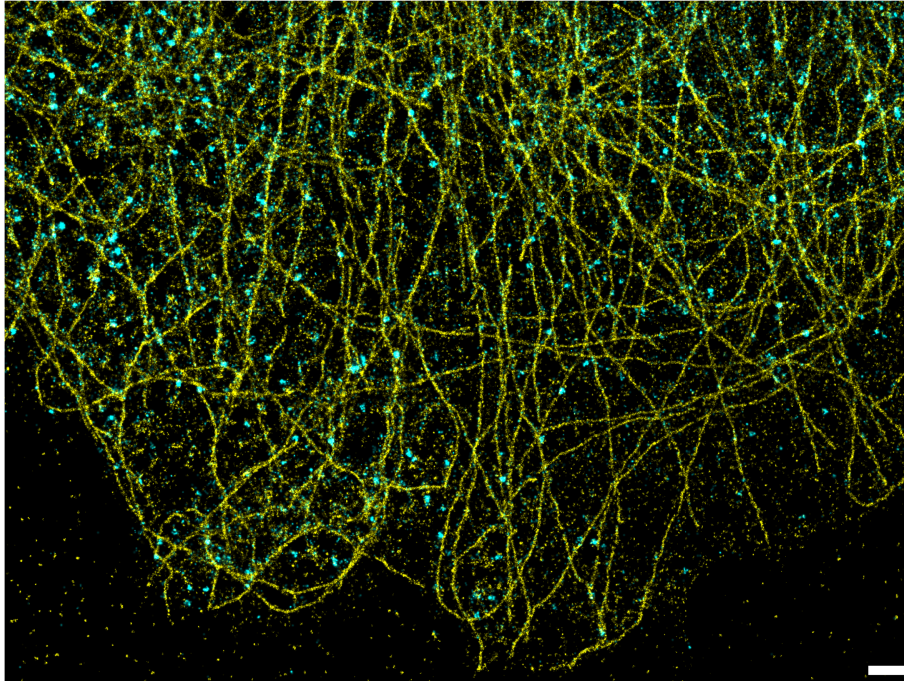


Figure 4.7: **Two-color PALM image of tubulin and clathrin-coated pits stained with PAX<sub>560</sub> and PAX<sub>480</sub>.** The reconstructed PALM image shows COS-7 cells labeled with primary antibodies (anti-tubulin and anti-clathrin) and secondary antibodies labeled with PAX<sub>560</sub> (yellow) and PAX<sub>480</sub> (cyan). Data were obtained sequentially by imaging PAX<sub>480</sub> first without UV light and subsequent PAX<sub>560</sub> with UV activation. The localization precision of single events was  $\sigma = 20 - 25$  nm. Scale bar: 1  $\mu$ m.

Both tubulin and vimentin are structures with a high density of fluorophore binding sites, allowing for a high apparent density of labeling and, thus are widely used as structures to evaluate the staining of new dyes in general. However, the structures are labeled with an uncountable number of fluorophores, which makes quantitative analysis more difficult. As a biological relevant standardized system one can pick nuclear pore complexes (NPC). Gene editing of the cell lines can facilitate linkers (e.g. HaloTag or eGFP) at an endogenous level and therefore they have an assignable number of binding sites [52]. As a consequence, MINFLUX imaging in section 3.2.3 was performed on NPCs after initial imaging in PALM microscopy (figure 4.8). The figure exhibits the labeling integrity of the characteristic ring-like structure, labeled with nanobodies and HaloTag respectively for PAX<sub>560</sub> and PAX<sub>+560</sub>.

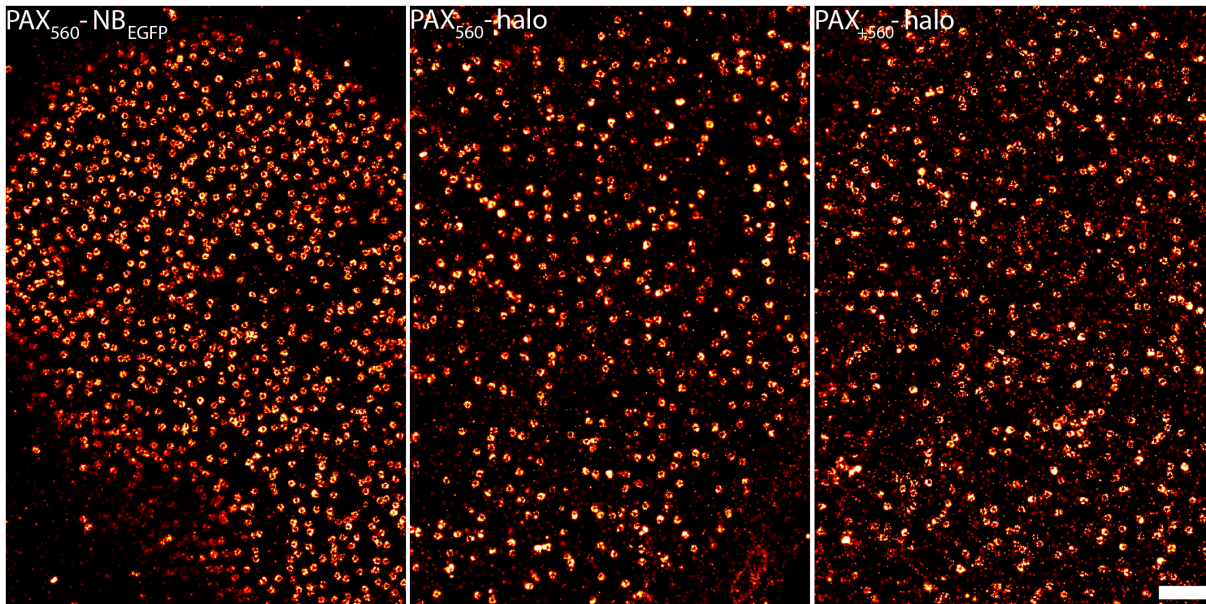


Figure 4.8: **Reconstructed PALM images of nuclear pore complexes.** The cells (mEGFP-Nup107, U2OS-Nup96-Halo) were labeled with either anti-GFP nanobody (fixed), or HaloTag (fixed before imaging) of PAX<sub>560</sub> or PAX<sub>+560</sub>. The reconstructed images have a localization precision of around  $\sigma = 15 - 20$  nm. Scale bar: 1  $\mu$ m.

### 4.2.3 MINFLUX Imaging

After demonstrating the general applicability of PAX for labeling of biological samples with different linker in fixed and live-cell conditions, the consecutive step was to show their suitability as fluorophores for MINFLUX nanoscopy. As stated in the previous section, an assignable number of fluorophores per binding site make nuclear pore complexes preferable for quantitative analysis, functioning as a standardized biological system. Therefore, in a first step mEGFP-Nup107 cells were labeled with primary nanobodies (PAX<sub>560</sub>) and consecutively U2OS-Nup96-Halo cells were labeled with PAX<sub>560</sub> and PAX<sub>+560</sub> chloalkane ligands. Both samples allow tagging with a smaller label compared to antibodies. Moreover, the cell lines are genetically engineered (CRISPR) cells, expressing the respective proteins at an endogenous level, allowing to target them with assignable numbers of the corresponding label. Thus, for U2OS-Nup96-Halo cells a single dye per protein (Nup96) can be facilitated. In an additional step, U2OS-CRISPR-Nup96-mMaple cells expressing mMaple at an endogenous level were imaged. The fluorescent protein has similar spectral properties and is to date the only orange fluorophore reported in MINFLUX nanoscopy before [8].

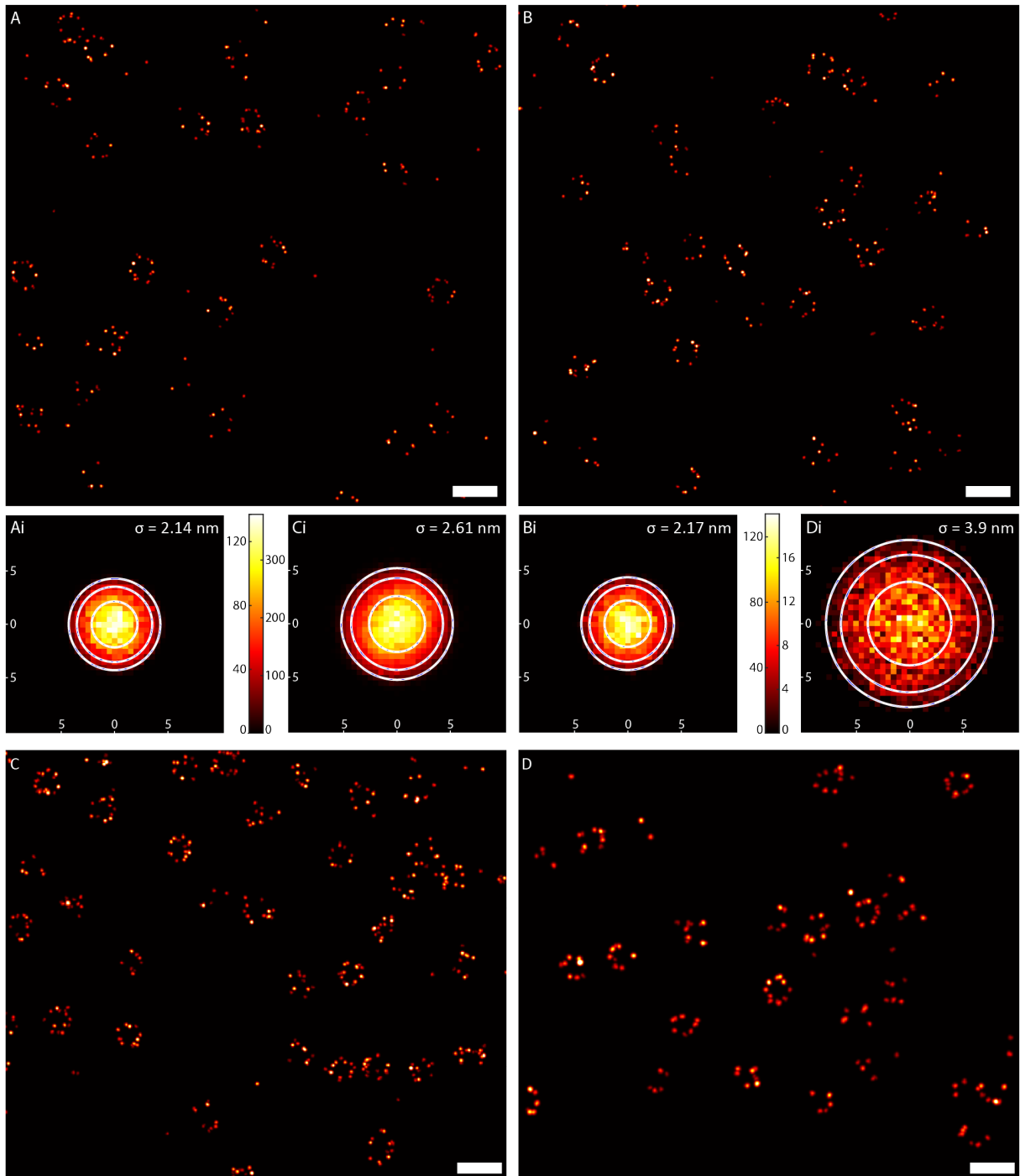


Figure 4.9: **MINIFLUX images of nuclear pore complexes.** Reconstructed MINIFLUX images of U2OS-Nup96-Halo fixed cells labeled with  $\text{PAX}_{560}$  (A) and  $\text{PAX}_{+560}$  (B) with a localization precision of  $\sigma = 2.14$  nm and  $\sigma = 2.17$  nm (Ai, Bi), respectively. C) mEGFP-Nup107 cells stained with an anti-GFP nanobody labeled with  $\text{PAX}_{560}$  (DOL=2) [34]. The corresponding 2D dispersion plot (Ci) visualizes the localization precision ( $\sigma = 2.61$  nm). D) U2OS-CRISPR-Nup96-mMaple (clone 16) cells imaged with a modified MINIFLUX sequence to take photo-bleaching and short term blinking into account. The average localization precision is  $\sigma = 3.9$  nm (Di). Scalebar: 200 nm.

Samples, labeled with bioconjugates of PAX<sub>560</sub> and PAX<sub>+560</sub>, were imaged with a standard imaging sequence by the manufacturer on a commercial MINFLUX setup. A detailed description of the setup and the image sequences can be found in section 7.1. In brief, the localization process starts after the detected fluorescence signal surpasses a threshold set by the manufacturer. The following sequence can be split into two parts: The first one suits as a pre-localization containing 4 steps with decreasing  $L$  (1 ms each) and requires a minimum of 120 photons (above the background). In the second part of localization, the sequence contains 2 steps (1 ms each,  $L_1 = 76$  nm and  $L_2 = 40$  nm, 30 photons per step), which are performed alternating until the fluorescence signal drops below the internal threshold. Thus, the recorded single emitter events consist of  $N$  localizations ( $N_{Loc}$ ), where  $N$  is the number of successful repeats of the last two steps. The localization precision of each event can be obtained from the distribution of the single localizations with respect to their mean position [8]. Furthermore, every single localization of the event has a time ID, as well as a distinct number of photons, adding up to a total localization time ( $T_{Loc}$ ) and a total number of photons ( $N_{Ph}$ ). Imaging U2OS-CRISPR-Nup96-mMaple cells with the same sequence showed a poor detection ratio of the fluorescent proteins, resulting in images with a low apparent density of labeling of the nuclear pore complexes. Addressing the photo stability and short term blinking of fluorescent proteins [70], a modified sequence for mMaple was utilized (provided by the EMBL Imaging Center), performing 3 steps with a final  $L = 100$  nm.

Table 4.3: **Image parameters obtained from the respective MINFLUX measurements.**

	$L$	Binning photons	$\sigma$ (nm)	$N_{loc}$ median	$N_{ph}$ median	$T_{loc}$ (ms) median	Rate (kHz) median	Phot <sub>Loc</sub> median
PAX 560 halo	40	100	2.14	16	4500	280	35	124
PAX +560 halo	40	100	2.17	17	5000	260	40	127
PAX 560 egfp	40	100	2.61	12	2400	665	19	122
mMaple	100	100	3.9	17	1700	120	37	148

Figure 4.9 depicts MINFLUX images of nuclear pore complexes labeled with the respective bioconjugates. After binning the detected events to slices of 100 photons per bin, the data was treated as described in section 2.2.2. Further analysis unveiled a localization precision of  $\sigma = 2.14$  nm and  $\sigma = 2.17$  nm for U2OS-Nup96-Halo cells labeled with the compounds PAX<sub>560</sub> and PAX<sub>+560</sub> (Ai, Bi), respectively. For mEGFP-Nup107 and U2OS-CRISPR-Nup96-mMaple a localization precision of  $\sigma = 2.61$  nm and  $\sigma = 3.9$  nm, respectively, was evaluated (Ci, Di). All calculated parameters are summarized in table 4.3. Although the number of photons per localization with the final  $L$  (Phot<sub>Loc</sub>) did not vary significantly, in case of mMaple the localization precision is reduced. The reduction can be explained by the enlarged scanning range  $L$  compared to the other measurements (see figure 1.8). The nanobody conjugate of PAX<sub>560</sub> showed significant

undesirable activation by excitation, coupling imaging with the discrimination criteria of single fluorophores. Therefore, excitation power was reduced to minimize the activation ensuring only one active emitter in a diffracted limited spot. Thus, a reduction of the average rate and therefore longer localization times was observed. PAX<sub>560</sub> halo and PAX<sub>+560</sub> halo in contrast, didn't show any significant activation without UV illumination confirming single molecule measurements (section 4.2.1). Also, no significant deviation of the evaluated parameters could be witnessed, as the images have a comparable number of photons ( $N_{ph}$ ) localizations per event ( $N_{loc}$ ) and localization precision  $\sigma$ . This was also confirmed for moderate excitation powers in single molecule measurements, resulting in a comparable average number of photons in the several thousand regime (see section 4.1).

#### 4.2.4 Apparent density of labeling in MINFLUX and PALM Imaging

The previous section demonstrated that PAX dyes can be utilized to image in MINFLUX nanoscopy. However, as they possess a single fluorescent on-cycle, there is only one chance to localize them. If the localization of the fluorophore fails, the structure appears unlabeled/under-labeled. Conclusively, the localization efficiency is from high importance for photoactivatable dyes and affects the image quality in the such a way as the density of labeling (DOL). For instance for gene edited U2OS-CRISPR-Nup96-mMaple cells a single label per protein can be ensured, but still the labeling can appear incomplete, if localizations fail. Therefore both, the detection ratio and the DOL, are summarized as apparent density of labeling (ADOL).

To evaluate the ADOL of the PAX compounds measured with MINFLUX nanoscopy, images of U2OS-Nup96-Halo cells labeled with PAX<sub>560</sub> and PAX<sub>+560</sub> chloralkane ligand were analyzed, taking the number of detected corners per nuclear pore complex into account. The cells express the Nup96 protein twice per corner and plane and thus, a complete labeling should result in two fluorophores per corner and plane. In an additional step, data taken from the same sample by PALM microscopy was compared with the former data sets. The focus lay on the occupancy of labeled corners per nuclear pore complex, evaluating the localization efficiency of MINFLUX nanoscopy with respect to an established method. Moreover, data sets were compared with data obtained from U2OS-CRISPR-Nup96-mMaple cells, which express mMaple at each Nup96 (DOL=1). Therefore, in a best case scenario the U2OS-Nup96-Halo were labeled with exactly the same amount of dyes. The second reason utilizing U2OS-CRISPR-Nup96-mMaple cells as a control is the fact that its a photoactivatable dye with similar spectral properties.

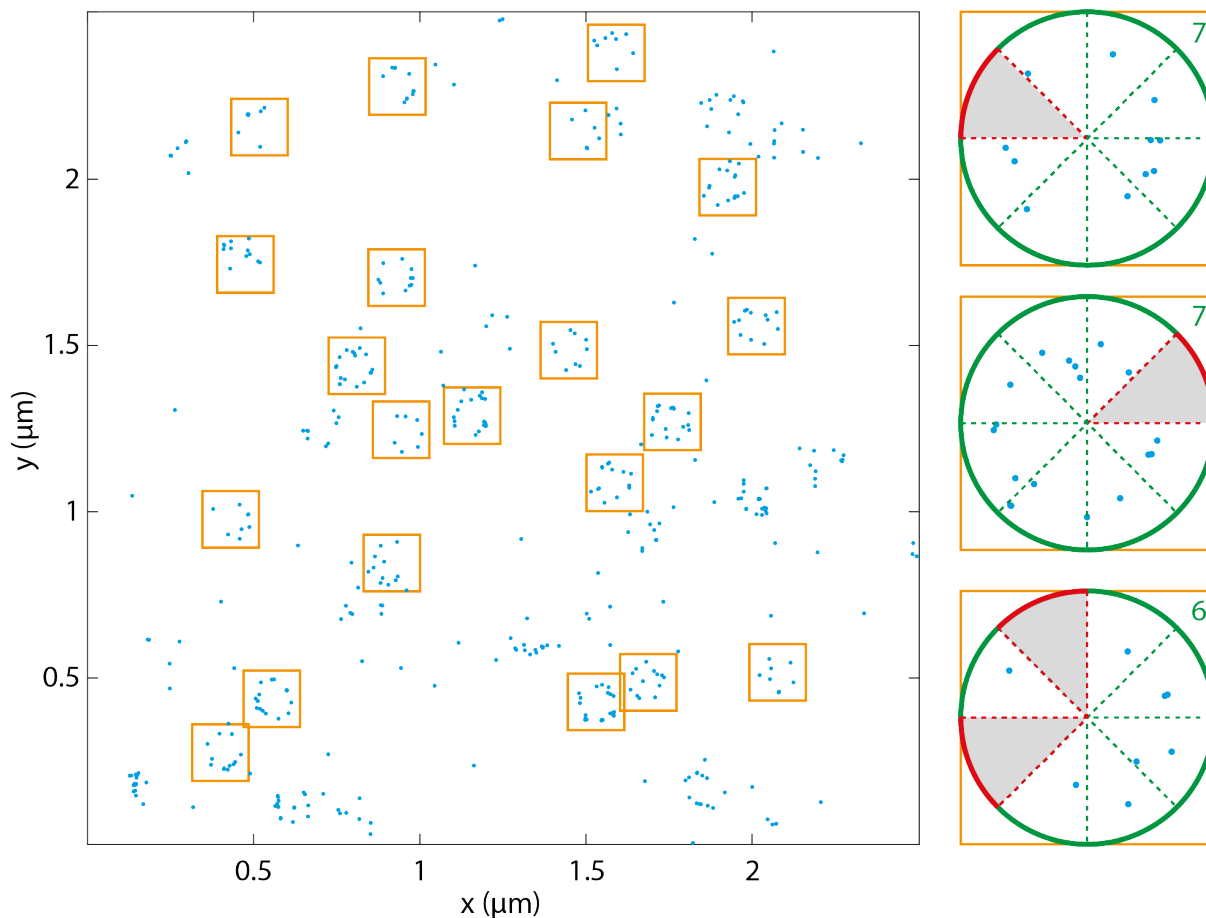


Figure 4.10: **Visualization of the algorithm utilized for occupancy analysis of MINFLUX data.** The scatter plot shows data obtained with MINFLUX of nuclear pore complexes labeled with  $\text{PAX}_{+560}$  chloralkane ligand. The algorithm fits rings through the nuclear pore complexes evaluating the center of each NPC. In a second step its 8-fold symmetry is utilized to split the nuclear pore complex in 8 wedges, maximizing their occupation.

The estimation of the occupancy was performed by Jan Keller (Ph.D. MPI for multidisciplinary nature sciences) analogous to [52]. MINFLUX results were rendered and all circular, isolated structures identifiable as NPCs were manually selected as regions of interest (see figure 4.10A). All localizations (combined single molecule blinking events) within a single region of interest (a single NPC) were rendered and the rendering fitted with a ring of variable center, diameter and width. The center of the fitted ring was then subtracted from all coordinates and all localizations within a reasonable radius (40-70 nm away from the origin) were distributed in 8 equal angular bins (corresponding to 45 deg wide wedges). The localizations were rotated so that a maximal number of localization fell into a single bin, avoiding that a bin edge divides a NPC subunit in half. All bins with at least one localization contained were counted as occupied (see figure 4.10B).

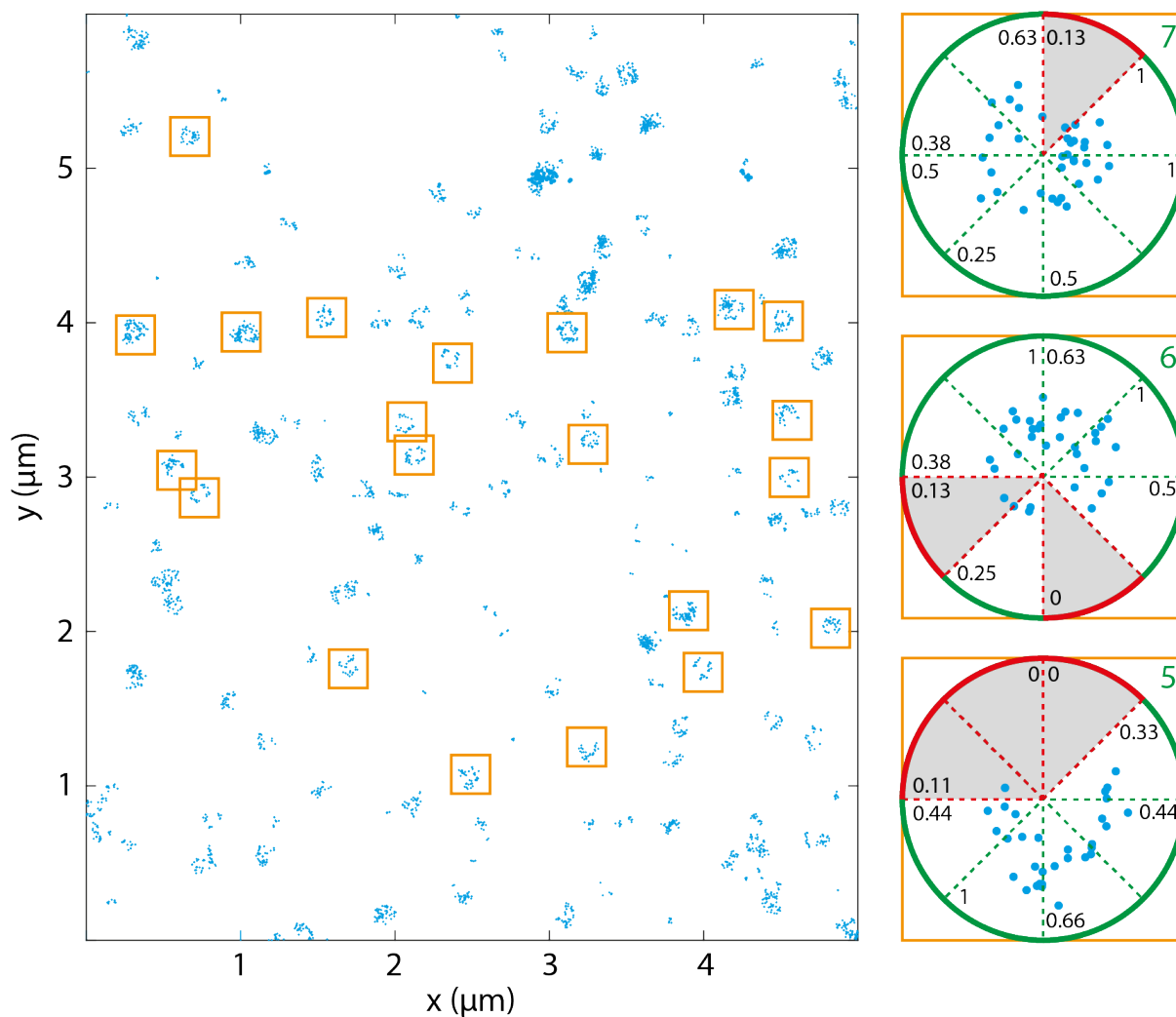


Figure 4.11: **Visualization of the algorithm utilized for occupancy analysis of PALM data.** The scatter plot shows data obtained with PALM of nuclear pore complexes labeled with PAX<sub>+560</sub> chloralkane ligand. The algorithm fits rings through the nuclear pore complexes evaluating the center of each NPC. In a second step its 8-fold symmetry is utilized to split the nuclear pore complex in 8 wedges, maximizing their occupation. Wedges with less than 20% signal with respect to the largest bin were eliminated.

From images obtained with PALM nanoscopy however, localizations were evaluated as described in section 7.3. The results were rendered and all isolated structures identifiable as NPCs with a clear hole (absence of localizations) in the center were manually selected as regions of interest (see figure 4.11A). All localizations (combined single molecule blinking events) within a single region of interest (a single NPC) were rendered and the rendering fitted with a ring of variable center, diameter and width. The center of the fitted ring was then subtracted from all coordinates and all localizations within a reasonable radius (40-70 nm away from the origin) were distributed in 8 equal angular bins (corresponding to 45 deg wide wedges). The localizations were rotated so that a maximal number of localization fell into a single bin, avoiding that a bin edge divides a NPC subunit in half. All bins with at least 20% of localizations of the bin with most of the localizations were

counted as occupied (see figure 4.11B), as clear separation of single bins was not possible due to the localization precision. It should be noted that the fraction of selected NPCs from all recorded NPCs is quite low, because many NPCs in the PALM image do also show localizations at the center of the NPC and thus, failing our filtering criteria.

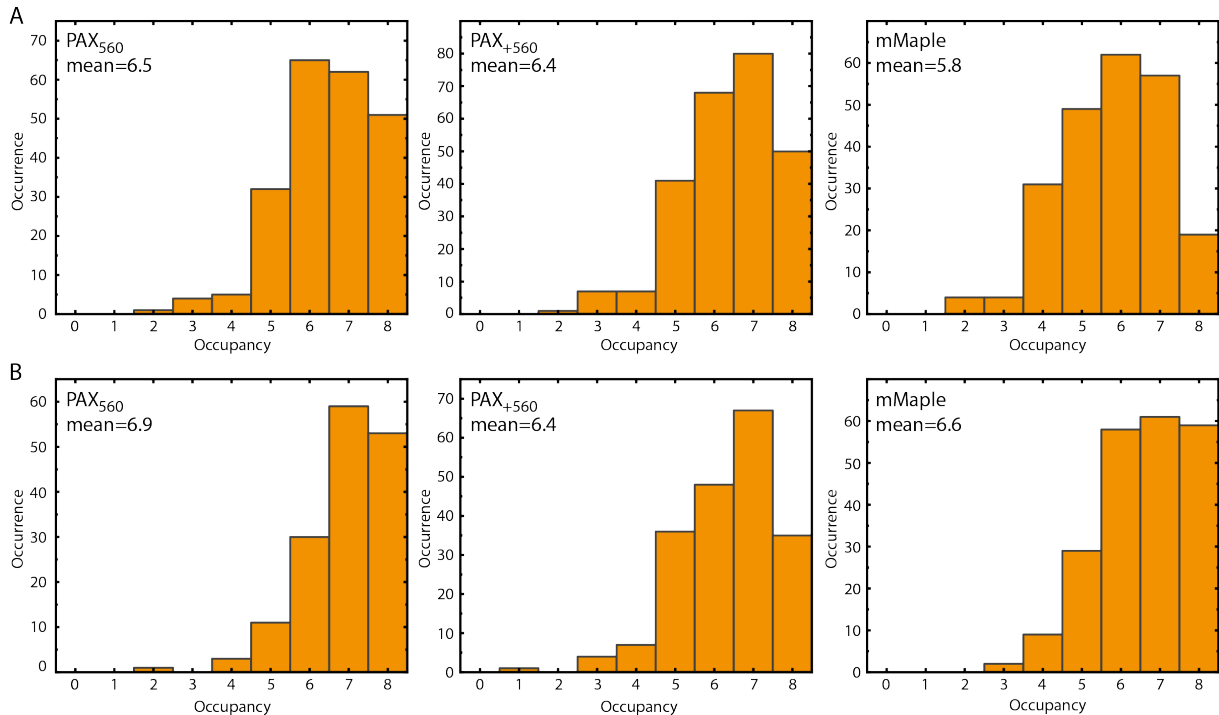


Figure 4.12: **Histograms with apparent density of labeling.** A) The apparent density of labeling of nuclear pore complexes labeled either via Halo (PAX<sub>560</sub> and PAX<sub>+560</sub>), or expressing mMaple at endogenous level taken with MINFLUX nanoscopy. The data depict a slight decrease for the ADOL in case of mMaple, which can be addressed to unsuccessful localizations caused by triplet blinking. B) The apparent density of labeling of nuclear pore complexes labeled either via the chloralkane ligand (PAX<sub>560</sub> and PAX<sub>+560</sub>), or expressing mMaple at endogenous level taken with PALM microscopy. The data depict no tendency for the ADOL. For the chloralkane ligands no tendency for either microscopy technique can be observed. Data represents multiple ROIs including  $\approx 200$  nuclear pore complexes.

The histograms in figure 4.12 visualize the distribution of detected corners for U2OS-Nup96-Halo cells labeled with PAX<sub>560</sub> and PAX<sub>+560</sub> or U2OS-CRISPR-Nup96-mMaple cells expressing the fluorescent protein. Data were obtained with MINFLUX nanoscopy (figure 4.12A) and PALM microscopy (figure 4.12B), averaging  $\approx 200$  nuclear pore complexes for each measurement. No significant difference was observed between labeling (chloralkane ligands vs. endogenous expression of PAX of mMaple) or different dyes (PAX<sub>560</sub> vs. PAX<sub>+560</sub>) for PALM microscopy. Furthermore, also no significant deviation between PALM and MINFLUX measurements of PAX<sub>560</sub> vs. PAX<sub>+560</sub> can be witnessed. For mMaple however, there is a clear decrease of detected corners, which was expected, due to the high rate of triplet blinking influencing the MINFLUX localization process.

### 4.3 Discussion

In this section photoactivatable xanthenes (PAX) dyes were investigated with respect to their applicability in MINFLUX nanoscopy. All compounds investigated fulfilled the basic requirements for MINFLUX, meaning sufficient event duration, sufficient photon numbers and uncaging to grant the discriminability criteria. However, two of the five characterized compounds showed a reliable uncoupled switching behavior making them favorable for MINFLUX nanoscopy. The two compounds, excited at  $\lambda = 560$  nm, could be imaged with a localization precision of  $\sigma \approx 2$  nm achieving a similar performance to established red-emitting fluorophores.

MINFLUX images of NPCs stained with PAX<sub>560</sub> and PAX<sub>+560</sub> chloralkane ligand were analyzed with respect to the apparent density of labeling. Simulations of the detection ratio and the number of labels in section 1.3 showed a high variability of the probability distributions. The interweaving of both parameters cannot be resolved by the designed experiment as one cannot guarantee a complete labeling of the sample. If one assumes complete labeling (four dyes per corner) simulations yield an average ADOL of  $mean_{ADOL} = 6.57$  for a detection ratio of  $DR = 0.35$  of all events. However, assuming a labeling efficiency of 50%, a detection ratio of  $DR = 0.57$  is necessary to accurately fit the distribution measured with PAX<sub>560</sub> and PAX<sub>+560</sub> compound, showing the high variance caused by the interweaving of the variables. As absolute numbers are difficult to obtain, a comparison with other techniques and previous reports is favorable. Thevathasan et al. [52] made a comprehensive study on nuclear pore complexes functioning as standardized structure in nanoscopy. They observed an apparent density of labeling of about 55% for mMaple in NPCs imaged in the same cell line, which corresponds to an ADOL of about  $mean_{ADOL} = 4.4$  compared to  $mean_{ADOL} = 6.6$  evaluated in this thesis. As the experimental parameters (laser power, instrumentation etc.) vary, a deviation is expected. However, the analysis utilized in this thesis depends on a threshold for evaluating the occupancy of the single NPCs, which increases the uncertainty. Moreover, separating individual NPCs with less than three detected corners by a circular fit from the background isn't feasible unambiguously, which suppresses this part of the distribution. This indicates an overestimation of the ADOL for data acquired with PALM microscopy. As MINFLUX data isn't depending on a set threshold the evaluation of the occupancy should be of less uncertainty. Furthermore, the improved resolution reduced the ambiguities in the identification as one can observe in figure 4.10. All in all these finding indicate a detection success in MINFLUX nanoscopy comparable to established techniques.

# Chapter 5

## Applications of irreversible switches

The photoactivatable xanthenes studied in the previous chapter operate as reliable, controllable fluorescent switches for MINFLUX nanoscopy. Their functionality opens the door for various applications of biological relevance. Two applications were chosen as examples for the widespread applicability of these fluorescent compounds.

In section 5.1 the irreversible mechanics of the PAX compounds were exploited to resolve the binding sites on individual fluorescent labels, namely nanobodies, unambiguously.

Dual color MINFLUX imaging was performed with PAX<sub>560</sub> and PAX<sub>570</sub> in section 4.2.3. The spectral separation in emission enabled their discriminability.

The study presented in this chapter resulted in a publication of Rimmel et al. (in preparation). Analysis of the data was performed in exchange with Mariano Bossi (Ph.D, Optical Nanoscopy, MPIImR, Heidelberg) and Tobias Engelhardt (Ph.D, Abberior, Heidelberg).

### 5.1 Resolving the Fluorescent Label

MINFLUX nanoscopy enables a localization precision in the lower single digit nanometer regime down to 1 nm [9]. However, as a fluorescence microscopy technique, it obtains information from single fluorophores of  $\approx 0.5$  nm or single digit nanometer sized fluorescent proteins. These are attached to the structure of interest via a bioconjugate. Common bioconjugates are antibodies, HaloTag, SnapTag or nanobodies with a size of 10 – 1 nm. Thus, the spatial deviation between the fluorescent probe and the structure of interest is expected to be relevant for the interpretation of data taken with MINFLUX nanoscopy.

To verify the relevance of labeling, commercial nanobodies (FluoTag®-X2 anti-Rabbit IgG) were labeled with PAX<sub>560</sub> maleimides, attached via cystein terminated linkers to the C- and N-terminus of the nanobody. The cystein linkers consist out of 5 or 6 amino acids respectively. The distance of both fluorophores should be in the few nanometers range and thus resolved by MINFLUX nanoscopy. As fluorescence microscopy only detects the fluorescent probe and not the structure, these measurements highlight the importance of its size and position with respect to the label and the structure of interest.

The nanobodies were imaged with a custom-built interferometric MINFLUX microscope described in detail in [71, 72]. A brief description can be found in section 7.2. As the sample does not possess any counter-labeling an initial  $10 \cdot 10 \mu\text{m}^2$  xy-scan was performed to find candidates, illuminating the sample with the excitation laser only. Pre-activated single fluorophores were detected and, if succeeding a given photon threshold, its position pre-determined by Gaussian fitting. The iterative MINFLUX routine was performed at those positions ( $p_{ex} = 260 \mu\text{W}$  at the last MINFLUX step); subsequently UV illumination ( $\lambda = 405 \text{ nm}$ ) was turned on at nanowatts power after around  $t = 0.9 \text{ s}$ , to uncage the second fluorophore. Pre-selected traces possessing two time-wise distinguishable events (see figure 5.1B) were used for further evaluation. By a dedicated matlab script data were binned, filtered with a DBScan algorithm and visualized.

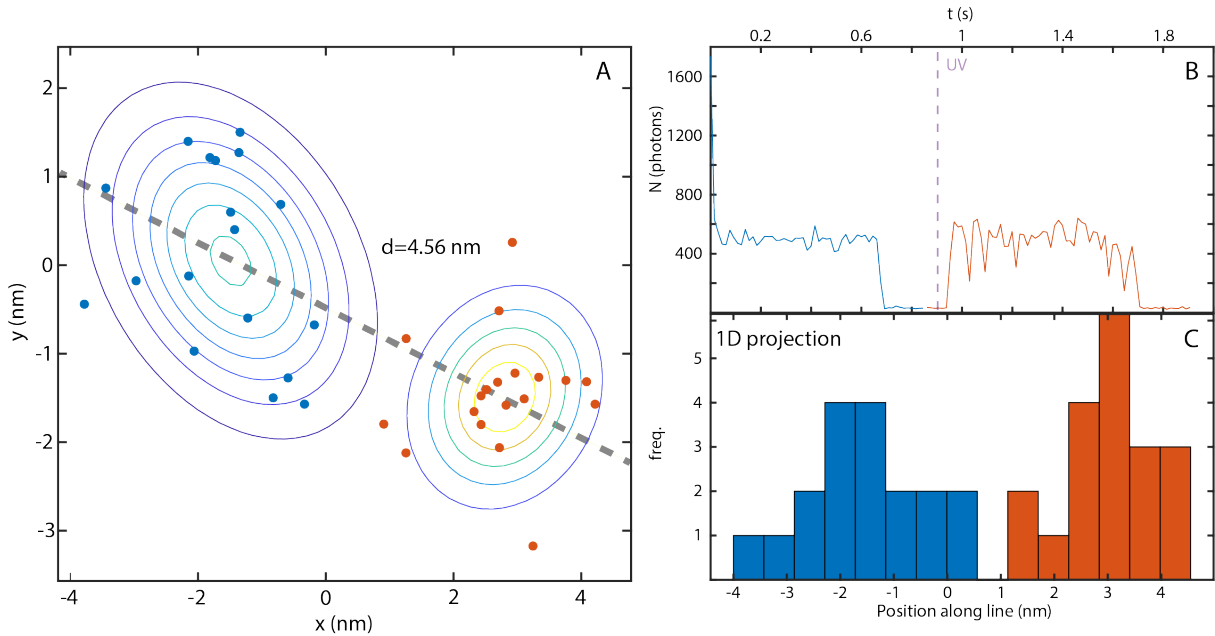


Figure 5.1: **Exemplary localization clusters representing a double labeled nanobody.** A) A 2D scatter plot displaying localizations obtained from the respective fluorescence events. Both distributions are fitted by 2D Gaussians allowing the evaluation of the center positions and their distance  $d = 4.56 \text{ nm}$ . B) The corresponding time trace of the fluorescent events. C) A histogram visualizing a 1D projection of the localizations through the fitted centers (A, grey line).

Figure 5.1 shows an exemplary measurement of a nanobody labeled with two PAX<sub>560</sub> maleimides. The time trace (figure 5.1B) shows a second fluorescence event emerging after a UV pulse at  $t = 0.9$  s. Localizations were binned by a factor of 5 and visualized as a 2D scatter plot (figure 5.1A). 2D Gaussians are fitted to the single distributions to evaluate the center of the events and their distance ( $d = 4.56$  nm). By projecting the data onto a single axis connecting the centers of both distributions one can visualize the data in a 1D histogram (see figure 5.1 C).

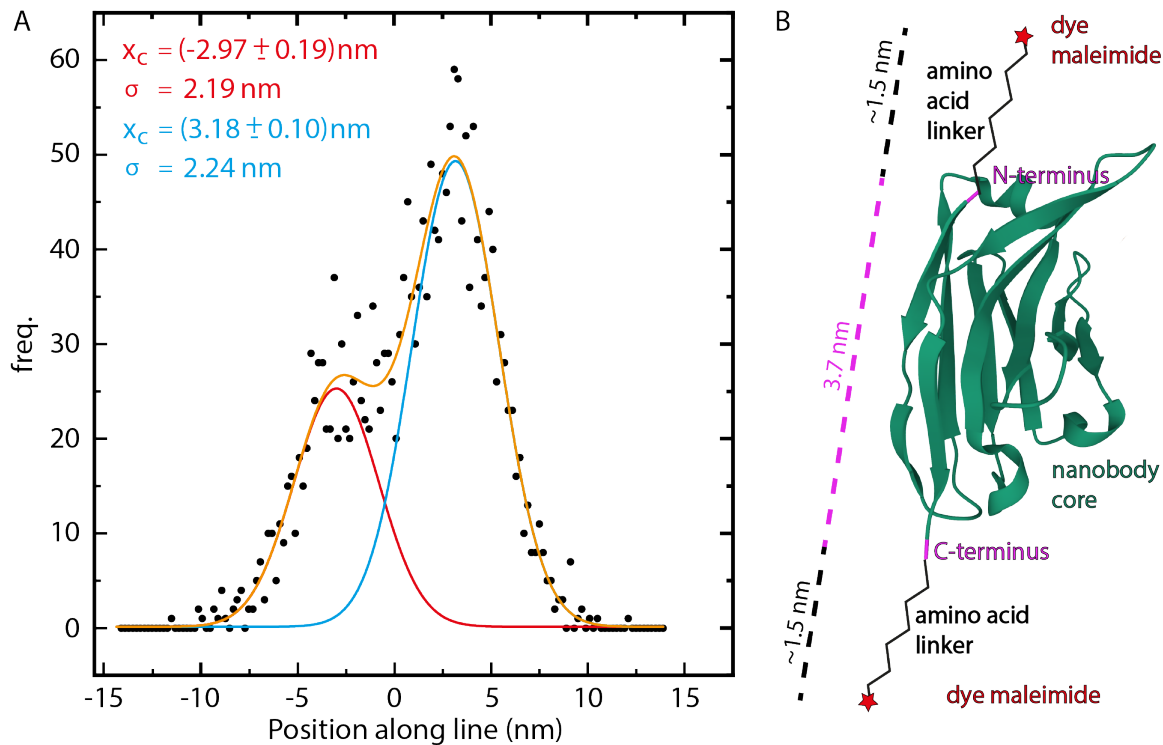


Figure 5.2: **Localizations projected into a single dimension.** A) The plot displays all localizations obtained from 30 measurements binned by a factor of 2 and projected onto a single axis normalized with respect to their center of mass. Two Gaussians are fitted through the distribution. The standard deviation of the fits is  $\sigma = 2.19$  nm and  $\sigma = 2.24$  nm, while the peak to peak distance is  $d = 6.21$  nm. B) A Model of a FluoTag®-X2 anti-ALFA nanobody, which possesses a different tag but consists out of a similar nanobody core. The crystallized structure ( $d = 3.7$  nm C- to N-terminus) is extended by a sketch of the linkers connecting the dye conjugates to the nanobody. The linkers consist out of 5 (6) amino acid attached to the C-terminus (N-terminus) of the nanobody core, respectively ( $d \approx 1.5$  nm).

Figure 5.2A) displays all localizations (binned by a factor of 2) obtained from 30 measurements, projected onto a single axis shifted by the corresponding positions centers. The noticeable height deviation of the two peaks can be explained by the nature of the analysis: as the events are separated in time, the left peak represent data of the first fluorescence event. On average the rate of the first fluorescent event was increased around 25% compared to the second, resulting in a shorter  $T_{On}$  and thus less localizations. This

might either originate from the orientation of the fluorescent probes with respect of the polarization axis of the excitation laser or from the micro-environment the fluorophore is experiencing, as there are two different termini the single fluorophores are attached to. Two Gaussians are fitted through the respective peak of the distribution yielding a standard deviation of  $\sigma = 2.19$  nm and  $\sigma = 2.24$  nm respectively. Thereby, the distance  $d = 6.21$  nm between the peaks could be resolved.

To date, no crystal structure of the employed nanobody has been published. However, the crystal structure of a similar nanobody (FluoTag®-X2 anti-ALFA) distributed by the same manufacturer is well-known and depicted in figure 5.2B. The manufacturer states that the fluorophores are attached to the C-terminus and the N-terminus by 5 and 6 amino acids respectively; thus, a size of  $d = (1.5 - 1.8)$  nm is estimated per binding site ( $0.35\text{\AA}$  per amino acid). Added to the distance between both terminus of the nanobody, one would expect a maximal fluorophore distance of  $d = (6.7 - 7)$  nm, which is in perfect agreement with the experiment.

## 5.2 Dual Color MINFLUX Imaging

To expand the applicability of PAX compounds, for instance in co-localization experiments, dual color MINFLUX imaging was performed, exploiting the spectral difference of PAX<sub>560</sub> and PAX<sub>570</sub>. Figure 5.3A shows the spectral properties of both dyes in combination with the properties of the detection channels of the MINFLUX microscope. The emission spectra of both compounds has a reasonable separation for single molecule discrimination in the Cy<sub>3</sub> and the Cy<sub>5, near</sub> spectral channels (filter based). The signal of both channels is used to evaluate a photon ratio of the detected events between the channels, which enables the assignment of every single molecule event to the corresponding dye in post processing. Unfortunately, the peak maximum of PAX<sub>570</sub> fell on the 640 nm laser line of the setup, and thus the detection filter blocks a considerable fraction of the emission signal.

To enable unambiguous results, for the first color PAX<sub>560</sub>, well-studied and characterized in the previous chapter, was selected. To this end, U2OS-Nup96-Halo cells were labeled with a chloralkane adduct of PAX<sub>560</sub>. For the second color primary and secondary combinations were tested. As the nanobody-PAX<sub>570</sub> showed poor specificity a secondary antibody-PAX<sub>570</sub> was chosen to compensate for the expected minor localization efficiency. Figure 5.3B depicts a reconstructed MINFLUX image of NPCs containing the indiscriminate signal of both detection channels (Cy<sub>3</sub> and Cy<sub>5, near</sub>).

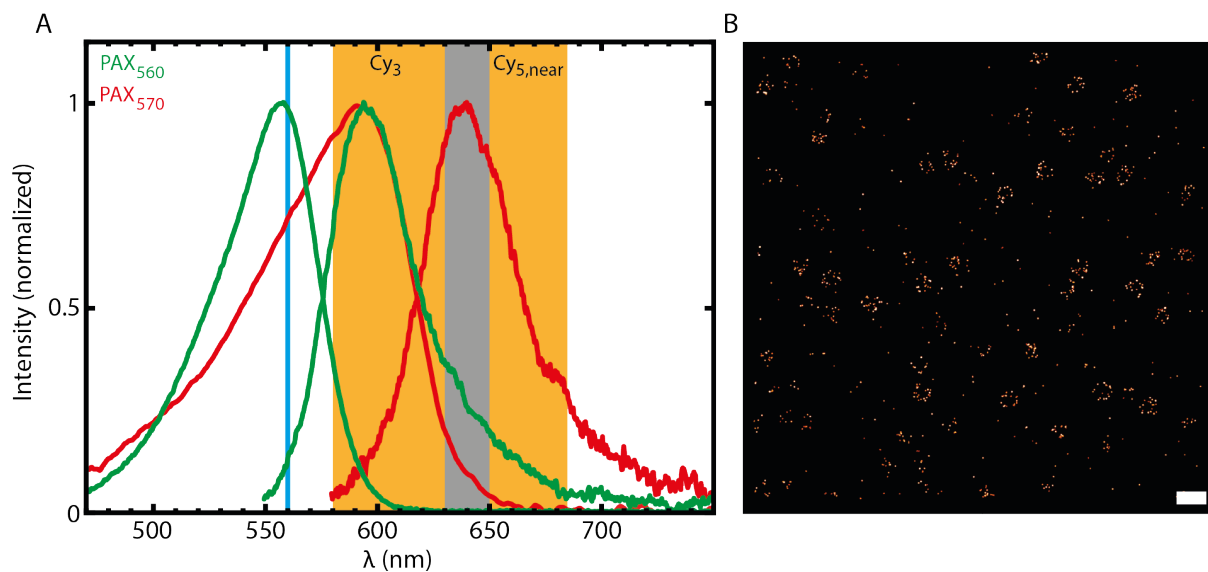


Figure 5.3: **Dual color MINFLUX imaging with PAX dyes.** A) Excitation and emission spectra of PAX<sub>560</sub> (green) and PAX<sub>570</sub> (red) with respect to the excitation wavelength (blue) and the detection channels (Cy<sub>3</sub> and Cy<sub>5, near</sub>) of the MINFLUX microscope (orange). The emission maximums of the compounds are well separated. However, due to the 640 nm line of the microscope, signal originated from PAX<sub>570</sub> is mostly blocked by filters. B) A reconstructed MINFLUX image containing the signal both channels indiscriminate. Scalebar: 200 nm.

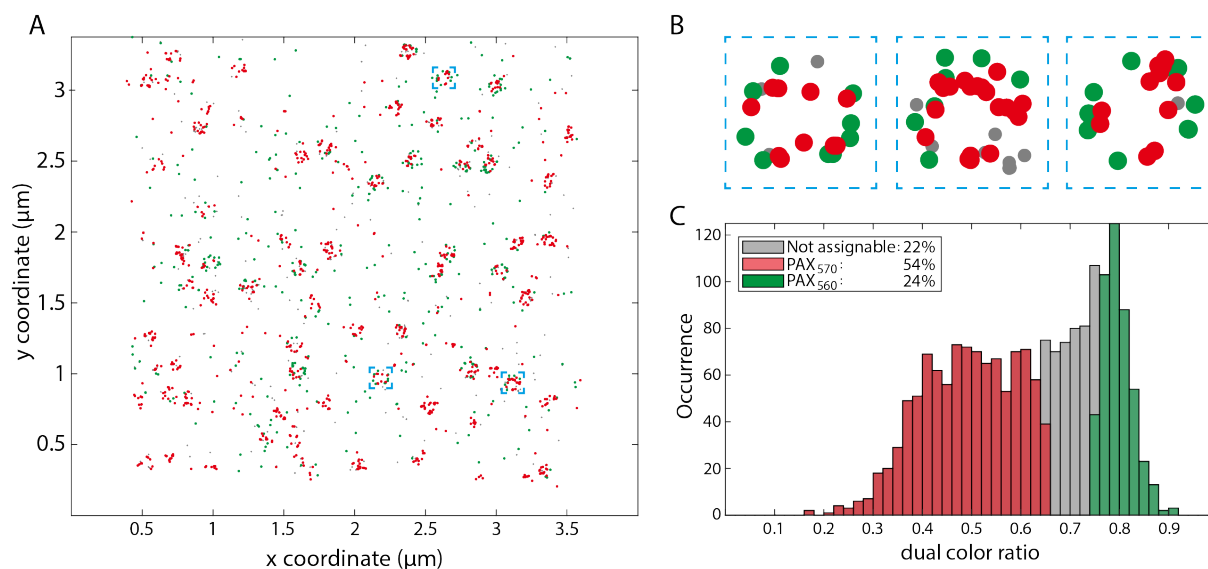


Figure 5.4: **Filtered events discriminated by dual color ratio (DCR).** A) Filtered events of figure 5.3B in a scatter plot after color assignment by their dual color ratio (DCR). Events originated from PAX<sub>560</sub>/PAX<sub>570</sub> are plotted in green/red, while filtered out events (grey) could not be assigned unambiguously. B) Exemplary NPCs from A enlarged. C) Histogram with the localization distribution as a function of the DCR.

MINFLUX localizations obtained in the measurement were plotted as a function of their dual color ratio ( $\text{DCR} = \text{Ph}_{Cy3} / (\text{Ph}_{Cy5, \text{near}} + \text{Ph}_{Cy3})$ ) in figure 5.4B. The distribution possesses a peak at  $\text{DCR} \approx 0.8$  (PAX<sub>560</sub>) and a widespread peak at  $\text{DCR} \approx 0.6$  (PAX<sub>570</sub>). Control experiments with single labeled structures show either one of those distributions, confirming this assignment. To minimize ambiguities in the assignment, data with  $0.65 \leq \text{DCR} \leq 0.75$  were eliminated. The resulting scatter plot with the respective assignment (PAX<sub>560</sub> green, PAX<sub>570</sub> red, filtered grey) is depicted in figure 5.4A. For both colors, ring-like structures can be observed.

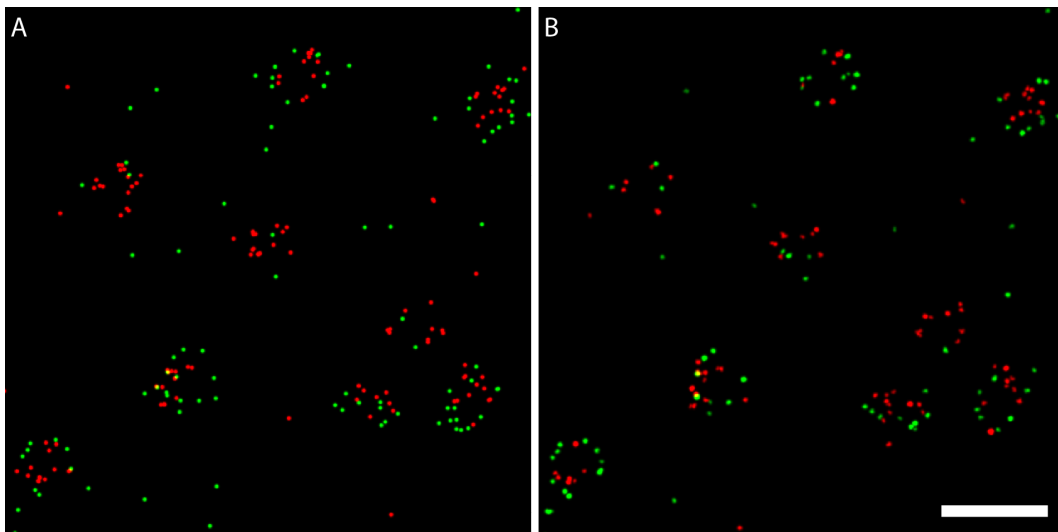


Figure 5.5: **Excerpt of the reconstructed MINFLUX image (see figure 5.4B) splitted by DCR and time.** A) shows a reconstructed MINFLUX image of NPCs stained with PAX<sub>560</sub> (green) and PAX<sub>570</sub> (red) separated by DCR. B) shows a reconstructed MINFLUX image of NPCs stained with PAX<sub>560</sub> (green) and PAX<sub>570</sub> (red) separated by the measurement time. Two exemplary NPCs are enlarged showing the similarity of the two images. Scalebar: 200 nm.

Initial measurements in PALM microscopy of PAX<sub>570</sub> antibodies showed substantial activation with 560 nm illumination. This shows incomplete uncoupling of the excitation and the activation processes of this dye, which is undesirable for MINFLUX nanoscopy in general, as discussed in the previous chapters. For two-color imaging however, combination with a fluorophore activating in an uncoupled manner, lead to orthogonal switching mechanisms (by activation rate). This also enabled two-color imaging separating the event by time (before and after UV activation) and functions as a control for the initial experiment. Reconstructed MINFLUX images of the same ROI showing both, two-color separation by spectral splitting and measurement time, are depicted in figure 5.5. The images show a strong similarity, which was expected as UV activation was turned on after no significant amount of localizations was registered over a time window of five minutes. The DCR histogram containing only events before UV activation shows a single peak centered at  $\text{DCR} \approx 0.55 - 0.60$ .

For higher statistical relevance of the evaluation the image of six NPCs was averaged. This addresses the minor localization efficiency and the deformation of the inner structure due to the size of the antibodies complex ( $\approx 15$  nm). All ringlike structures were selected by an algorithm fitting a circular template to the event clusters and calculating each center. For averaging NPCs those with two circular fits inside each other were selected and plotted by stacking the images of the respective color, separately. The overlay is plotted in figure 5.6B. For Nup96, stained with PAX<sub>560</sub> chloralkane ligand, the symmetric ringlike structure is clearly visible. The averaged signal of Nup98 looks slightly more deformed as expected. The pixel signal is plotted in dependence of the radial coordinate for the respective color, resulting in an average radial profile. By fitting a Gaussian to the respective distribution the peak centers are evaluated to be  $x_{nup98} = 38.8$  nm and  $x_{nup96} = 52.4$  nm. The standard deviation  $\sigma$  is partly attributed to the overlapping error of the single NPCs, convoluted with the localization precision. Furthermore, the peak fitting of the inner circle shows a more widespread distribution of PAX<sub>570</sub> fluorophores resulting from the larger size of the antibody complex.

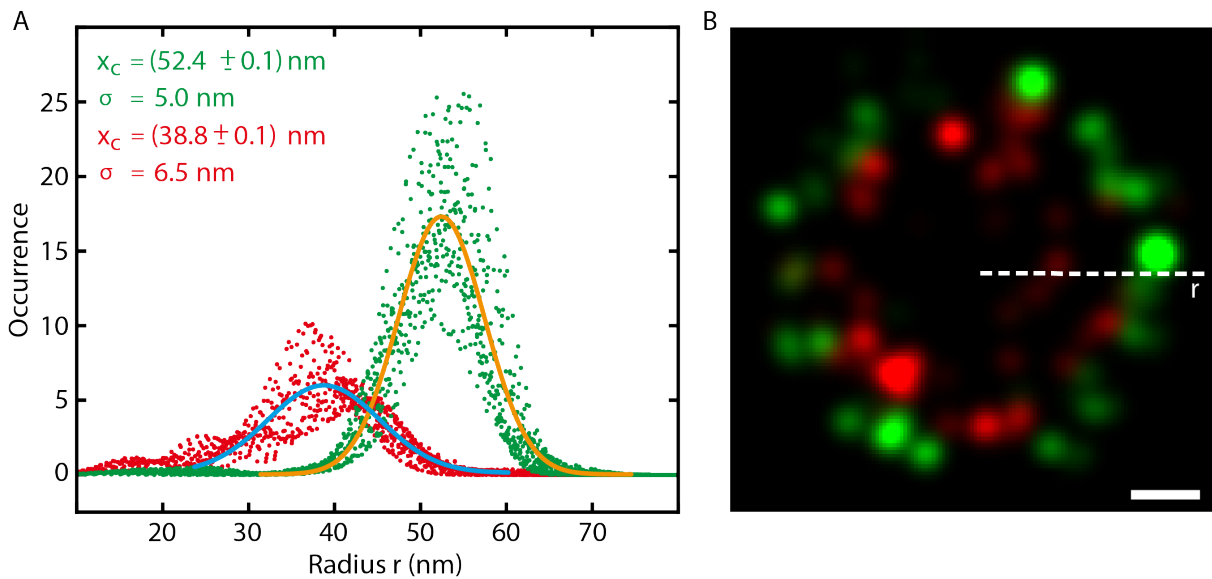


Figure 5.6: **Averaged Radial distribution of the signal of NPCs.** The averaged radial distribution of the localizations is fitted by two Gaussians. The fit representing PAX<sub>570</sub> has a significant standard deviation, which is addressed to the antibody labeling. However, the peaks are distinguishable with their centers being  $x_{nup98} = 38.8$  nm and  $x_{nup96} = 52.4$  nm. Scalebar: 20 nm.

## 5.3 Discussion

With a weight of  $\approx 15$  kDa nanobodies represent a label with one of the smallest sizes (SnapTag 19.4 kDa, HaloTag 33 kDa) and are the current the state of the art. Still a size of a few nanometers is expected for them, larger than the MINFLUX localization precision. In this thesis the irreversible switching mechanism of the PAX fluorophores was exploited to unambiguously resolve the individual size of nanobodies. The intra-label distance of single nanobodies was evaluated to be  $d \approx 6.21$  nm fitting the maximal expected distance of  $d \approx 6.7 - 7.0$  nm. Recent studies of antibodies and nanobodies (FluoTag®-X2 anti-ALFA, FluoTag®-X2 anti-GFP) with the aid of expansion microscopy presented a size of approximately  $d \approx 60$  Å for nanobodies with a similar corpus [73], confirming the results. The results show that MINFLUX challenges one of the smallest and most utilized labeling strategies. Thus, labeling with even shorter linkers or shorter recognition scaffolds are necessary.

Two-color imaging was performed by staining different proteins on the nuclear pore complex located in the outer ring (with a chloralkane ligand of PAX<sub>560</sub>) and the inner ring (with an antibody complex labeled with PAX<sub>570</sub>). Spectral splitting of the compounds enabled the identification of the two rings and their sizes could be evaluated by averaging NPCs ( $x_{nup98} = 38.8$  nm and  $x_{nup96} = 52.4$  nm). Previous reports studying the sizes of NPCs evaluated the radius of Nup96 to be  $x_{nup96} = 56.2 \pm 10.2$  nm [74], while the radius of Nup98 was evaluated to be ( $x_{nup98} = 43.5 \pm 16$  nm) [75]. Both are in good agreement with the results presented in this thesis.

# Chapter 6

## Conclusion and Outlook

By the combination of the target-coordinated and the target-stochastic approach MINFLUX nanoscopy exploits the advantage of having both a reference coordinate for localization and the discriminability of single emitters by fluorescent on- and dark off-states. This conceptually new approach utilizes a minimum in the excitation intensity distribution to inject the reference coordinate. With a set of exposures in the vicinity of the emitter, its position is estimated. An iterative measurement routine during which the spatial separation  $L$  between the reference coordinate and the estimated fluorophore position is lowered step by step, allows for a more precise position estimate with every step. This strategy enables nanometer precision with moderate photon numbers in the regime of a few thousands in 2D [7] and 3D [8, 9]. With the introduction of the scanning range  $L$  the localization precision no longer depends only on the number of photons. This paradigm shift motivates dye research, which mostly used to focus on photostability, with attention to other parameters more relevant to MINFLUX nanoscopy. As the localization efficiency (namely speed and success) depends on both the measurement routine (microscope side) and the properties of the single emitters (fluorophore side), it is possible to optimize the MINFLUX performance via characterization of the fluorophore properties most relevant to the MINFLUX scheme, and the subsequent adaption of the measurement routine to those properties. One core issue remaining affects the fluorophores in vicinity of the to-be-localized emitter: while the target dye is protected from high intensities preventing the population of higher states and possibly faster photo-degradation, fluorophores outside the center of the node are still exposed to high excitation intensities. Thus, complete decoupling of the mechanisms (i.e. on-, off-switching and excitation) is extremely relevant. Due to its novelty, the first experiments with MINFLUX nanoscopy had been performed with cyanine dyes optimized for STORM microscopy, exploiting thiol-based switching (i.e. bi-molecular reactions in oxygen depleted systems) [7–9, 66]. The unnecessarily high number of photons per on-cycle and the coupling of the photoswitching to the excitation

---

is disadvantageous and paid by a lowered localization efficiency. Thus, a search for fluorescent switches with alternative mechanisms and specific design for the requirements of MINFLUX becomes relevant, and thus is the aim of this work.

Consequently, a consistent characterization strategy for a systematic fluorophore screening was established within the presented research work. In the first step, a versatile optical microscopy setup was designed and built, enabling fluorescent microscopic measurements with single molecule sensitivity in either confocal or wide-field mode and the fast exchange of both configurations. The main focus of the design was the comparability of measurements performed in the respective configurations and possible adaption for structural modifications of the dyes. This was facilitated by two independent beam paths allowing for sequential measurements of the same ROI in confocal and wide-field mode. To guarantee reproducible single molecule samples, a simple immobilization method was utilized, allowing to attach different dye bioconjugates (e.g. antibodies, nanobodies, self-labeling enzymes) to a polymer layer via various intermediates (e.g. streptavidin, biotin,  $\text{Ni}^{2+}$ /NTA) [49, 50]. A sparse distribution of fluorophores ensured the investigation at the single molecule level, which enabled the observation of the emitters switching individually. By applying a comprehensive analysis of a large set of data, a detailed characterization of the fluorophore properties was performed with statistical relevance, including photophysical properties like photons per on-cycle and emission rate, as well as switching related properties like activation rate (for irreversible mechanism), on-time, duty cycle or number of on-cycles (for reversible mechanisms). After evaluating these properties, the fluorophores were tested in biological samples, utilizing different bioconjugates in fixed and living cells. With the aid of the custom-built setup confocal as well as PALM/STORM data were acquired, proving the specificity of the reactive adducts and bioconjugates. Furthermore, their cell permeability and the applicability for live-cells measurements was proven by staining nuclear pore complexes (NPC) and vimentin with a chloralkane ligand selective for the self labeling enzyme HaloTag. Finally, dyes were selected on basis of the obtained results and applied in MINFLUX nanoscopy. As NPCs are an established standardized system in optical nanoscopy [52], proteins of the NPCs were stained in genetically modified cells via HaloTag and anti-GFP-nanobodies. The small size (33 kDa and 43 kDa respectively) of these state-of-the-art labels, complies with the high localization precision of MINFLUX nanoscopy. MINFLUX data were mostly obtained on a commercial MINFLUX setup (Abberior GmbH, Göttingen) and, for specific experiments, on a custom-built setup [71, 72]. A statistical analysis of the initial data allowed for a refinement of the measurement routines with respect to the fluorophore properties. Subsequently, final data were acquired, evaluated and compared to previous publications [8, 9, 52].

With the aid of the established characterization strategy, two different dye classes were investigated and implemented in MINFLUX possessing different switching mechanisms. The first mechanism investigated, relies on reversible and stochastic switching in the fluorophores' ground state between a thermodynamically stable dark off-state and a short-lived ( $< 10$  ms) fluorescent on-state (chapter 3). Their average on-times of  $T_{On} \leq 3$  ms are more than one order of magnitude shorter than the ones previously reported stochastically switching dyes [21], fitting the fast localization speed of a single MINFLUX position estimate ( $T_{1,loc} \approx 1$  ms). By iterative adaption of the MINFLUX routine it was possible to localize single emitters of stained NPCs with on average  $T_{1,loc} \approx 1.5$  ms resulting in an average localization time per photon burst of  $T_{loc} \approx 9$  ms. This is a 30-fold increase of imaging speed compared to previous reports on MINFLUX imaging with dyes featuring photo-induced blinking, while losing only a factor of 4 in precision [9]. The difference in localization precision is attributed to the scanning range  $L$ , which was increased by a factor of 2.5 in the adapted measurement routine. However, the obtained localization precision of  $\sigma = 3.7$  nm is of the size of the state of the art labels (e.g. nanobodies, HaloTag) employed in nanoscopy techniques. As the mechanism is controlled chemically, tweaking the switching properties can be achieved by further changing of the side groups or changing the pH-value (in fixed samples only). This would allow for adjusting the switching properties to the DOL of the structure of interest or optimize the localization efficiency further in terms of speed and success.

The second switching mechanism investigated, is based on irreversible on-switching and subsequent off-switching by photo-degradation after obtaining the spatial information from a single photon burst (chapter 4). The characterized photoactivatable xanthone (PAX) dyes [34], performed cage-group free on-switching with a high activation rate. The selected dyes reliably performed fluorescent switching for MINFLUX nanoscopy, providing an apparent density of labeling (ADOL) of NPCs comparable to the one measured with PALM imaging, and also in line with previous publications evaluating other established dye mechanisms including reversible ones (e.g. cyanines) [52]. To the best of our knowledge, this is the first quantitative analysis comparing the detection ratio of MINFLUX nanoscopy to an established SMLM method, proving a similar localization efficiency in terms of success. Moreover, the dyes' irreversible switching behavior was exploited to resolve one dimension of a single fluorescent affinity label (nanobody) unambiguously, by sequentially localizing two PAX fluorophores attached to the N- and C-terminus of the nanobody. The measured distance was  $d = 6.21$  nm, well fitting the expected size of a nanobody (from x-ray structures) plus terminal linkers of five to six amino acids. A recent study using expansion microscopy determined a distance  $d \approx 6$  nm for a similar nanobody construct [73], being in good agreement with our results. Resolving single nanobodies reveals a new barrier in fluorescence microscopy, as the method now offers a resolution,

---

at which the distance between the fluorophore and the structure of interest is no longer negligible. Therefore, future research interest will lie on the identification and development of even smaller labels or will push endogenous labeling with fluorescent proteins suitable for MINFLUX with the aid of CRISPR/Cas more into the spotlight. Finally, the dyes' applicability in dual color imaging was demonstrated by combining two PAX compounds with separated emission spectra and staining the inner and outer ring of NPCs. The two rings were identified by color separation and these results were reproduced by sequential separation exploiting different activation rates of the dyes. The combination of dyes with different activation rates or even orthogonal switching mechanisms promise to allow for combining simultaneous and sequential multicolor imaging in the same spectral range.

As stated above, the localization efficiency mainly depends on the interplay of the measurement scheme and the photoswitching behavior of the fluorophore. To take full consideration of different dye characteristics, tuning of the localization schemes with respect to the dye properties will be required, potentially resulting in different schemes adapted to each dye and experiment. To this end, a self-adapting measurement scheme could be introduced, automatically choosing the  $L$ , number of MINFLUX iterations and other important measurement parameters based on the current fluorophore performance, instead of performing MINFLUX steps with a fixed  $L$ . This machine-based decision making could accelerate single localizations for dyes with short on-times by significantly reducing the number of exposures.

In conclusion, it has been demonstrated that both a spontaneously blinking as well as an irreversible switching mechanism are suitable for MINFLUX imaging. In contrast to previously employed dyes, the investigated mechanisms uncouple the control over the single fluorophore discriminability from the localization routine, which enables the experimenter to influence both independently with respect to the individual experiment. Selecting photoswitching mechanisms based on their strength with respect to the individual experiment, tweaking switching parameters and exploiting orthogonal switching opens the door to a manifold of new applications conceivable in MINFLUX nanoscopy.

# Chapter 7

## Supplementary Information

### 7.1 Commercial MINFLUX microscopic setup

MINFLUX imaging was performed on a commercial Abberior 3D MINFLUX microscope. For excitation, the setup is equipped with a 560 nm and a 640 nm (CW) excitation laser line. Moreover, for confocal imaging the setup possesses a 488 nm laser line, as well as a 405 laser line for activation. The latter can be dimmed by neutral density filters, which was utilized for the PAX dyes. The three detection channels range from 580 – 630 nm ( $Cy_3$ ), 650 – 685 nm ( $Cy_{5, near}$ ) 685 – 720 nm ( $Cy_{5, far}$ ). Active stabilization of the system is achieved with a real-time positioning system containing a infrared laser (975 nm) and wide-field camera collecting scattered infrared light from the sample plane.

**Reversible On-Switching Dyes** Spontaneously blinking fluorophores were excited at 640 nm and detected with  $Cy_5$  near and  $Cy_5$  far channel adding up the signal. The excitation powers ranged from 240 – 540  $\mu$ W measured at the scanner entry. Different sequences were utilized to take the characteristics of the dyes into account. The main parameters of the respective sequence are listed in table 7.1.

**Irreversible On-Switching Dyes** PAX dyes were excited at 560 nm and detected in the  $Cy_3$  channel. For dual color images the  $Cy_{5, near}$  also recorded. Excitation power in the last MINFLUX iteration ranged from 180 – 360  $\mu$ W at the scanner entry. For imaging an adaption of a standard sequence was utilized listed in table 7.2. For mMaple a modified sequence kindly provided from the EMBL Imaging Center was used.

Table 7.1: **Main parameters of the MINFLUX imaging sequence.**  $L$  is the exposure distance of the MINFLUX localization pattern. Center frequency ratio (cfr) is the ratio of photons between the inside and outside exposures. The dwell time (Dt) is the minimal time of one step (all exposures of the hexagonal illumination scheme) to surpass the photon threshold (Thr). Pattern repeat is the number of repeats of the hexagonal illumination scheme inside one dwell time. The power factor (PF) defines the power of the exposure by multiplying the factor with the base excitation power.

	<b>Spontaneously blinking dyes - Slow Sequence</b>						
	$L$ (nm)	Thr (phot)	cfr	Dt (ms)	offset BG (kHz)	PF	Pattern repeat
<b>step 1 (gauss)</b>	288	30	2	1	10000	1	1
<b>step 2 (donut)</b>	288	30	0.5	1	8000	1	1
<b>step 3 (donut)</b>	151	30	2	1	8000	2	1
<b>step 4 (donut)</b>	101	30	0.8	1	8000	4	1
<b>step 5 (donut)</b>	76	30	0.8	1	8000	4	1
<b>step 6 (donut)</b>	40	30	0.8	1	8000	6	1

	<b>Spontaneously Blinking dyes - Fast Sequence</b>						
	$L$ (nm)	Thr (phot)	cfr	Dt (ms)	offset BG (kHz)	PF	Pattern repeat
<b>step 1 (gauss)</b>	288	20	1	0.4	15000	2	1
<b>step 2 (donut)</b>	151	30	0.8	0.3	10000	2	1
<b>step 3 (donut)</b>	76	30	0.8	0.5	30000	4	1

## 7.2 Custom-built MINFLUX microscopic setup

In the custom-built MINFLUX microscopic setup a 405 nm laser (LBX-405-100, Oxxius, Lannion, France) is overlaid with the excitation beam ( $\lambda = 561$  nm, Jive Cobolt 05-01 Series, Hübner, Kassel Germany) and focused into the sample. The MINFLUX iteration is performed by moving two pairs of beams, interfering destructively in the focal plane and yielding an intensity zero, over the emitter of interest. The measurement routine is controlled via a dedicated self-written LabView software. Raw MINFLUX position data were reevaluated using

$$x_M = \frac{L}{4} \frac{(n_- - n_+)}{n_- + n_+ - 2n_0} + x_{FPGA} \quad , \quad (7.1)$$

with  $x_{FPGA}$  being the coordinate of the central exposure and  $n$  the number of photons at the respective position  $(x_0 - L/2, x_0 + L/2, x_0)$ . To prevent large outliers the new position only counts valid if  $|n_- - n_+| < 4(n_- + n_+ - 2n_0)$ . Otherwise the last position estimate was kept. Pre-selected traces possessing two time-wise distinguishable events were used for further evaluation.

Table 7.2: **Main parameters of the MINFLUX imaging sequence.**  $L$  is the exposure distance of the MINFLUX localization pattern. Center frequency ratio (cfr) is the ratio of photons between the inside and outside exposures (cfr=  $-1$  meaning filter off). The dwell time (Dt) is the minimal time of one step (all exposures of the hexagonal illumination scheme) to surpass the photon threshold (Thr). Pattern repeat is the number of repeats of the hexagonal illumination scheme inside one dwell time. The power factor (PF) defines the power of the exposure by multiplying the factor with the base excitation power. Additionally for mMaple the max-off time (waiting time before aborting the sequence if the the signal went below the internal photon threshold) was set to 20 ms to take short term blinking into account.

	PAX fluorophores - Sequence						
	$L$ (nm)	Thr (phot)	cfr	Dt (ms)	offset BG (kHz)	PF	Pattern repeat
step 1 (gauss)	288	30	2	1	10000	1	1
step 2 (donut)	288	30	0.5	1	8000	1	1
step 3 (donut)	151	30	2	1	8000	2	1
step 4 (donut)	101	30	0.8	1	8000	4	1
step 5 (donut)	76	30	0.8	1	8000	4	1
step 6 (donut)	40	30	0.8	1	8000	6	1
	mMaple - Sequence						
	$L$ (nm)	Thr (phot)	cfr	Dt (ms)	offset BG (kHz)	PF	Pattern repeat
step 1 (gauss)	273	20	-1	2	20000	1	1
step 2 (donut)	302	30	0.6	2	15000	1	5
step 3 (donut)	101	80	0.8	2	15000	2.5	5

### 7.3 Initial PALM data analysis for evaluating the apparent density of labeling

The acquired camera frames were converted to localizations with a dedicated script written in Matlab. The script first subtracts an inhomogeneous background (by a convolution of the camera frames with a Gaussian convolution kernel and suitable size in x and y as well as extending over a few consecutive frames. The width of the PSF was estimated from fitting a few selected peaks in the data (FWHM was 2.8 camera pixel). Localizations were obtained by fitting a single Gaussian peak with the estimated FWHM to each local maxima to the background subtracted data with a brightness above a certain threshold. In a first post-processing step, localizations within the first 100 frames (too many molecules were in the on-state), with a too large fit chi-square or too low fit amplitude were discarded ( $\approx 20\%$  of localizations were discarded in that step). Localizations in consecutive frames with overlapping fits were combined. A drift correction was applied that divided the dataset in overlapping small time windows and calculated redundant cross-correlations between the data subsets, then computing a shift between these datasets that minimizes

the shift in the position of the maximum of the cross-correlations, finally interpolating linearly between the time points of the data subsets. Moreover, a density based filter was applied, by choosing the lowest density of localizations within a  $50 \cdot 50 \text{ nm}^2$  area as a threshold where still most localizations in between the NPCs structures can be filtered out. The remaining localizations are used for display and for calculation of the labeling efficiency.

## 7.4 Labeling Protocols

Labeling was performed according by the protocols listed below. The protocol for nanobody labeling of nuclear pore complexes is an adaption from the one provided by the protein provider (NanoTag Biotechnologies) and adapted. The protocol for labeling nuclear pore complexes of HK-2xZFN-mEGFP-Nup107 cells with anti-GFP nanobodies was first introduced by Pleiner et al. [51]. Labeling with primary antibodies was also performed overnight at 4°C. Moreover, the buffers used are listed in table 7.8.

Table 7.3: **Protocol for live-cell labeling of vimentin and nuclear pore complex and counter labeling with primary and secondary antibodies.** For live-cell labeling only the protocol was stopped before blocking the cells.

Steps	Concentration	Duration
Labeling with dye of interest in cell media	(200-500) nM	(24-48) h
(2x) Wash with cell media		45 min
Wash with PBS		30 s
Fix with PFA at r.t.	3%	15 min
Incubate with quenching buffer		10 min
Incubate with permeabilization buffer	0.1%-0.2%	5 min
(2x) Wash with PBS		5 min
Incubate with blocking buffer (BB)	2 %	45 min
Incubate with primary antibody in BB	1:200-1:400	60 min
(2x) Wash with BB	2%	5 min
Incubate with secondary antibody or nanobody in BB	1:1000-1:4000	60 min
Wash with BB	2%	5 min
(2x) Wash with PBS		5 min

Table 7.4: **Protocol for labeling nuclear pore complexes of eGFP cells with anti-GFP nanobodies.**

Steps	Concentration	Duration
Fix with PFA in transport buffer (TRB) at r.t.	2.4%	30 s
(2x) Wash with TRB		5 min
Incubate with Digitonin in TRB on ice	25 µg/ml	8 min
(2x) Wash with transport blocking buffer (TBA)	1%	5 min
Incubate with anti-GFP nanobody in TBA	1:4000	60 min
(2x) Wash with TBA	1%	5 min
Fix with PFA in TBA at r.t.	3%	10 min
(2x) Wash with TBA	1%	5 min
Incubate with permeabilization buffer	0.1%-0.2%	3 min
(2x) Wash with PBS		5 min
Incubate with anti-GFP nanobody in TBA	1:4000	60 min
Wash with TBA	1%	5 min
(2x) Wash with PBS		5 min

Table 7.5: **Protocol for labeling nuclear pore complexes with primary and secondary antibodies.**

Steps	Concentration	Duration
Fix with PFA at r.t.	3%	15 s
Wash with PBS		30 s
Incubate with quenching buffer		10 min
Wash with PBS		5 s
Incubate with permeabilization buffer	0.1%-0.2%	5 min
Incubate with blocking buffer (BB)	2 %	45 min
Incubate with primary antibody in BB	1:200-1:400	60 min
(2x) Wash with BB	2%	5 min
Incubate with secondary antibody or nanobody in BB	1:1000-1:4000	60 min
Wash with BB	2%	5 min
(2x) Wash with PBS		5 min

Table 7.6: **Protocol for labeling vimentin or tubulin with primary and secondary antibodies.**

Steps	Concentration	Duration
Fix with MeOH cooled to -20°C		5 min
Wash with PBS		5 s
Incubate with permeabilization buffer	0.1%-0.2%	5 min
Incubate with blocking buffer (BB)	2 %	45 min
Incubate with primary antibody in BB	1:200-1:400	60 min
(2x) Wash with BB	2%	5 min
Incubate with secondary antibody or nanobody in BB	1:1000-4000	60 min
Wash with BB	2%	5 min
(2x) Wash with PBS		5 min

Table 7.7: Fixation protocol for U2OS-CRISPR-NUP96-mMaple clone #16 cells.

Steps	Concentration	Duration
Fix with PFA at r.t.	2.4%	30 s
Incubate with permeabilization buffer	(0.1-0.2)%	3 min
Fix with PFA in TBA at r.t.	2.4%	30 min
Incubate with quenching buffer		10 min
(2x) Wash with PBS		5 min
Mounting in Tris buffer (pH= 8) in 95% D <sub>2</sub> O	50 mM	

Table 7.8: Buffers utilized in the context of this thesis.

Buffer/Medium	Reagents
PBS	Phosphate buffered saline tablets (18912-014 Gibco)
Blocking buffer	BSA in PBS (2%, BP9702, Fisher Scientific)
Quenching buffer	Glycine (0.1 M), Ammonium chloride (0.1 M)
Transport buffer	HEPES (20 mM, pH 7.5), Potassiumacetat (KAc, 110mM, 32309-500G, Roth) EGTA (1mM, E3889-10G, Roth), Sucrose (250mM, S0389-1kg, Sigma)
Transport blocking buffer	Transport buffer with BSA (1%)
Permeabilization buffer	Triton (0.1-0.2%, VWR) in PBS
Dulbeccos's modified eagle medium ++ (DMEM++)	FBS (10% v/v, 10500064, ThermoFisher), penicillin-streptomycin (1%, 15140122, Gibco) 2mM GlutaMAX (35050061, ThermoFischer)
McCoy's 5A medium ++ (2600023, Gibco)	1mM sodium pyruvate (ThermoFisher 31966), 1-10% MEM (11140035, ThermoFischer) FBS (10% v/v, 10500064, ThermoFisher), penicillin-streptomycin (1%, 15140122, Gibco)
FluoBrite DMEM ++ (A1896701, ThermoFisher)	GlutaMAX (2%), FBS 10% v/v (10500064, ThermoFisher)

Table 7.9: Buffers utilized in the context of this thesis.

Cell line	Distributor
HK-2xZFN-mEGFP-Nup107	CLS Cell Lines Service GmbH (300676)
U2OS-CRISPR-NUP96-mMaple clone #16	CLS Cell Lines Service GmbH (300461)
U2OS-NUP96-Halo	CLS Cell Lines Service GmbH (300448)
COS-7	CLS Cell Lines Service GmbH (665470)
U2OS-Vim-Halo	Jakobs Group, Structure & Dynamics of Mitochondria, MPI Göttingen

## 7.5 Reagents and Proteins

The following tables list the proteins and additives used in this work for single molecule characterization, cell labeling and imaging. Reagents and proteins used for single molecule characterization are listed in table 7.10. Reagents, proteins and labels used for imaging are listed in table 7.11

Table 7.10: **Proteins and additives used for single molecule characterization experiments.**

Reagent	Type	Supplier	Catalogue No.	Concentration
PLL-PEG-biotin (PLL(20)-g[3.5]-PEG(2)/PEG(3.4)-biotin(20%))	Polymer-Protein Layer	Suso AG Inc.		0.2mg/ml
PLL-PEG-biotin (PLL(20)-g[3.5]-PEG(3.4)-NTA, biotin(20%))	Polymer-Protein Layer	Suso AG Inc.		0.2mg/ml
Streptavidin	Protein	Merck/Sigma Aldrich	189730	10 $\mu$ g/ml
NiCl <sub>2</sub>	Additive	Merck/Sigma Aldrich	339350	2 $\mu$ g/ml
his-HaloTag7	Protein	Protein Expressison Facility MPIMR		1:10000/1:100000
AffiniPure Goat Anti-Rabbit IgG (H+L)	Secondary antibody (goat, anti-rabbit)	Jackson ImmunoResearch Europe Ltd	111-005-003	1:100
chloroalkane dye adduct	Reactive dye	prepared in the respective projects		100 pM - 10 nM
Biotin-SP (long spacer) Rabbit Anti-Mouse IgG (H+L)	Secondary antibody (rabbit, anti-mouse)	AffiniPure Jackson ImmunoResearch Europe Ltd	315-065-045	1:100

Table 7.11: **Antibodies and nanobodies used for labeling and imaging.**

Reagent	Type	Target	Host	Supplier	Catalogue No.	Dilution
$\alpha$ -Anti-Tubulin antibody	Primary Antibody (monoclonal)	$\alpha$ -tubulin	Rabbit	Abcam	ab18251	1:200
Anti-Nup153 antibody	Primary Antibody (monoclonal)	Nup153	Mouse	Abcam	ab24700	1:300
FluoTag-X2 anti-GFP unconjugated clone 1H1 & 1B2	Nanobody	GFP	Camelid	NanoTag Biotechnologies	N0302	1:4000
FluoTag-X2 anti-rabbit unconjugated clone 10E10	Nanobody	Rabbit	Alpaca	NanoTag Biotechnologies	N2402	1:2000
Invitrogen Goat Anti-Mouse IgG (H+L)	Secondary antibody	Mouse	Goat	Thermo Fisher	A32723	1:1000
NUP98 (C39A3) mAb	Primary antibody	Nup98	rabbit	Cell Signal	2598	1:100
AffiniPure Goat Anti-Rabbit IgG (H+L)	Secondary antibody	Rabbit	Goat	Jackson ImmunoResearch	111-005-003	1:100
chloroalkane dye adduct	Reactive dye	HaloTag		prepared in the respective project		100 nM - 500 nM



# List of Tables

2.1	Overview of dichroics in filter cascade . . . . .	24
2.2	Overview of filter cubes inside the microscope body . . . . .	25
3.1	Photophysical properties of the fluorescent probes . . . . .	42
3.2	Photophysical properties of compound 4 bound to different ligands . . . . .	42
3.3	Image parameters obtained from the MINFLUX measurements compared with Schmidt et al. [9] . . . . .	51
4.1	Photophysical properties of the fluorescent probes . . . . .	57
4.2	Image parameters obtained from the respective PALM measurements . . . . .	60
4.3	Image parameters obtained from the respective MINFLUX measurements. . . . .	64
7.1	Main parameters of the MINFLUX imaging sequence. . . . .	83
7.2	Main parameters of the MINFLUX imaging sequence. . . . .	84
7.3	Protocol for live-cell labeling of vimentin and nuclear pore complex and counter labeling with primary and secondary antibodies. . . . .	85
7.4	Protocol for labeling nuclear pore complexes of HK-2xZFN-mEGFP-Nup107 cells with anti-GFP nanobodies. . . . .	86
7.5	Protocol for labeling nuclear pore complexes with primary and secondary antibodies. . . . .	86
7.6	Protocol for labeling vimentin or tubulin with primary and secondary antibodies. . . . .	86
7.7	Fixation protocol for U2OS-CRISPR-NUP96-mMaple clone #16 cells. . . . .	87
7.8	Buffers and cell media utilized in the context of this thesis. . . . .	87
7.9	Buffers and cell media utilized in the context of this thesis. . . . .	87
7.10	Proteins and additives used for single molecule characterization experiments. . . . .	88
7.11	Antibodies and nanobodies used for labeling and imaging. . . . .	88

# List of Figures

1.1	Molecular orbitals and electronic energy states of formaldehyde. . . . .	5
1.2	Perrin-Jablonski diagram of the energy states and transitions of a molecule. . . . .	7
1.3	Simplified Jablonski diagram of the triplet state transitions. . . . .	8
1.4	Main photochemical/photophysical processes of Cy5. . . . .	10
1.5	Spontaneous reversible on/off-switching of fluorophores. . . . .	11
1.6	Irreversible on-switching of fluorophores. . . . .	12
1.7	MINFLUX excitation scheme visualized in 1D. . . . .	16
1.8	MINFLUX localization precision in dependence on number of detected photons. . . . .	17
1.9	Iterative MINFLUX approach. . . . .	18
1.10	Single fluorophore event probability in dependence on the duty cycle. . . . .	19
1.11	Probability distribution of detected events for an idealized nuclear pore complex. . . . .	20
2.1	Scheme of the custom-built experimental setup . . . . .	23
2.2	Data separation of the single molecule time traces. . . . .	27
2.3	Evaluation of the single molecule data. . . . .	28
2.4	Visualization of DBSCAN. . . . .	30
2.5	Outlier filtering method. . . . .	31
2.6	Single Molecule Sample Setup. . . . .	32
3.1	General structure of the evaluated stochastic blinkers. . . . .	37
3.2	Absorbance of the six compounds in dependence on the pH-values. . . . .	38
3.3	Duration distribution of the on-events for the six compounds. . . . .	39
3.4	Duration distribution of the off-events for the six compounds. . . . .	40
3.5	On- and off-times of the six compounds and the corresponding duty cycle in dependence on the equilibrium constant. . . . .	41
3.6	Experimental complementary cumulative distribution function of compound 4 with different bioconjugates. . . . .	43
3.7	Reconstructed STORM images of fixed tubulin. . . . .	44
3.8	Reconstructed STORM images of live-cell vimentin. . . . .	45
3.9	Reconstructed STORM images of nuclear pore complexes. . . . .	46
3.10	MINFLUX images of nuclear pore complexes. . . . .	47
3.11	mEGFP-Nup107 cells imaged with different MINFLUX sequences. . . . .	48
3.12	Localization precision in dependence on binning and filtering. . . . .	50
4.1	Absorption spectra of the open (non-fluorescent) and closed (fluorescent) form. . . . .	54
4.2	PAX compounds utilized in this work. . . . .	55
4.3	Histograms of the event duration ( $T_{On}$ ) for PAX <sub>560</sub> and PAX <sub>+560</sub> at three different excitation intensities. . . . .	56
4.4	Activation rate in dependence on activation power. . . . .	58
4.5	Reconstructed PALM images of fixed tubulin. . . . .	59
4.6	Reconstructed PALM images of vimentin in live-cells. . . . .	60

4.7	Two-color PALM image of tubulin and clathrin-coated pits stained with PAX <sub>560</sub> and PAX <sub>480</sub> . . . . .	61
4.8	Reconstructed PALM images of nuclear pore complexes. . . . .	62
4.9	MINFLUX images of nuclear pore complexes. . . . .	63
4.10	Visualization of the algorithm utilized for occupancy analysis of MINFLUX data. . . . .	66
4.11	Visualization of the algorithm utilized for occupancy analysis of PALM data. . . . .	67
4.12	Histograms with apparent density of labeling. . . . .	68
5.1	Exemplary localization clusters representing a double labeled nanobody. . . . .	71
5.2	Localizations projected into a single dimension. . . . .	72
5.3	Dual color MINFLUX imaging with PAX dyes. . . . .	74
5.4	Filtered events discriminated by dual color ratio (DCR). . . . .	74
5.5	Excerpt of the reconstructed MINFLUX image (see figure 5.4B) . . . . .	75
5.6	Radial distribution of the signal after averaging the NPCs. . . . .	76

# Publications

**M. Rimmel**, L. Scheiderer, A.N. Butkevich, M.L. Bossi, S. W. Hell. Spontaneously blinking fluorophores for accelerated MINFLUX nanoscopy. 2022, submitted (available as preprint on *bioRxiv*)

**M. Rimmel**, R.Lincoln, M. Weber, A.N. Butkevich, M.L. Bossi, J. Matthias, S.W. Hell. PAX PNAS (in preparation)

**R. Lincoln**, **M.L. Bossi**, M. Rimmel, E. D'Este, A.N. Butkevich, S.W. Hell. A general design of caging-group-free photoactivatable fluorophores for live-cell nanoscopy. 2022, Nature Chemistry

# Bibliography

- [1] E. Abbe. Beiträge zur theorie des mikroskops und der mikroskopischen wahrnehmung. *Archiv für Mikroskopische Anatomie*, 9(1):413–468, 1873.
- [2] Stefan W. Hell and Jan Wichmann. Breaking the diffraction resolution limit by stimulated emission: stimulated-emission-depletion fluorescence microscopy. *Opt. Lett.*, 19(11):780–782, 1994.
- [3] Thomas A. Klar, Egbert Engel, and Stefan W. Hell. Breaking abbe’s diffraction resolution limit in fluorescence microscopy with stimulated emission depletion beams of various shapes. *Phys. Rev. E*, 64:066613, 2001.
- [4] Michael J. Rust, Mark Bates, and Xiaowei Zhuang. Sub-diffraction-limit imaging by stochastic optical reconstruction microscopy STORM. *Nature Methods*, 3(10):793–796, 2006.
- [5] Eric Betzig, George H. Patterson, Rachid Sougrat, O. Wolf Lindwasser, Scott Olenych, Juan S. Bonifacino, Michael W. Davidson, Jennifer Lippincott-Schwartz, and Harald F. Hess. Imaging intracellular fluorescent proteins at nanometer resolution. *Science*, 313(5793):1642–1645, 2006.
- [6] S. T. Hess, T. P. Girirajan, and M. D. Mason. Ultra-high resolution imaging by fluorescence photoactivation localization microscopy. *Biophys J*, 91(11):4258–72, 2006.
- [7] Francisco Balzarotti, Yvan Eilers, Klaus C Gwosch, Arvid H Gynnå, Volker Westphal, Fernando D Stefani, Johan Elf, and Stefan W Hell. Nanometer resolution imaging and tracking of fluorescent molecules with minimal photon fluxes. *Science*, 355:606–612, 2017.
- [8] Klaus C. Gwosch, Jasmin K. Pape, Francisco Balzarotti, Philipp Hoess, Jan Ellenberg, Jonas Ries, and Stefan W. Hell. MINFLUX nanoscopy delivers 3d multicolor nanometer resolution in cells. *Nature Methods*, 17(2):217–224, 2020.
- [9] Roman Schmidt, Tobias Weihs, Christian A. Wurm, Isabelle Jansen, Jasmin Rehman, Steffen J. Sahl, and Stefan W. Hell. MINFLUX nanometer-scale 3d imaging and microsecond-range tracking on a common fluorescence microscope. *Nature Communications*, 12(1):1478, 2021.
- [10] Valeur & Berberan-Santos. *Absorption of Ultraviolet, Visible, and Near-Infrared Radiation*, chapter 2, pages 31–51. John Wiley & Sons, Ltd, 2012.
- [11] Valeur & Berberan-Santos. *Characteristics of Fluorescence Emission*, chapter 3, pages 53–74. John Wiley & Sons, Ltd, 2012.
- [12] N. K. Bridge, George Porter, and Ronald George Wreyford Norrish. Primary photoprocesses in quinones and dyes i. spectroscopic detection of intermediates. *Proceedings of the Royal Society of London. Series A. Mathematical and Physical Sciences*, 244(1237):259–275, 1958.

- [13] Alexander P Demchenko. Photobleaching of organic fluorophores: quantitative characterization, mechanisms, protection. *Methods and Applications in Fluorescence*, 8(2):022001, 2020.
- [14] Rob Zondervan, Florian Kulzer, Mikhail A. Kol’chenk, and Michel Orrit. Photobleaching of rhodamine 6g in poly(vinyl alcohol) at the ensemble and single-molecule levels. *The Journal of Physical Chemistry A*, 108(10):1657–1665, 2004. doi: 10.1021/jp037222e.
- [15] Babette Hinkeldey, Alexander Schmitt, and Gregor Jung. Comparative photostability studies of bodipy and fluorescein dyes by using fluorescence correlation spectroscopy. *ChemPhysChem*, 9(14):2019–2027, 2008.
- [16] Owen Woodford, Anthony Harriman, William McFarlane, and Corinne Wills. Dramatic effect of solvent on the rate of photobleaching of organic pyrrole-bf2 (bophy) dyes. *ChemPhotoChem*, 1(7):317–325, 2017.
- [17] C. Eggeling, J. Widengren, R. Rigler, and C. A. M. Seidel. Photobleaching of fluorescent dyes under conditions used for single-molecule detection: Evidence of two-step photolysis. *Analytical Chemistry*, 70(13):2651–2659, 1998.
- [18] Jan Vogelsang, Robert Kasper, Christian Steinhauer, Britta Person, Mike Heilemann, Markus Sauer, and Philip Tinnefeld. A reducing and oxidizing system minimizes photobleaching and blinking of fluorescent dyes. *Angewandte Chemie International Edition*, 47(29):5465–5469, 2008.
- [19] Viktorija Glembockyte and Gonzalo Cosa. Redox-based photostabilizing agents in fluorescence imaging: The hidden role of intersystem crossing in geminate radical ion pairs. *Journal of the American Chemical Society*, 139(37):13227–13233, 2017. doi: 10.1021/jacs.7b08134.
- [20] Michael Hofmann, Christian Eggeling, Stefan Jakobs, and Stefan W. Hell. Breaking the diffraction barrier in fluorescence microscopy at low light intensities by using reversibly photoswitchable proteins. *Proceedings of the National Academy of Sciences*, 102(49):17565–17569, 2005.
- [21] Shin-nosuke Uno, Mako Kamiya, Toshitada Yoshihara, Ko Sugawara, Kohki Okabe, Mehmet C. Tarhan, Hiroyuki Fujita, Takashi Funatsu, Yasushi Okada, Seiji Tobita, and Yasuteru Urano. A spontaneously blinking fluorophore based on intramolecular spirocyclization for live-cell super-resolution imaging. *Nature Chemistry*, 6(8):681–689, 2014.
- [22] Atanu Acharya, Alexey M. Bogdanov, Bella L. Grigorenko, Ksenia B. Bravaya, Alexander V. Nemukhin, Konstantin A. Lukyanov, and Anna I. Krylov. Photoinduced chemistry in fluorescent proteins: Curse or blessing? *Chemical Reviews*, 117(2):758–795, 2017. doi: 10.1021/acs.chemrev.6b00238.
- [23] Yasser Gidi, Liam Payne, Viktorija Glembockyte, Megan S. Michie, Martin J. Schnermann, and Gonzalo Cosa. Unifying mechanism for thiol-induced photoswitching and photostability of cyanine dyes. *Journal of the American Chemical Society*, 142(29):12681–12689, 2020. PMID: 32594743.
- [24] Sebastian van de Linde, Ivan Krstić, Thomas Prisner, Sören Doose, Mike Heilemann, and Markus Sauer. Photoinduced formation of reversible dye radicals and their impact on super-resolution imaging. *Photochem. Photobiol. Sci.*, 10:499–506, 2011.

- [25] Sebastian Van De Linde, Ivan Krstić, Thomas Prisner, Sören Doose, Mike Heilemann, and Markus Sauer. Photoinduced formation of reversible dye radicals and their impact on super-resolution imaging. *Photochemical and Photobiological Sciences*, 10:499–506, 2011.
- [26] I. Jusuk, C. Vietz, M. Raab, T. Dammeyer, and P. Tinnefeld. Super-resolution imaging conditions for enhanced yellow fluorescent protein (eyfp) demonstrated on dna origami nanorulers. *Sci Rep*, 5:14075, 2015.
- [27] Tanja Brakemann, Andre C. Stiel, Gert Weber, Martin Andresen, Ilaria Testa, Tim Grotjohann, Marcel Leutenegger, Uwe Plessmann, Henning Urlaub, Christian Eggeling, Markus C. Wahl, Stefan W. Hell, and Stefan Jakobs. A reversibly photoswitchable gfp-like protein with fluorescence excitation decoupled from switching. *Nature Biotechnology*, 29(10):942–947, 2011.
- [28] Akihiko Morozumi, Mako Kamiya, Shin-nosuke Uno, Keitaro Umezawa, Ryosuke Kojima, Toshitada Yoshihara, Seiji Tobita, and Yasuteru Urano. Spontaneously blinking fluorophores based on nucleophilic addition/dissociation of intracellular glutathione for live-cell super-resolution imaging. *Journal of the American Chemical Society*, 142(21):9625–9633, 2020. doi: 10.1021/jacs.0c00451.
- [29] B. Albert Griffin, Stephen R. Adams, and Roger Y. Tsien. Specific covalent labeling of recombinant protein molecules inside live cells. *Science*, 281(5374):269–272, 1998.
- [30] Shin-nosuke Uno, Mako Kamiya, Akihiko Morozumi, and Yasuteru Urano. A green-light-emitting, spontaneously blinking fluorophore based on intramolecular spirocyclization for dual-colour super-resolution imaging". *Chem. Commun.*, 54:102–105, 2018.
- [31] Samuel J. Lord, Nicholas R. Conley, Hsiao-lu D. Lee, Reichel Samuel, Na Liu, Robert J. Twieg, and W. E. Moerner. A photoactivatable push-pull fluorophore for single-molecule imaging in live-cells. *Journal of the American Chemical Society*, 130(29):9204–9205, 2008. doi: 10.1021/ja802883k.
- [32] Vladimir. N Belov, Christian A. Wurm, Vadim P. Boyarskiy, Stefan Jakobs, and Stefan W. Hell. Rhodamines nn: A novel class of cages fluorescent dyes. *Angewandte Chemie International Edition*, 49(20):3520–3523, 2010.
- [33] Jonathan B. Grimm, Brian P. English, Heejun Choi, Anand K. Muthusamy, Brian P. Mehl, Peng Dong, Timothy A. Brown, Jennifer Lippincott-Schwartz, Zhe Liu, Timothée Lionnet, and Luke D. Lavis. Bright photoactivatable fluorophores for single-molecule imaging. *Nature Methods*, 13(12):985–988, 2016.
- [34] Richard Lincoln, Mariano L. Bossi, Michael Remmel, Elisa D’Este, Alexey N. Butkevich, and Stefan W. Hell. A general design of caging-group-free photoactivatable fluorophores for live-cell nanoscopy. *Nature Chemistry*, 2022.
- [35] Ann L. McEvoy, Hiofan Hoi, Mark Bates, Evgenia Platonova, Paula J. Cranfill, Michelle A. Baird, Michael W. Davidson, Helge Ewers, Jan Liphardt, and Robert E. Campbell. mmapple: A photoconvertible fluorescent protein for use in multiple imaging modalities. *PLOS ONE*, 7(12):1–15, 2012.
- [36] S. A. McKinney, C. S. Murphy, K. L. Hazelwood, M. W. Davidson, and L. L. Looger. A bright and photostable photoconvertible fluorescent protein. *Nat Methods*, 6(2):131–3, 2009.
- [37] Stefan W. Hell. Far-field optical nanoscopy. *Science*, 316(5828):1153–1158, 2007.

- [38] S. W. Hell and M. Kroug. Ground-state-depletion fluorescence microscopy: A concept for breaking the diffraction resolution limit. *Applied Physics B*, 60(5):495–497, 1995.
- [39] Benjamin Harke, Jan Keller, Chaitanya K. Ullal, Volker Westphal, Andreas Schönle, and Stefan W. Hell. Resolution scaling in STED microscopy. *Opt. Express*, 16(6):4154–4162, 2008.
- [40] E. Rittweger, D. Wildanger, and S. W. Hell. Far-field fluorescence nanoscopy of diamond color centers by ground state depletion. *EPL (Europhysics Letters)*, 86(1):14001, 2009.
- [41] Alexey Sharonov and Robin M. Hochstrasser. Wide-field subdiffraction imaging by accumulated binding of diffusing probes. *Proceedings of the National Academy of Sciences*, 103(50):18911–18916, 2006.
- [42] J. Schnitzbauer, M. T. Strauss, T. Schlichthaerle, F. Schueder, and R. Jungmann. Super-resolution microscopy with dna-paint. *Nat Protoc*, 12(6):1198–1228, 2017.
- [43] Qinsi Zheng, Manuel F. Juette, Steffen Jockusch, Michael R. Wasserman, Zhou Zhou, Roger B. Altman, and Scott C. Blanchard. Ultra-stable organic fluorophores for single-molecule research. *Chem. Soc. Rev.*, 43:1044–1056, 2014.
- [44] Soham Samanta, Wanjun Gong, Wen Li, Amit Sharma, Inseob Shim, Wei Zhang, Pintu Das, Wenhui Pan, Liwei Liu, Zhigang Yang, Junle Qu, and Jong Seung Kim. Organic fluorescent probes for stochastic optical reconstruction microscopy STORM: Recent highlights and future possibilities. *Coordination Chemistry Reviews*, 380:17–34, 2019.
- [45] Graham T. Dempsey, Joshua C. Vaughan, Kok Hao Chen, Mark Bates, and Xiaowei Zhuang. Evaluation of fluorophores for optimal performance in localization-based super-resolution imaging. *Nature Methods*, 8:1027–1040, 2011.
- [46] Makio Tokunaga, Naoko Imamoto, and Kumiko Sakata-Sogawa. Highly inclined thin illumination enables clear single-molecule imaging in cells. *Nature Methods*, 5(2):159–161, 2008.
- [47] Martin Ovesný, Pavel Křížek, Josef Borkovec, Zdeněk Švindrych, and Guy M. Hagen. ThunderSTORM: a comprehensive ImageJ plug-in for PALM and STORM data analysis and super-resolution imaging. *Bioinformatics*, 30(16):2389–2390, 2014.
- [48] Martin Ester, Hans-Peter Kriegel, Jörg Sander, and Xiaowei Xu. A density-based algorithm for discovering clusters in large spatial databases with noise. page 226–231, 1996.
- [49] Manchen Zhao, Philip R. Nicovich, Miro Janco, Qiji Deng, Zhengmin Yang, Yuanqing Ma, Till Böcking, Katharina Gaus, and J. Justin Gooding. Ultralow- and low-background surfaces for single-molecule localization microscopy of multistep biointerfaces for single-molecule sensing. *Langmuir*, 34:10012–10018, 2018.
- [50] Guoliang Zhen, Stefan Zürcher, Didier Falconnet, Fei Xu, Eva Kuennemann, and Marcus Textor. Nta-functionalized poly(l-lysine)-g-poly(ethylene glycol): A polymeric interface for binding and studying 6×his-tagged proteins. *Annual International Conference of the IEEE Engineering in Medicine and Biology - Proceedings*, 7 VOLS:1036–1038, 2005.
- [51] Tino Pleiner, Mark Bates, Sergei Trakhanov, Chung-Tien Lee, Jan Erik Schliep, Hema Chug, Marc Böhning, Holger Stark, Henning Urlaub, and Dirk Görlich. Nanobodies: site-specific labeling for super-resolution imaging, rapid epitope-mapping and native protein complex isolation. *eLife*, 4, 2015.

- [52] Jervis Vermal Thevathasan, Maurice Kahnwald, Konstanty Cieřliński, Philipp Hoess, Sudheer Kumar Peneti, Manuel Reitberger, Daniel Heid, Krishna Chaitanya Kasuba, Sarah Janice Hoerner, Yiming Li, Yu-Le Wu, Markus Mund, Ulf Matti, Pedro Matos Pereira, Ricardo Henriques, Bianca Nijmeijer, Moritz Kueblbeck, Vilma Jimenez Sabinina, Jan Ellenberg, and Jonas Ries. Nuclear pores as versatile reference standards for quantitative superresolution microscopy. *Nature Methods*, 16(10):1045–1053, 2019.
- [53] Michael Rimmel, Lukas Scheiderer, Alexey N. Butkevich, Mariano L. Bossi, and Stefan W. Hell. Spontaneously blinking fluorophores for accelerated MINFLUX nanoscopy. *bioRxiv*, 2022.
- [54] Philipp Werther, Klaus Yserentant, Felix Braun, Nicolai Kaltwasser, Christoph Popp, Mathis Baalmann, Dirk-Peter Herten, and Richard Wombacher. Live-cell localization microscopy with a fluorogenic and self-blinking tetrazine probe. *Angewandte Chemie International Edition*, 59(2):804–810, 2020.
- [55] Qinglong Qiao, Wenjuan Liu, Jie Chen, Xia Wu, Fei Deng, Xiangning Fang, Ning Xu, Wei Zhou, Shaowei Wu, Wenting Yin, Xiaogang Liu, and Zhaochao Xu. An acid-regulated self-blinking fluorescent probe for resolving whole-cell lysosomes with long-term nanoscopy. *Angewandte Chemie International Edition*, 61(21):e202202961, 2022.
- [56] Gražvydas Lukinavičius, Keitaro Umezawa, Nicolas Olivier, Alf Honigmann, Guoying Yang, Tilman Plass, Veronika Mueller, Luc Reymond, Ivan R. Corrêa Jr, Zhen-Ge Luo, Carsten Schultz, Edward A. Lemke, Paul Heppenstall, Christian Eggeling, Suliana Manley, and Kai Johnsson. A near-infrared fluorophore for live-cell super-resolution microscopy of cellular proteins. *Nature Chemistry*, 5(2):132–139, 2013.
- [57] Hideo Takakura, Yongdeng Zhang, Roman S. Erdmann, Alexander D. Thompson, Yu Lin, Brian McNellis, Felix Rivera-Molina, Shin-nosuke Uno, Mako Kamiya, Yasuteru Urano, James E. Rothman, Joerg Bewersdorf, Alanna Schepartz, and Derek Toomre. Long time-lapse nanoscopy with spontaneously blinking membrane probes. *Nature Biotechnology*, 35(8):773–780, 2017.
- [58] Nicolas Lardon, Lu Wang, Aline Tschanz, Philipp Hoess, Mai Tran, Elisa D’Este, Jonas Ries, and Kai Johnsson. Systematic tuning of rhodamine spirocyclization for super-resolution microscopy. *Journal of the American Chemical Society*, 143(36):14592–14600, 2021. doi: 10.1021/jacs.1c05004.
- [59] Ruta Gerasimaitė, Jonas Bucevičius, Kamila A. Kiszka, Sebastian Schnorrenberg, Georgij Kostiuik, Tanja Koenen, and Gražvydas Lukinavičius. Blinking fluorescent probes for tubulin nanoscopy in living and fixed cells. *ACS Chemical Biology*, 16(11):2130–2136, 2021. PMID: 34734690.
- [60] M. Bates, B. Huang, G. T. Dempsey, and X. Zhuang. Multicolor super-resolution imaging with photo-switchable fluorescent probes. *Science*, 317(5845):1749–53, 2007.
- [61] Mike Heilemann, Emmanuel Margeat, Robert Kasper, Markus Sauer, and Philip Tinnefeld. Carbocyanine dyes as efficient reversible single-molecule optical switch. *Journal of the American Chemical Society*, 127(11):3801–3806, 2005. PMID: 15771514.
- [62] Dominic A. Helmerich, Gerti Beliu, Danush Taban, Mara Meub, Marcel Streit, Alexander Kuhlemann, Sören Doose, and Markus Sauer. Photoswitching fingerprint analysis bypasses the 10-nm resolution barrier. *Nature Methods*, 19(8):986–994, 2022.

- [63] Alain Sillen and Yves Engelborghs. The correct use of “average” fluorescence parameters. *Photochemistry and Photobiology*, 67(5):475–486, 1998.
- [64] Gražvydas Lukinavičius, Keitaro Umezawa, Nicolas Olivier, Alf Honigmann, Guoying Yang, Tilman Plass, Veronika Mueller, Luc Reymond, Ivan R Corrêa, Zhen-Ge Luo, Carsten Schultz, Edward A Lemke, Paul Heppenstall, Christian Eggeling, Suliana Manley, and Kai Johnsson. A near-infrared fluorophore for live-cell super-resolution microscopy of cellular proteins. *Nature chemistry*, 5(2):132–139, 2013.
- [65] Yvan Eilers, Haisen Ta, Klaus C. Gwosch, Francisco Balzarotti, and Stefan W. Hell. MINFLUX monitors rapid molecular jumps with superior spatiotemporal resolution. *Proceedings of the National Academy of Sciences*, 115:6117–6122, 2018.
- [66] Jasmin K. Pape, Till Stephan, Francisco Balzarotti, Rebecca Büchner, Felix Lange, Dietmar Riedel, Stefan Jakobs, and Stefan W. Hell. Multicolor 3d MINFLUX nanoscopy of mitochondrial micos proteins. *Proceedings of the National Academy of Sciences*, 117(34):20607–20614, 2020.
- [67] Michael Weber, Taukeer A. Khan, Lukas J. Patalag, Mariano Bossi, Marcel Leutenegger, Vladimir N. Belov, and Stefan W. Hell. Photoactivatable fluorophore for stimulated emission depletion STED microscopy and bioconjugation technique for hydrophobic labels. *Chemistry – A European Journal*, 27(1):451–458, 2021.
- [68] Alexey N. Butkevich, Michael Weber, Angel R. Cereceda Delgado, Lynn M. Ostersehl, Elisa D’Este, and Stefan W. Hell. Photoactivatable fluorescent dyes with hydrophilic caging groups and their use in multicolor nanoscopy. *Journal of the American Chemical Society*, 143(44):18388–18393, 2021. doi: 10.1021/jacs.1c09999.
- [69] Philipp Lohner, Mariia Zmyslia, Johann Thurn, Jasmin K. Pape, Rūta Gerasimaitė, Jan Keller-Findeisen, Saskia Groeer, Benedikt Deuringer, Regine Süß, Andreas Walther, Stefan W. Hell, Gražvydas Lukinavičius, Thorsten Hugel, and Claudia Jessen-Trefzer. Inside a shell—organometallic catalysis inside encapsulin nanoreactors. *Angewandte Chemie International Edition*, 60(44):23835–23841, 2021.
- [70] Taekjip Ha and Philip Tinnefeld. Photophysics of fluorescent probes for single-molecule biophysics and super-resolution imaging. *Annual Review of Physical Chemistry*, 63:595–617, 2012.
- [71] Tobias Englehardt. *MinFlux Nanoscopy with Interferometric Approach*. Phd thesis, Max-Planck-Institute for medical research, 2021.
- [72] Jan O. Wolff, Lukas Scheiderer, Tobias Engelhardt, Johann Engelhardt, Jessica Matthias, and Stefan W. Hell. Minflux dissects the unimpeded walking of kinesin-1. *bioRxiv*, 2022.
- [73] Ali H. Shaib, Abed Alrahman Chouaib, Vanessa Imani, Rajdeep Chowdhury, Svilen Veselinov Georgiev, Nikolaos Mougios, Mehar Monga, Sofiia Reshetniak, Daniel Mihaylov, Han Chen, Parisa Fatehbasharad, Dagmar Crzan, Kim-Ann Saal, Claudia Trenkwalder, Brit Mollenhauer, Tiago F. Outeiro, Julia Preobraschenski, Ute Becherer, Tobias Moser, Edward S. Boyden, A Radu Aricescu, Markus Sauer, Felipe Opazo, and Silvio O. Rizzoli. Expansion microscopy at one nanometer resolution. *bioRxiv*, 2022.
- [74] Thomas Schlichthaerle, Maximilian T. Strauss, Florian Schueder, Alexander Auer, Bianca Nijmeijer, Moritz Kueblbeck, Vilma Jimenez Sabinina, Jervis V. Thevathasan, Jonas Ries, Jan Ellenberg, and Ralf Jungmann. Direct visualization of single nuclear pore complex proteins using genetically-encoded probes for dna-paint. *Angewandte Chemie International Edition*, 58(37):13004–13008, 2019.

- [75] Thomas Schlichthaerle, Maximilian T. Strauss, Florian Schueder, Alexander Auer, Bianca Nijmeijer, Moritz Kueblbeck, Vilma Jimenez Sabinina, Jervis V. Thevathasan, Jonas Ries, Jan Ellenberg, and Ralf Jungmann. Direct visualization of single nuclear pore complex proteins using genetically-encoded probes for dna-paint. *bioRxiv*, 2019.

# Acknowledgments

I am fortunate of being surrounded by so many positive people helping me constantly. Without them, my Ph.D. wouldn't have been possible and I want to say 'thank you' to all of you.

Especially, I want to thank Prof. Dr. Stefan Hell for giving me the opportunity to do my Ph.D. in his lab. You gave me a chance to prove myself in a time where I stopped believing. You challenged me constantly to interrogate myself scientifically and taught me to stand my point when I was convinced. Also, I want to thank Prof. Dr. Joachim Spatz for participating as second referee of my thesis. Prof. Dr. Ulrich Schwarz and Prof. Dr. Selim Jochim I want to thank to participate in the examination committee.

I count myself as a lucky person because I had three terrific co-supervisors taking care of me at different stages of my Ph.D. I honestly don't know where to start thanking you Dr. Mariano Bossi! It's pretty rare to meet someone, with whom one can work like two well-oiled gears. Moreover, you taught me so much about statistics, data analysis, photophysics and movies out of the 80's. I really enjoyed our big talks about politics and football. Thanks for letting me be a part of your projects and proof reading this thesis.

Dr. Johann Engelhardt I want to thank for all input you gave me on physics, especially optics, teaching me about microscopy, how to not lose the overview of all the cables and sharing your life experiences with me.

Dr. Jessica Matthias I want to thank for all the input on physical, biochemistry. When I started here everything was physics for me, but that view change now: Everything is physical biochemistry. Thank you also for the nice chats in our offices and also for teaching me project handling and proof reading this thesis.

Dr. Richard Lincoln I also want to thank. You paved the way for great project I can count myself lucky to participate in. Especially thank you Ricky for proof reading my thesis.

Also, I want thank Dr. Alexey Butkevich for letting me work with his fluorophores.

Dr. Jade Cottam-Jones I want to thank for taking care of a lot of administrative things.

Moreover, I also want to thank our facilities inside our institute: Thanks to the IT department for immediately helping if something was not working as it was supposed to be. Thanks to

Martin Lukat and Daniel Berndt of the mechanical workshop for supplying me with so many custom-built constructions, often twice. And also thank you Dr. Elisa D'Este for running the optical microscopy facility so well. I really appreciate the input you provided for me on the MINFLUX system and also how much freedom you gave me to adapt the system to my needs.

Jasmine Hubrich and Alena Fischer I want to thank to supply me so reliably with cells over the past years, even when I was unreliable with my orders. Alena, I also thank you for taking care with labeling in the last weeks of my Ph.D. Jasmine, thank you for your valuable input on all the labeling strategies I used and proof reading the thesis.

I also want to thank the whole lab for the nice working environment you provided me. Special thanks to the physicsboys (Dr. Marcus Held, Dr. Tobias Engelhardt, Otto Wolff, Julian Rickert and Philip Matthias). The helpfulness regarding our optical setups and the problems arising with them I'll never forget. Thank you, Otto for all your input on programming and statistics. I really enjoyed discussing experimental problems with you, as they always ended up pretty fruitful. Also, our Disc Golf and bouldering sessions I appreciate very much, as they show me that I can call you more than just colleagues.

Also, I want to thank the supervisor of my master thesis Dr. Tobias Siegle. You really acted like a role model to me in many ways and also outside science I tend to ask myself, what would you do in that situation.

Moreover, I want to thank my friends, especially the guys from Karlsruhe: Dönz, Jojo, Bene, Krami, Sepp, Philma, Kai and many more. I loved studying with you, I love hanging out with you and I love how we're cheering up each other when one needs it.

I know only three people on this planet who believed in me my whole live: These are my parents and my brother. Thanks for supporting me all the time over the past 30 years and for being around when I need you.